Heiko Füser

Interaction of Femtosecond Lasers with Semiconductors:

Terahertz Frequency Combs and Terahertz Steering

Cuvillier Verlag Göttingen
Internationaler wissenschaftlicher Fachverlag

Interaction of Femtosecond Lasers with Semiconductors:
Terahertz Frequency Combs and Terahertz Steering

Interaction of Femtosecond Lasers with Semiconductors: Terahertz Frequency Combs and Terahertz Steering

---

Von der Fakultät für Elektrotechnik, Informationstechnik, Physik
der Technischen Universität Carolo-Wilhelmina
zu Braunschweig
zur Erlangung des Grades eines
Doktors der Naturwissenschaften
(Dr. rer. nat.)
genehmigte

D i s s e r t a t i o n

von Heiko Füser
aus Kassel

1. Referent: Prof. Dr. rer. nat. Andreas Hangleiter
2. Referent: Priv.-Doz. Dr. rer. nat. Uwe Siegner

eingereicht am: 13.02.2014
mündlichen Prüfung am: 22.04.2014

2014

Bibliografische Information der Deutschen Nationalbibliothek
Die Deutsche Nationalbibliothek verzeichnet diese Publikation in der Deutschen Nationalbibliografie; detaillierte bibliografische Daten sind im Internet über http://dnb.d-nb.de abrufbar.
1. Aufl. - Göttingen : Cuvillier, 2014
Zugl.: (TU) Braunschweig, Univ., Diss., 2014

Nonnenstieg 8, 37075 Göttingen
Telefon: 0551-54724-0
Telefax: 0551-54724-21
www.cuvillier.de

1. Auflage, 2014
Gedruckt auf umweltfreundlichem, säurefreiem Papier
aus nachhaltiger Forstwirtschaft.

ISBN 978-3-95404-708-6
eISBN 978-3-7369-4708-5

Abstract

During the last decades, the Terahertz (THz) frequency range has lead to steadily increasing interest in a scientific as well as in an economic context. Significant effort has been spent to further develop technologies operating in this specific region of the electromagnetic spectrum. The increasing importance of this relatively young technique for modern society results in new challenges for science and technology. On the one hand national metrology institutes like the Physikalisch-Technische Bundesanstalt need to establish traceability for THz sources and detectors. On the other hand the economic needs offer great potential for novel developments and detailed investigations of the underlying physical dependencies.

This outlines the two main points treated in this thesis. The first part introduces a measurement scheme for a precise characterization of continuous-wave, free-space THz radiation. Based on the metrologically well-established technique of optical frequency combs, rectification and modulation techniques are introduced to establish a THz frequency comb allowing for the measurement of THz signals. Thereby, two different methods are compared: photoconductive and electro-optic detection. Both techniques allow to construct a setup for high-precision frequency measurements. With a relative measurement accuracy of $(9 \pm 3) \cdot 10^{-14}$ over a measurement interval of 10 s, a hitherto unreached accuracy in the determination of THz frequencies is demonstrated. Next to the frequency, the measurement scheme allows for the detection of the relative amplitude and phase of the emitted radiation. Via a relative movement between source and detector, spatially resolved emission patterns are obtained. A comparison of both detection methods is performed. Next to the precision characterization of a 100 GHz emitter, the emission of a 30 THz source is analyzed to study the frequency bandwidth of the detection methods.

The second part of the thesis investigates basic properties of a pulsed, spatially steerable THz source based on all-optically generated currents in gallium arsenide (GaAs). Utilizing the properties of the crystal structure, different types of currents are excited. On the one hand, drift- and diffusion-based currents are generated, flowing perpendicular to the semiconductor surface. On the other hand, in-plane shift currents are excited, whose flow direction can be controlled via the polarization of the pump

light. The superposition of both current contributions results in a spatially directed THz field. Modifying the shift current direction allows for an angular change of the emission direction of more than 8°. Comparing the experimental results to a theoretical model, a detailed investigation of the current dependencies is possible. The influence of the excitation conditions on the steering angle are analyzed. This method of the coherently controlled "THz steering effect" allows for a fast, reliable and all-optical generation method of spatially directed THz fields. This proves to be valuable for various technical applications, ranging from imaging to communication techniques.

Zusammenfassung

In den letzten Jahrzehnten rückte der Terahertz (THz) Frequenzbereich verstärkt in den Fokus wissenschaftlicher und wirtschaftlicher Interessen. Erhebliche Anstrengungen wurden unternommen, um die Entwicklung neuartiger Technologien in dieser speziellen Region des elektromagnetischen Spektrums voranzutreiben. Durch die wachsende Bedeutung der verhältnismäßig jungen THz-Technologie für die moderne Gesellschaft ergeben sich neue Herausforderungen an Wissenschaft und Technik. Zum einen steht speziell für nationale Metrologieinstitute wie die Physikalisch-Technische Bundesanstalt die rückgeführte Charakterisierung von THz-Quellen und -Detektoren im Zentrum der Aufmerksamkeit. Zum anderen bietet die wirtschaftliche Bedeutung der Technologie eine Vielzahl neuer Entwicklungsmöglichkeiten und Ansätze für weitergehende Untersuchungen der zugrundeliegenden physikalischen Effekte.

Mit diesen zwei Themenschwerpunkten befasst sich die vorliegende Dissertationsschrift. Im ersten Teil der Arbeit wird ein Messverfahren für die präzise Charakterisierung von Dauerstrich-Freistrahl-THz-Quellen vorgestellt. Basierend auf der metrologisch etablierten Technik der optischen Frequenzkämme kann mittels eines Gleichrichtungs- oder Modulationsvorganges ein THz-Frequenzkamm erzeugt werden, welcher zur Detektion des THz-Signals verwendet wird. Hierbei werden zwei unterschiedliche Verfahren miteinander verglichen, basierend auf photoleitenden und elektrooptischen Detektionsmethoden. Mit beide Verfahren kann ein Messaufbau zur hochgenauer Frequenzbestimmung demonstriert werden. Hierbei wird ein softwaregestütztes Datenanalyseverfahren verwendet, welches die Rauscheinflüsse des unstabilisierten optischen Frequenzkammes eliminiert. Mit einer relativen Messgenauigkeit von $(9 \pm 3) \cdot 10^{-14}$ über eine Messzeit von 10 s kann eine bis dato unerreichte Genauigkeit der Frequenzbestimmung im THz-Frequenzbereich demonstriert werden. Neben der Frequenzbestimmung ermöglicht das Messverfahren auch die Detektion der relativen Amplitude und Phase der emittierten THz-Strahlung. Über eine relative Verschiebung von Signalquelle und Detektor lassen sich ortsaufgelöste Darstellungen dieser Parameter realisieren und Unterschiede in beiden Detektionsverfahren analysieren. Um die Frequenzbandbreite der Messverfahren darzustellen, wird neben der Präzisionscharakterisierung

einer Quelle im Frequenzbereich von 100 GHz auch das Signal einer 30-THz-Quelle detektiert und analysiert.

Der zweite Teil der Arbeit befasst sich mit grundlegenden Untersuchungen zur Entwicklung einer gepulsten, räumlich lenkbaren THz-Signalquelle. Das zugrundeliegende Erzeugungsprinzip basiert auf der rein optischen Anregung von Stromflüssen in Galliumarsenid (GaAs). Hierbei werden die Eigenschaften der Kristallstruktur des Materials ausgenutzt, welche die Erzeugung unterschiedlicher Stromkomponenten ermöglicht. Zum einen werden Drift- und Diffusionsströme induziert, die senkrecht zur Halbleiteroberfläche fließen. Zum anderen werden Verschiebungsströme parallel zur Halbleiteroberfläche angeregt. Diese lassen sich durch eine Modifikation der Polarisation des Anregungslichts in ihrer Richtung umkehren. Die Überlagerung der mit beiden Stromkomponeten einhergehenden elektromagnetischen Felder resultiert in einer räumlich gerichteten Emission der THz-Strahlung. Eine Modifikation der Verschiebungsstromrichtung bewirkt dabei eine Veränderung der Emissionsrichtung über einen Winkel von mehr als 8°. Mit Hilfe eines theoretischen Modells wird dieser Effekt detailliert untersucht und dessen Abhängigkeiten von den Anregungsparametern analysiert. Die beschriebene Methode des „THz Steerings“ erweist sich als eine zuverlässige, schnelle und auf rein optischen Effekten basierende Methode zur Lenkung von THz-Feldern, wertvoll für die technische Anwendung in einer Vielzahl von Bereichen von bildgebenden Verfahren bis zu neuartigen Kommunikationstechniken.

Vorveröffentlichungen der Dissertation

Teilergebnisse aus dieser Arbeit wurden mit Genehmigung der Fakultät für Elektrotechnik, Informationstechnik, Physik, vertreten durch den Mentor der Arbeit, in folgenden Beiträgen vorab veröffentlicht:

Publikationen

[A1] H. Füser and M. Bieler, "Terahertz Frequency Combs," *Journal of Infrared, Millimeter, and Terahertz Waves*, Nov. 2013, http://dx.doi.org/10.1007/s10762-013-0038-8.

[A2] H. Füser and M. Bieler, "Terahertz beam steering by optical coherent control," *Applied Physics Letters*, vol. 102, no. 25, p. 251109, 2013.

[A3] H. Füser, R. Judaschke, and M. Bieler, "High-precision frequency measurements in the THz spectral region using an unstabilized femtosecond laser," *Applied Physics Letters*, vol. 99, p. 121111, 2011.

Tagungsbeiträge

[B1] Y. Deng, H. Füser, R. Judaschke, and M. Bieler, "Traceable amplitude measurement of CW and pulsed THz radiation using femtosecond lasers," in *VDI International Forum on Terahertz Spectroscopy and Imaging, Kaiserslautern*, 2014.

[B2] H. Füser and M. Bieler, "Steerable emission of THz radiation by optical coherent control," *Infrared - Milimeter Wave - Terahertz (IRMMW-THz), Mainz*, 2013.

[B3] H. Füser and M. Bieler, "Steerable THz emission by optical coherent control," *Progress in Electromagnetic Research Symposium (PIERS), Stockholm*, 2013.

[B4] H. Füser and M. Bieler, "Frequency, amplitude, and phase measurements of GHz and THz sources using unstabilized THz frequency combs," in *Proc. SPIE. 8624, Terahertz, RF, Millimeter, and Submillimeter-Wave Technology and Applications VI* (L. P. Sadwick and C. M. O'Sullivan, eds.), p. 86240, 2013.

[B5] H. Füser and M. Bieler, "(Invited) Using THz frequency combs generated from unstabilized femtosecond lasers for near- and far-field characterization of GHz and THz emitters," *Infrared - Milimeter Wave - Terahertz (IRMMW-THz), Wollongong*, 2012.

[B6] H. Füser, R. Judaschke, and M. Bieler, “High-precision THz spectrum analyzer based on an unstabilized optical frequency comb,” in *VDI International Forum on Terahertz Spectroscopy and Imaging, Kaiserslautern*, 2012.

[B7] H. Füser, R. Judaschke, and M. Bieler, “High-precision THz spectrum analyzer based on an unstabilized frequency comb,” *Infrared - Milimeter Wave - Terahertz (IRMMW-THz), Houston*, 2011.

Weitere Veröffentlichungen

[C1] H. Füser, S. Eichstädt, K. Baaske, C. Elster, K. Kuhlmann, R. Judaschke, K. Pierz, and M. Bieler, “Optoelectronic time-domain characterization of a 100 GHz sampling oscilloscope,” *Measurement Science and Technology*, vol. 23, p. 025201, 2012.

[C2] H. Füser and M. Bieler, “(Invited) Laser-based waveform measurements,” *European Microwave Week, Nuremberg*, 2013.

[C3] M. Bieler and H. Füser, “Realization of an ultra-broadband voltage pulse standard utilizing time-domain optoelectronic techniques,” *SPIE Photonics West, San Francisco*, 2013.

[C4] M. Bieler and H. Füser, “Laser-based waveform metrology at PTB: Development of an ultrabroadband voltage pulse standard,” *Infrared - Milimeter Wave - Terahertz (IRMMW-THz), Wollongong*, 2012.

[C5] P. D. Hale, D. F. Williams, A. Dienstfrey, J. Wang, J. Jargon, D. Humphreys, M. Harper, H. Füser, and M. Bieler, “Traceability of High-Speed Electrical Waveforms at NIST, NPL, and PTB,” in *Conference on Precision Electromagnetic Measurements, Washington*, pp. 1–2, 2012.

[C6] M. Winter, H. Füser, M. Bieler, G. Siegmund, and C. Rembe, “The Problem of Calibrating Laser-Doppler Vibrometers at High Frequencies,” *10th International Conference on Vibration Measurements, Ancona*, 2012.

[C7] H. Füser and M. Bieler, “Strategy for laser-based waveform metrology for frequencies ranging from below 1 GHz to 1 THz,” *European Microwave Week, Manchester*, 2011.

[C8] H. Füser, K. Baaske, S. Eichstädt, C. Elster, K. Kuhlmann, R. Judaschke, K. Pierz, and M. Bieler, “Time domain characterization of a 110 GHz sampling oscilloscope using optoelectronic techniques,” *Kleinheubacher Tagung, Miltenberg*, 2010.

Contents

1 Introduction **1**
- 1.1 Motivation . . . 1
- 1.2 Outline of the Thesis . . . 4

2 Theoretical and Experimental Fundamentals **7**
- 2.1 Susceptibility of Semiconductors . . . 7
  - 2.1.1 Lorentz Oscillator Model . . . 8
  - 2.1.2 Power Series of the Susceptibility . . . 10
- 2.2 Ti:Sa Femtosecond Laser . . . 16
  - 2.2.1 Basic Properties . . . 17
  - 2.2.2 Optical Frequency Comb . . . 18
  - 2.2.3 Noise Effects . . . 19
- 2.3 Employing the Semiconductor Susceptibility for Terahertz Generation and Detection . . . 22
  - 2.3.1 Terahertz Generation . . . 22
  - 2.3.2 Terahertz Detection . . . 28

3 Terahertz Frequency Combs **41**
- 3.1 Motivation and Review of Previous Work . . . 41
- 3.2 High-precision Frequency Measurements . . . 42
  - 3.2.1 Transfer Concept . . . 42
  - 3.2.2 Experimental Setup . . . 44
  - 3.2.3 Data Analysis . . . 47
  - 3.2.4 Measurement Results . . . 49
  - 3.2.5 Summary . . . 58
- 3.3 Amplitude and Phase Measurements . . . 59
  - 3.3.1 Experimental Setup . . . 59
  - 3.3.2 Spatially Resolved Measurements . . . 62
  - 3.3.3 Summary . . . 66
- 3.4 Frequency Range . . . 67
  - 3.4.1 Experimental Setup . . . 68
  - 3.4.2 Measurement Results . . . 69
  - 3.4.3 Summary . . . 73
- 3.5 Summary and Outlook . . . 74

4 Coherent Control of Steerable THz Emitters **77**
4.1 Motivation and Review of Previous Work 77
4.2 Schematic Description 78
4.2.1 Temporal Shape of the THz Traces 79
4.2.2 Interference of the Emitted Fields 81
4.3 Experimental Demonstration 83
4.3.1 Experimental Setup 83
4.3.2 Measurement Results 85
4.3.3 Analysis of the Current Properties 88
4.3.4 Spatial Profile of the Emission Pattern 90
4.4 Dipole Model 91
4.4.1 Fundamental Relations 91
4.4.2 Variation of Parameters 96
4.5 Summary and Outlook 101

5 Conclusion **105**

Appendix A Electro-Optic Detection Crystals **107**

Appendix B Photoconductive Antenna Geometries **109**

1 Introduction

1.1 Motivation

Research and development in the field of Terahertz (THz) science and technology have intensified significantly over the past 30 years [1–7]. The ongoing interest [1], motivated by both academic as well as economic means, reflects the huge technological progress in a specific part of the electromagnetic spectrum which has been difficult to access for many decades. Due to the lack of efficient generation and detection mechanisms of electromagnetic signals [2], the corresponding spectral region has long been referred to as THz gap. The exact definition of the boundary frequencies of this gap greatly varied, depending on the specific problem of interest. Typically frequencies from 100 GHz up to 30 THz have been considered (i.e. wavelengths between 3 mm and 10 μm, respectively) [3]. Hereby the lower boundary was roughly marked by the frequency limit of typical all-electronic devices such as amplifiers and oscillators. The upper value of the THz frequency range has been determined from the optical side of the electromagnetic spectrum, given by the operational frequencies of typical laser sources such as the CO_2 laser.

For a long time, the THz frequency region was only of interest for a scientific niche of mostly astronomy-related spectroscopy [4]. However, over time this part of the frequency spectrum became a matter of increasing interest for other fields, in particular for fundamental physics. Many interaction phenomena between radiation and matter are found in the far-infrared region, covering a wide range of elementary excitations such as phonons, plasmons, excitons and various transition effects [5–7]. With this development, the necessity for appropriate tools to be utilized in the corresponding investigations arouse. Consequently, the research on THz sources and detectors intensified. Various THz generation mechanisms have been established, ranging from electronic-based devices like solid-state oscillators [8] over free-electron oscillators like gyrotrons [9, 10] to THz lasers, i.e. gas lasers [11, 12], free electron lasers [13, 14] or quantum-cascade lasers (QCL) [15, 16], and other sources [17]. Moreover, broadband spectroscopic systems were realized, utilizing short opti-

cal laser pulses [18, 19]. In addition to the radiative approach driven by spectroscopic needs, also the progress in electronics has been steadily narrowing the THz gap. Here, especially the continually increasing demand of bandwidth of modern communication technology [20–23] acted as the main driver for the ongoing development of THz technologies. Wireless data transmission at high gigabit rates [24] has already successfully been employed, e.g. for the television broadcasting of events of major interest like the 2008 Summer Olympic Games in Beijing [25]. These technological breakthroughs are based on the properties of today's state-of-the-art integrated circuits, whose operational frequencies already reach far into the THz region. For instance, devices like voltage controlled oscillators operating at several 100 GHz [26] or integrated diode circuits and THz mixers for frequencies up to 2.5 THz [27] allow for the realization of photonic circuits. In combination with the novel THz sources available, e.g. QCLs, envisaged electro-photonic designs promise to bridge the THz gap [28].

The advent of THz generation and detection techniques unlocked the door for a multitude of applications. In various fields such as medical diagnosis, quality control, chemical and biological sensing, imaging techniques for security applications and other purposes, THz techniques have proven to be a valuable tool [29–33]. The increasing economic interest in this particular frequency band indispensably calls for metrological developments to characterize devices, judge the reliability of measurement methods, precisely compare different technical approaches or define common standards. For about a decade, national metrology institutes (NMIs) all over the world intensified their work towards THz metrology [34] and, by this, accompanied the rise of this new technology. Large NMIs performing research in the field of THz metrology are, e.g., the National Institute of Standards and Technology (NIST) in the USA, the National Physical Laboratory (NPL) in the UK, the National Metrology Institute of Japan (NMIJ) and the National Institute of Information and Communications Technology (NICT) in Japan, the National Institute of Metrology (NIM) in China, the Korea Research Institute of Standards and Science (KRISS) in Korea and the Physikalisch-Technische Bundesanstalt (PTB) in Germany. To cover the wide range of THz applications, metrological research projects have been established. These activities comprise spectrometry applications [35–37], THz radiometry [38–43], characterization of high-frequency electronics [44–49] [C1], the calibration of THz sources [50–52], high-precision frequency measurement techniques [53–56] and more. Despite these projects, THz metrology constitutes a very recent branch in the portfolio of NMIs, thus requiring intensified ongoing research. A vital task for the future concerns an international coordination of these research projects and a thorough comparison of the various ap-

proaches realized by the different NMIs. Envisaged comparisons cover, e.g., the characterization of high-frequency electronic devices [C5] or the development of traceable THz detectors [57].

This description outlines the framework in which the work presented in the following chapters is placed. This thesis is divided into two main parts, discussing different aspects of the ongoing effort to close the THz gap. First, precision measurements of free-space, continuous-wave (cw) electromagnetic signals in the THz frequency domain are presented. An accurate measurement of different parameters of the radiation is realized by utilizing the concept of THz frequency combs [53]. Incorporating a data processing scheme to correct the measurement data for the noise influences of the laser system, high-precision frequency determination with an accuracy of the measurement system as high as $(9 \pm 3) \cdot 10^{-14}$ is demonstrated using a 100 GHz source [A3]. This presents an improvement of two orders of magnitude as compared to previously reported results [54, 55, 58]. THz communication, imaging and sensing applications are not only based on frequency, but also on amplitude and phase information of electromagnetic signals. Thus, employing the same optoelectronic detection scheme as utilized for the frequency measurements, a spatially resolved analysis of these parameters is demonstrated. Here, standard deviations of the mean of 0.1 % and 0.2° are reached for the measurement of the relative amplitude and phase, respectively. With this, the full characterization of the emission properties of cw-THz sources is demonstrated [A1]. By utilizing the emission of a CO_2-laser to access the far-end of the THz gap, the frequency limits of the detection process are analyzed. For a precise determination of the different parameters of electromagnetic radiation, a detailed understanding of the interaction processes of the electromagnetic signals with the detection system is necessary. To account for this, an evaluation and comparison of two techniques for the detection process is presented, namely photoconductive and electro-optic detection. By this, two entirely different light-matter interaction processes (with the polarization depending in first respectively second order on the optical field strength) are analyzed towards their usability for the aforementioned metrological tasks.

The second topic of this thesis addresses a THz generation mechanism. For many of the realized and envisaged applications operating in the former THz gap, specific properties of the THz emission are mandatory. Among these properties, the need for spatial control of the emitted fields has become more and more important. For instance, communications at high frequencies requires the realization of different propagation channels [48]. Furthermore, spatially resolved spectroscopy and imaging applications are based on a relative movement between the THz field and

the device under test [59]. One possible approach to accomplish such demands is given by a steerable THz emitter. In this thesis such an emitter is presented, based on an all-optical approach for the THz generation process as well as for the control of the emitted fields [A2]. Utilizing the optically induced emission of THz radiation from a gallium arsenide (GaAs) semiconductor material, adjustable THz steering angles reaching from below 2° to more than 8° are realized. The presented method allows for a fast, reliable and non-mechanical beam steering. A simple model is introduced, capable to relate the steering effect to different optically excited current contributions. With the help of the model an analysis of the underlying relations and dependencies between the THz field and the optical excitation parameters is presented. This work is the basis for future developments of next-generation THz emitters.

1.2 Outline of the Thesis

This thesis is organized as follows. In chapter 2, the theoretical and experimental fundamentals are given, common for both topics of THz generation and THz detection by optoelectronic means. Indifferent whether the generation of pulsed THz signals or the detection of cw-THz radiation is regarded, the corresponding processes described here are based on the interaction of light with a semiconductor material. Thus, the concept of semiconductor susceptibility is introduced (section 2.1), with a focus on the aspects being relevant for this thesis. Subsequently the basic properties of the light source used throughout this work are presented (Section 2.2), a femtosecond solid-state laser utilizing a titanium-doped sapphire crystal. Finally the findings of both sections are combined (section 2.3), introducing the resulting effects and dependencies of the light-matter interaction relevant for the remainder of the thesis.

Chapter 3 represents the treatment of THz detection by use of THz frequency combs. After a brief motivation and review of the related literature (section 3.1) the high-precision frequency measurement scheme (section 3.2), the spatially resolved amplitude and phase measurements (section 3.3) and the frequency range of the detection methods (section 3.4) are discussed. In all sections, a comparison of both electro-optic and photoconductive detection is performed. Hence, the chapter closes with a conclusion and outlook regarding the advantages and disadvantages of both methods (section 3.5).

Chapter 4 introduces the concept of coherently controlled THz emitters. Again a brief motivation and overview of the corresponding literature is given (section 4.1). A schematic description outlines the concept of

the THz steering mechanism (section 4.2), which is then experimentally demonstrated and analyzed (section 4.3). A more detailed understanding of the steering effect is obtained by simulating the radiation pattern using a dipole model (section 4.4). Finally, the obtained insights and conclusions allowing for an improvement of the technique are summarized (section 4.5).

An outlook for future work is given in the last part of this thesis, chapter 5.

2 Theoretical and Experimental Fundamentals

In this chapter, a description of the fundamental relations necessary in the remainder of the thesis is given. First, the concept of susceptibility is introduced in section 2.1. Going from a classical description to a quantum mechanical approach, the basic expressions for the light-matter interaction utilized in the following chapters are derived. Second, the properties of the laser system used throughout the presented work are summarized in section 2.2. Here, especially the concept of optical frequency combs is introduced, as well as the noise contributions inherent to the laser process. Section 2.3 combines the hitherto outlined insights and describes the fundamental equations for the generation and detection of THz signals based on light-matter interaction.

2.1 Susceptibility of Semiconductors

The interaction of light with matter reveals a rich and complex field in modern physics. Atomic systems offer specific responses if excited by electromagnetic waves under appropriate conditions. Especially if the atoms are arranged in a regularly ordered scheme like crystal lattices, light may be used as a tool to induce well-defined effects. To introduce the fundamental relations of light-matter interactions necessary in the scope of this work, the following section briefly reviews the corresponding literature, e.g. [60–62], as well as recent publications for a more specific examination of the topic. Depending on the level of detail of the investigation, more or less accurate models can be used to describe the appearing interaction phenomena. Hence, first a macroscopic picture is presented to establish a general overview and introduce basic phenomena. In a second step, a more elaborated approach based on a quantum mechanical description is given, which is necessary to explain the detailed material response after excitation with an electromagnetic field of high power.

2.1.1 Lorentz Oscillator Model

The basic concept of susceptibility is best introduced using a highly restricted model. Regarding a material system like an atom or a solid composed of a large group of non-interacting atoms, the system consists of positively charged ions and negatively charged electrons bound to the ions. If such an electron is exposed to a time-varying, monochromatic electrical field $\mathbf{E}'(t) = \mathbf{E}'(\omega)\exp(-i\omega t) + \text{c.c.}$ with a frequency ω and an amplitude $\mathbf{E}'(\omega)$ and if this field is not strong enough to break the bond between ion and electron, a relative displacement $\mathbf{x}(t)$ of the electron from its equilibrium position is caused. Thus, a dipole moment $\mathbf{p}(t) = e\mathbf{x}(t)$ results, with e expressing the elementary charge. Under the influence of the temporal variation of $\mathbf{E}'(t)$ and the restraining field of the positive charge, the electron movement may be described as a damped driven oscillation [61]

$$m_0 \frac{d^2\mathbf{x}(t)}{dt^2} = -2m_0\gamma\frac{d\mathbf{x}(t)}{dt} - m_0\omega_0'^2\mathbf{x}(t) + e\mathbf{E}'(t), \tag{2.1}$$

where m_0 is the electron mass, ω_0' and γ are the resonance frequency and the damping constant of the oscillator, respectively. The latter corresponds to the radiative losses caused by an accelerated charge particle. This expression is solved by the ansatz $\mathbf{x}(t) = \mathbf{x}(\omega)\exp(-i\omega t)$, which inserted into (2.1) results in $\mathbf{x}(t) = -e\mathbf{E}'(t)/\left[m_0\left(\omega^2 + 2i\omega\gamma - \omega_0'^2\right)\right]$. Hence a proportionality between the dipole moment and the electrical field is given,

$$\begin{aligned}\mathbf{p}(t) &= \frac{e^2}{m_0}\frac{1}{\omega_0'^2 - \omega^2 - i2\gamma\omega}\,\mathbf{E}'(t)\\ &= a_p(\omega)\mathbf{E}'(t),\end{aligned} \tag{2.2}$$

where the complex proportional constant defines the optical polarizability $a_p(\omega)$ of the Lorentz oscillator model.

For homogeneous materials composed of many of such oscillators, it is convenient to express the proportionality between the overall dipole moment $\mathbf{P}(t)$ and an electrical field $\mathbf{E}(t)$ by the electric susceptibility χ,

$$\mathbf{P}(t) = \epsilon_0\chi\mathbf{E}(t). \tag{2.3}$$

Here and in the following, the International System of Units (SI) is used, thus the constant ϵ_0 denoting the electric permittivity of free space is introduced in (2.3). Following the description of the oscillator model, the susceptibility is connected to $a_p(\omega)$ via the Clausius-Mossotti Relation. The latter takes into account that the local field $\mathbf{E}'(t)$ at the position of an atom is influenced by the surrounding polarization and, thus, differs from the

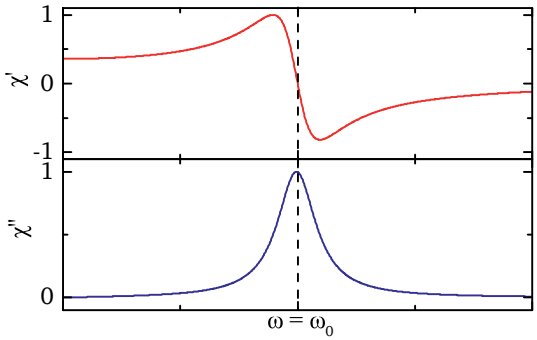

Figure 2.1 Real and imaginary part of the normalized susceptibility around the resonance frequency ω_0, denoted as dashed line.

externally applied field $\mathbf{E}(t)$ [61]. Together with the number of oscillators per unit volume N, it follows for the susceptibility

$$\chi(\omega) = \frac{Ne^2}{m_0} \frac{1}{\omega_0^2 - \omega^2 - i2\gamma\omega}, \tag{2.4}$$

having a slightly detuned resonance frequency ω_0 with respect to ω_0' due to the local-field correction. Separating real and imaginary part of $\chi = \chi'(\omega) + i\chi''(\omega)$, it follows

$$\chi'(\omega) = \frac{Ne^2}{m_0} \frac{\omega_0^2 - \omega^2}{\left(\omega^2 - \omega_0^2\right)^2 + 4\omega^2\gamma^2} \tag{2.5a}$$

$$\chi''(\omega) = \frac{Ne^2}{m_0} \frac{2\gamma\omega}{\left(\omega^2 - \omega_0^2\right)^2 + 4\omega^2\gamma^2}. \tag{2.5b}$$

The behavior of χ' and χ'' around the resonance frequency ω_0 is shown in figure 2.1. The course of the real part describes dispersion, whereas the imaginary part is related to absorption effects as will be discussed in the following. Using the definition of the dielectric permittivity $\epsilon(\omega) = \epsilon_0 (1 + \chi(\omega))$, the ability of a material to transmit an electrical field is described. Due to the complex quantity χ, the material's refractive index $n \approx \sqrt{\epsilon(\omega)/\epsilon_0}$ is complex as well, having a real and an imaginary part $n = n'(\omega) + in''(\omega)$ expressed by

$$n'(\omega) = \sqrt{\frac{1}{2\epsilon_0}\left(\epsilon'(\omega) + \sqrt{\epsilon'(\omega)^2 + \epsilon''(\omega)^2}\right)} \tag{2.6a}$$

$$n''(\omega) = \sqrt{\frac{1}{2\epsilon_0}\left(-\epsilon'(\omega) + \sqrt{\epsilon'(\omega)^2 + \epsilon''(\omega)^2}\right)}. \tag{2.6b}$$

For an electromagnetic wave propagating through matter along a direction z, the wave vector $k_z = \frac{\omega}{c} = \frac{\omega}{c_0} n$, with c and c_0 being the speed of light in matter and in vacuum, respectively, is expressed as $k_z = \frac{\omega}{c_0} n' + i \frac{\omega}{c_0} n''$. It follows

$$e^{i(k_z z - \omega t)} = e^{i\left(\left(\frac{\omega}{c_0} n' + i \frac{\omega}{c_0} n''\right) z - \omega t\right)} = e^{i\left(k'_z z - \omega t\right)} e^{-\frac{\omega}{c_0} n'' z}, \tag{2.7}$$

with $k'_z = \frac{\omega}{c_0} n'$. The second exponential function on the right hand side in equation (2.7) expresses the absorption of the wave inside the material. This defines the absorption coefficient

$$\alpha(\omega) = 2 \frac{\omega n''(\omega)}{c_0} = \frac{\omega \epsilon''(\omega)}{n'(\omega) \epsilon_0 c_0} \approx \frac{\omega \chi''(\omega)}{n_b c_0}, \tag{2.8}$$

which depends on the imaginary part of ϵ and the real part of the refractive index. Restricting the further discussion to semiconductors like GaAs, the optical resonance frequencies ω_0 are found in the ultraviolet energy range and by this energetically much higher than the fundamental absorption edge E_{gap} [63]. For photon energies around E_{gap}, $n'(\omega)$ varies slowly with ω, and, thus, may be replaced by a constant background index n_b. The frequency behavior of the absorption coefficient $\alpha(\omega)$ is then essentially determined by the imaginary part of the dielectric function $\epsilon''(\omega)$ which is proportional to the imaginary part of the susceptibility, $\chi''(\omega)$.

2.1.2 Power Series of the Susceptibility

With the macroscopic approach of the preceding subsection, the susceptibility has been introduced to describe the interaction processes between electromagnetic radiation and a (simplified) material system. In this picture, the general frequency behavior of the material response is deduced and effects like absorption are introduced in a straightforward way. However, the concept of susceptibility allows to describe much more complex phenomena in light-matter interaction. Especially when considering intense light fields as emitted by short-pulsed lasers, the simple oscillator picture is not sufficient. Furthermore specific material properties as for instance the detailed electronic band structure are not accounted for in the model, despite their obvious relevance with regard to, e.g., resonance frequencies, and thus to the frequency behavior of different solids. To develop a more precise description of the light-matter interaction, the polarization $\mathbf{P}$ is expressed as a power series in the field strength $\mathbf{E}$. This defines higher-order coefficients of χ with

$$\mathbf{P}(t) = \epsilon_0 \left(\chi^{(1)}\mathbf{E}(t) + \chi^{(2)}\mathbf{E}^2(t) + \chi^{(3)}\mathbf{E}^3(t) + \cdots \right). \tag{2.9}$$

The validity of this time-domain description is limited to the case of a negligible frequency dependency of the coefficients $\chi^{(N)}$ [64], as usually given over the frequency bandwidth of light emitted by a laser with energies being far away from the optical resonances. Furthermore, to ensure the convergence of equation (2.9), the electrical field strength must not be too large. The experimental conditions found throughout this work result in maximal power densities of about 10^8 W/cm^2, significantly below the critical values on the order of 10^{16} W/cm^2 [61].

To relate the coefficients $\chi^{(N)}$ to the properties of specific materials, a quantum mechanical description of the problem is helpful. With the tools of the density matrix approach and the formalism of perturbation calculation, real-world behavior of light-matter interaction may be described with high accuracy. The treatment discussed here follows [61] and [65]. Starting point for the quantum mechanical description is the definition of the Hamilton operator

$$\hat{H} = \hat{H}_0 + \hat{V}(t), \tag{2.10}$$

where $\hat{H}_0$ denotes the Hamiltonian for a free atom and $\hat{V}(t) = -\hat{\boldsymbol{\mu}}\mathbf{E}(t)$ represents the interaction of the atom with the electrical field. Here, $\hat{\boldsymbol{\mu}} = -e\hat{\boldsymbol{r}}$ is the electric dipole moment operator with $\hat{r}$ expressing the position operator. Next, a wavefunction $\Psi_s(\mathbf{r}, t)$ is defined, which describes the quantum mechanical properties of the system in a state s. The wavefunction can be represented in terms of the basis functions of $\hat{H}_0$, $\Psi_s(\mathbf{r}, t) = \sum_n C_n^s(t) u_n(\mathbf{r})$, which are energy eigensolutions of $\hat{H}_0 u_n(\mathbf{r}) = E_n u_n(\mathbf{r})$. Here, $C_n^s(t)$ denotes the probability amplitudes. The density matrix $\hat{\rho}$ is now defined as $\rho_{nm} = \sum_s p(s) C_m^{s*} C_n^s$ with $p(s)$ expressing the probability to find the system in state s, $\sum_s p(s) = 1$. Using the Schrödinger's equation to describe the time evolution of the probability amplitudes, it follows for the time evolution of ρ_{mn}

$$\dot{\rho}_{nm} = -\frac{i}{\hbar}[\hat{H}, \hat{\rho}]_{nm} - \gamma_{nm}\left(\rho_{nm} - \rho_{nm}^{\text{eq}}\right). \tag{2.11}$$

For this expression, $p(s)$ is considered as time-independent. Time-dependent effects are included by a phenomenological damping term, which indicates that ρ_{nm} relaxes to its equilibrium value ρ_{nm}^{eq} at rate γ_{nm}, thereby $\rho_{nm}^{\text{eq}} = 0$ for $n \neq m$.

Since in general equation (2.11) cannot be solved analytically for physical systems of some complexity, a perturbation approach is chosen to describe the evolution of the system. For this, the density matrix elements are expanded in a power series around a parameter $0 \leq \lambda \leq 1$ which characterizes the strength of the perturbation,

$$\rho_{nm} = \rho_{nm}^{(0)} + \lambda\rho_{nm}^{(1)} + \lambda^2\rho_{nm}^{(2)} + \cdots . \tag{2.12}$$

Combining (2.11) and (2.12) and considering terms of common power of λ, the single terms of $\rho_{nm}^{(i)}$ may be calculated,

$$\rho_{nm}^{(0)}(t) = \rho_{nm}^{\text{eq}} \tag{2.13a}$$

$$\rho_{nm}^{(1)}(t) = e^{-(i\omega_{nm}+\gamma_{nm})t} \int_{-\infty}^{t} -\frac{i}{\hbar}[\hat{V}(t'), \hat{\rho}^{(0)}]_{nm} e^{(i\omega_{nm}+\gamma_{nm})t'}\, dt' \tag{2.13b}$$

$$\rho_{nm}^{(2)}(t) = e^{-(i\omega_{nm}+\gamma_{nm})t} \int_{-\infty}^{t} -\frac{i}{\hbar}[\hat{V}(t'), \hat{\rho}^{(1)}]_{nm} e^{(i\omega_{nm}+\gamma_{nm})t'}\, dt'. \tag{2.13c}$$

Following the definition of the susceptibility as given in equation (2.3), χ denotes the proportionality between the polarization $\mathbf{P}(t)$ and the electrical field $\mathbf{E}(t) = \sum_p \mathbf{E}(\omega_p) exp(-i\omega_p t)$. $\mathbf{P}(t)$ may also be expressed in terms of the expectation value of the induced dipole moment $\langle \boldsymbol{\mu}(t) \rangle = \sum_p \langle \boldsymbol{\mu}(\omega_p) \rangle \exp(-i\omega_p t)$ and the atomic number density N, so in first order [61]

$$\begin{aligned} \mathbf{P}^{(1)}(\omega_p) &= N \langle \boldsymbol{\mu}(\omega_p) \rangle^{(1)} = \epsilon_0 \chi^{(1)}(\omega_p) \mathbf{E}(\omega_p) \\ P_i^{(1)}(\omega_p) &= N \langle \mu_i(\omega_p) \rangle^{(1)} = \sum_j \epsilon_0 \chi_{ij}^{(1)}(\omega_p) E_j(\omega_p), \end{aligned} \tag{2.14}$$

with the second line expressing the Cartesian components of $\mathbf{P}$. Evaluating $\langle \boldsymbol{\mu}(t) \rangle^{(1)} = \text{tr}(\hat{\rho}^{(1)} \hat{\boldsymbol{\mu}})$, it follows with $\omega_{nm} = (E_n - E_m)/\hbar$

$$\chi_{ij}^{(1)}(\omega_p) = \frac{N}{\hbar} \sum_{nm} \rho_{mm}^{(0)} \left[\frac{\mu_{mn}^i \mu_{nm}^j}{(\omega_{nm} - \omega_p) - i\gamma_{nm}} + \frac{\mu_{nm}^i \mu_{mn}^j}{(\omega_{nm} + \omega_p) + i\gamma_{nm}} \right], \tag{2.15}$$

with the transition matrix elements $\boldsymbol{\mu}_{nm}$. Simplifying this expression by a restriction to isotropic media ($\mathbf{E}$ parallel to $\mathbf{P}$) with a ground-state population a such that $\rho_{aa}^{(0)} = 1, \rho_{mm}^{(0)} = 0$, the approximation

$$\chi^{(1)}(\omega_p) \approx \sum_n f_{na} \left[\frac{Ne^2/m}{(\omega_{na}^2 - \omega_p^2 - 2i\omega_p\gamma_{na})} \right] \tag{2.16}$$

holds. Here, $f_{na} = \left(2m\omega_{na}|\mu_{na}|^2\right) / \left(3\hbar e^2\right)$ denotes the oscillator strength for a transition of the system from level a to n. In this notation, the quantum mechanical description of the first-order susceptibility equals the result of the simple oscillator model, equation (2.4), modified by the occurrence of multiple resonance frequencies ω_{na} with a strength of f_{na}. Using this framework, also a more detailed expression for the absorption coefficient $\alpha(\omega)$ may be found. Assuming the case of linear absorption in a semiconductor, e.g. one-photon processes are considered to be dominant, first-order perturbation is sufficient for the description of $\alpha(\omega)$. Following [62], the free-carrier model relates equations (2.8) and (2.15) such that the absorption coefficient is given by

$$\alpha(\omega) = \frac{2|\mu_{cv}|^2\omega}{n_b c}\left(\frac{2m_r}{\hbar^2}\right)^{3/2}\sqrt{\hbar\omega - E_{\text{gap}}}\,. \tag{2.17}$$

In this expression, μ_{cv} is the transition matrix element for a transition from the valence band v to the conduction band c of the semiconductor with band gap energy E_{gap}. Thereby $m_r = m_e m_h/(m_e + m_h)$ denotes the reduced electron-hole mass (m_e, m_h are the electron and hole mass, respectively). The photon energy $\hbar\omega$ is assumed to exceed the band gap energy, i.e. $\hbar\omega \geq E_{\text{gap}}$.

Next to the linear effects of the susceptibility, also the higher-order terms of expression (2.9) are related to distinct light-matter interaction phenomena. In the following, specific second-order effects are introduced due to their role with regard to the THz generation and detection as presented in this work. However, before the resulting expressions are given, the second-order phenomena to be generally expected are briefly introduced. Considering monochromatic excitation as, e.g., given by a cw-laser, the temporal evolution of the field is expressed by $E(t) = E_0\, exp(-i\omega t) +$ c.c. for a certain field polarization and frequency. Thus, it follows for the polarization in second-order of the electrical field

$$\begin{aligned} P^{(2)}(t) &= \epsilon_0\chi^{(2)}E^2(t) \\ &= \epsilon_0\left[2\chi^{(2)}E_0E_0^* + \left(\chi^{(2)}E_0^2e^{-2i\omega t} + \text{c.c.}\right)\right]. \end{aligned} \tag{2.18}$$

The first term of this expression is related to a process denoted as optical rectification [66], resulting in a static electrical field. The terms in parenthesis refer to a signal at twice the input frequency, expressing the second-harmonic generation [67]. If the excitation field is composed of two cw electrical field components, the squaring of the field results in additional terms related to sum- and difference frequency generation processes [68]. To reflect the origin of the corresponding terms of the second-order sus-

ceptibility, a special notation has been established. Following [61], the expression $\chi^{(2)}(\omega_p + \omega_q; \omega_p, \omega_q)$ contains three arguments. The first entry denotes the constant sum of the involved field frequencies, the second and third refer to the individual fields. Hereby, ω_p and ω_q may also be negative. By this, all permutations of the fields are unambiguously accounted for when taking the square of $E(t)$. A general expression for the second-order term of the polarization is now derived in analogy to equation (2.14) [61],

$$\begin{aligned} P_i^{(2)}(\omega_p + \omega_q) &= N \langle\, \mu_i(\omega_p + \omega_q) \,\rangle^{(2)} \\ &= D \sum_{jk} \chi_{ijk}^{(2)}(\omega_p + \omega_q; \omega_p, \omega_q) E_j(\omega_p) E_k(\omega_q). \end{aligned} \tag{2.19}$$

Here D denotes the degeneracy factor which is equal to the number of distinct permutations of the applied field frequencies ω_p and ω_q.

With $\langle \boldsymbol{\mu}(t) \rangle^{(2)} = \mathrm{tr}(\hat{\rho}^{(2)} \hat{\mu})$ and additional calculations it follows

$$\begin{aligned} \chi_{ijk}^{(2)}(\omega_p + \omega_q; \omega_p, \omega_q) = \frac{N}{2\hbar^2} \sum_{lmn} \rho_{ll}^{(0)} \\ \Bigg\{ \frac{\mu_{ln}^i \mu_{nm}^j \mu_{ml}^k}{[(\omega_{nl} - \omega_p - \omega_q) - i\gamma_{nl}][(\omega_{ml} - \omega_p) - i\gamma_{ml}]} \\ + \frac{\mu_{ln}^i \mu_{nm}^k \mu_{ml}^j}{[(\omega_{nl} - \omega_p - \omega_q) - i\gamma_{nl}][(\omega_{ml} - \omega_q) - i\gamma_{ml}]} \\ + \frac{\mu_{ln}^k \mu_{nm}^i \mu_{ml}^j}{[(\omega_{mn} - \omega_p - \omega_q) - i\gamma_{mn}][(\omega_{nl} + \omega_p) + i\gamma_{nl}]} \\ + \frac{\mu_{ln}^j \mu_{nm}^i \mu_{ml}^k}{[(\omega_{mn} - \omega_p - \omega_q) - i\gamma_{mn}][(\omega_{nl} + \omega_q) + i\gamma_{nl}]} \\ + \frac{\mu_{ln}^j \mu_{nm}^i \mu_{ml}^k}{[(\omega_{nm} + \omega_p + \omega_q) + i\gamma_{nm}][(\omega_{ml} - \omega_p) - i\gamma_{ml}]} \\ + \frac{\mu_{ln}^k \mu_{nm}^i \mu_{ml}^j}{[(\omega_{nm} + \omega_p + \omega_q) + i\gamma_{nm}][(\omega_{ml} - \omega_q) - i\gamma_{ml}]} \\ + \frac{\mu_{ln}^k \mu_{nm}^j \mu_{ml}^i}{[(\omega_{ml} + \omega_p + \omega_q) + i\gamma_{ml}][(\omega_{nl} + \omega_p) + i\gamma_{nl}]} \\ + \frac{\mu_{ln}^j \mu_{nm}^k \mu_{ml}^i}{[(\omega_{ml} + \omega_p + \omega_q) + i\gamma_{ml}][(\omega_{nl} + \omega_q) + i\gamma_{nl}]} \Bigg\}. \end{aligned} \tag{2.20}$$

This extensive expression accounts for the various possible transitions induced by the two electrical fields involved in the excitation process. De-

pending on the resonance energies, only particular terms of (2.20) are dominant. More convenient equations are obtained when only resonant or nonresonant excitation processes are assumed. These expressions are then to a certain extend suitable to calculate the strength of the specific second-order effects [69]. However, when applying this concept to the calculation of $\chi^{(2)}$ over the full frequency spectrum for a certain material, non-physical effects may influence the calculation. Especially divergences at the zero-frequency limit were not understood until a careful consideration of intra- and interband effects was included in the description [70]. A general formalism for the calculation of the optical response of semiconductors in the independent-particle approximation, applicable to arbitrary crystal classes, has been introduced in [71] in a velocity-gauge framework. Also based on a perturbation approach, this treatment allows for a full band structure calculation of χ [72, 73]. A mathematically more simple expression was derived in [74] utilizing a length-gauge analysis to expand the standard formalism of the semiconductor Bloch equations (e.g. [62]) by including intraband effects. This formalism has shown to be very useful to describe the second-order optical response of semiconductors [75].

Based on this description, two second-order effects relevant in the remainder of this work are introduced. First, the occurrence of all-optically induced current flows is described using a difference frequency generation process ($\chi^{(2)}_{ijk}(0;\omega,-\omega)$, see subsection 2.3.1). Second, the electro-optic effect is utilized for the detection of THz signals, which is based on $\chi^{(2)}_{ijk}(-\omega;\omega,0)$ (see subsection 2.3.2). Especially for the first, a formalism following equation (2.20) is not sufficient to describe the susceptibility since the zero-frequency limit of $\chi^{(2)}$ is regarded. A detailed description of the more elaborated approach as given in [75] exceeds the introductory character of this chapter. In the following, only a phenomenological description of $\chi^{(2)}$ is presented.

Following [75], also the susceptibility expresses the separation into inter- (superscript "ter") and intraband (superscript "tra") effects,

$$\chi^{(2)}(\omega_\Sigma;\omega_p,\omega_q) = \chi^{(2)\mathrm{ter}}(\omega_\Sigma;\omega_p,\omega_q) + \chi^{(2)\mathrm{tra}}(\omega_\Sigma;\omega_p,\omega_q). \tag{2.21}$$

Thereby both terms are complex values and $\omega_\Sigma = \omega_p + \omega_q$. For $\chi^{(2)\mathrm{tra}}$, a further decomposition is possible,

$$\begin{aligned}&\chi^{(2)\mathrm{tra}}(\omega_\Sigma;\omega_p,\omega_q)\\ &= \frac{\eta^{(2)}(\omega_\Sigma;\omega_p,\omega_q)}{(-i\omega_\Sigma)^2} + \frac{\sigma^{(2)}(\omega_\Sigma;\omega_p,\omega_q)}{(-i\omega_\Sigma)} + \widetilde{\chi}^{(2)\mathrm{tra}}(\omega_\Sigma;\omega_p,\omega_q).\end{aligned} \tag{2.22}$$

In this expression, $\eta^{(2)}$ is purely imaginary, $\sigma^{(2)}$ and $\widetilde{\chi}^{(2)\mathrm{tra}}$ are complex.

With equations (2.21) and (2.22), the behavior of the susceptibility under resonant and nonresonant excitation is summarized as follows.

Resonant: When $\hbar\omega > E_{\text{gap}}$, both real and imaginary parts are included in (2.21), thus an absorptive behavior of the susceptibility is given and charge carriers may be generated. Under appropriate conditions of the exciting field, the light absorption gives rise to current flows as described in more detail in subsection 2.3.1. Especially the current related to $\sigma^{(2)}$, denoted as shift current, is of importance for the remainder of the work. For monochromatic excitation, i.e. $\omega_p = -\omega_q$, the imaginary part of $\sigma^{(2)} = \sigma^{(2),R} + i\sigma^{(2),I}$ vanishes and the second term of equation (2.22) is purely imaginary.

Nonresonant: When the photon energy is below the band gap, $\hbar\omega < E_{\text{gap}}$, $\eta^{(2)}$, the real part of $\sigma^{(2)} = \sigma^{(2),R} + i\sigma^{(2),I}$ and the imaginary parts of $\chi^{(2)\text{ter}}$ and $\widetilde{\chi}^{(2)\text{tra}}$ vanish. Consequently, $\chi^{(2)}$ is purely real as expected for the susceptibility in the nonresonant case. Thus, (2.21) simplifies for the electro-optic effect to

$$\chi^{(2)}(\omega;\omega,0) = \chi^{(2)\text{ter}}(\omega;\omega,0) + \frac{\sigma^{(2),I}(\omega;\omega,0)}{\omega} + \widetilde{\chi}^{(2)\text{tra}}(\omega;\omega,0). \tag{2.23}$$

This closes the section about the semiconductor susceptibility. The description of basic light-matter interaction is utilized to introduce the important quantities for the remainder of the work. Equation (2.17) describes the light absorption process, relevant for the generation of free carriers in the semiconductor material. Based on this, THz generation and detection is possible as will be described in section 2.3. Expressions (2.21) and (2.22) are the basis for the second-order effects which may also be utilized for THz detection and generation. Since in any case well defined excitation conditions are a prerequisite for a thorough investigation of the occurring effects, the following section outlines the properties of the light source used for the experiments.

2.2 Ti:Sa Femtosecond Laser

In the following section, a fundamental tool utilized throughout this thesis is introduced: the Ti:Sa femtosecond laser. Detailed descriptions about the operation principle of lasers may be found in various text books, e.g. [76, 77]. Nevertheless, due to the key role of certain features of laser emission for the remainder of this thesis, a brief summary of the most

important properties will be given. Especially the principle of optical frequency combs is of utmost importance in the following chapters, as well as the noise contribution inherent to the emitted light.

2.2.1 Basic Properties

To utilize distinct terms of the semiconductor susceptibility as given in equation (2.9) for the generation and detection of THz radiation, extensive control of the electromagnetic fields interacting with the material is necessary. Moreover, the stimulation of higher-order terms of χ is only possible using high-intensity fields. With the principle of the laser [78,79], a source of coherent, well defined radiation is given. Furthermore, highest electrical field strengths may be realized by locking appropriate modes oscillating in the laser cavity to each other [80, 81] and thus forming very short light pulses with high peak power. Depending on the laser type, various mode-locking techniques may be realized. In this work, a solid-state laser based on a titanium-doped sapphire crystal (Ti:Sa) used as gain medium [82] is utilized. Here, a passive mode-locking process is employed, originating from a Kerr-induced self-focusing of the light propagating in the oscillator [83, 84]. This technique allows for the generation of ultrashort optical pulses, reaching down to 5 fs full width at half maximum (FWHM) [85,86] and providing ultrabroad optical spectra [87].

With the specific device used in this work (Coherent Micra-10), pulses with a FWHM of 15 fs at a spectral width of 75 nm are specified (see table 2.1 for manufacturer specifications of certain laser parameters). These parameters can only be reached by incorporating a pulse compressing unit (Coherent CPC) into the setup, compensating the chirp induced by optical components inside the laser cavity via negatively chirped mirrors. Corresponding autocorrelation traces as well as a spectral decomposition of such short laser pulses are given in section 3.4. To ensure most stable operational conditions, the majority of experimental results presented in the following chapters are obtained using a smaller bandwidth of about 30 nm and pulses with a FWHM on the order of 100 fs. Nevertheless,

Coherent Micra-10 Ti:Sa	
Description	Specification
Center Wavelength	800 nm
Bandwidth (FWHM)	75 nm
Pulse Width (FWHM)	15 fs
Average Power	750 mW
Pulse Repetition Rate	(76 $\pm$ 0.5) MHz

Table 2.1 Manufacturer specifications for certain parameters of the Coherent Micra-10 Ti:Sa laser used throughout this work.

also at 100 fs pulse width at a repetition rate of 76 MHz, peak powers on the order of 100 kW are reached with the given laser system. This ensures a sufficient excitation of the second-order terms of the susceptibility to utilize the related phenomena for various purposes as described in section 2.3.

2.2.2 Optical Frequency Comb

The repetitive emission of light pulses by a mode-locked laser immediately allows to introduce a concept of great importance for metrology: the optical frequency comb [88–91]. To outline the basic features of such a comb, a brief description following [89, 92] is given. A comparable workout has been published in [A1].

For a light pulse circulating in an optical resonator with a cavity length L, a round-trip time $T = v_\mathrm{g}/2L$ results. Here, v_g denotes the group velocity of the pulse with a certain carrier frequency f_c. Whenever the light pulse hits the output coupler mirror of the resonator, a fraction of the light is emitted as laser radiation. Thus, the round-trip time defines the repetition rate $f_\mathrm{rep} = 1/T$ of the laser, see figure 2.2 (a). Going from a time-domain description to frequency domain, the spectral representation of an infinite series of regularly emitted laser pulses equals a series of Dirac delta functions which are separated in frequency by the value of f_rep, refer figure 2.2 (b). This defines the so called optical frequency comb. For typical pulse shapes, the comb envelope is centered at the carrier frequency f_c and its spectral bandwidth is related to the minimal pulse width τ via the time-bandwidth product. With the parameters given in table 2.1, the laser used in the following spans a frequency comb from 355 THz to 395 THz.

The absolute positions of those comb modes are, in the case of an optical frequency comb, influenced by an additional parameter, the carrier-envelope offset frequency f_CEO. Since the phase velocity of the carrier wave, v_ph, usually differs from v_g, consecutive light pulses show a phase shift $\Delta\varphi = f_\mathrm{c}\left(\frac{L}{v_\mathrm{g}} - \frac{L}{v_\mathrm{ph}}\right)$ in the electrical field of the carrier wave with respect to the envelope maximum. In frequency domain, this phase shift is equal to a shift of the comb modes of the optical frequency comb by $f_\mathrm{CEO} = \Delta\varphi/T$. Thus, the frequency $f_{n,\mathrm{oc}}$ of a single comb mode n_opt of the optical frequency comb is given by

$$f_{n,\mathrm{oc}} = n_\mathrm{opt} f_\mathrm{rep} + f_\mathrm{CEO}, \tag{2.24}$$

with n_opt being a large ($\approx 10^5$ - 10^6) integer number.

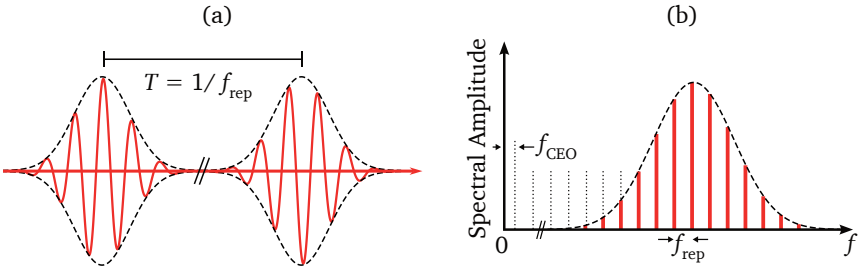

Figure 2.2 (a) In time-domain, the emission of the laser equals a train of pulses with a repetition rate f_{rep}. (b) In frequency domain, the pulsed nature of the emission is represented by a comb structure. The optical frequency comb consists of distinct modes, separated by f_{rep}. The modes are shifted from multiples of f_{rep} by the carrier-envelope offset frequency f_{CEO}.

2.2.3 Noise Effects

The process of lasing is generally regarded to result in the emission of a well-defined, stable output signal. However, this process underlies a variety of influences, significantly affecting the laser's emission parameters. Fluctuations of the latter act as noise contributions in a measurement process which possibly restrict the usability of the device. This is especially true for applications in the field of metrology, where highest measurement precision and accuracy is required. In this subsection, the fundamental noise contributions of a mode-locked laser with regard to their influences on the optical frequency comb are introduced.

Laser noise is a result of two different contributions, as discussed in detail in [93]. One the one hand, there is technical noise, resulting from the mechanical design of the apparatus. Here, optimization techniques may be applied to overcome hampering effects on the measurement setup. On the other hand, fundamental noise governed by the occurrence of basic physical effects determines a principal limitation for all optimization approaches. It is instructive to visualize the most simple type of laser for the understanding of the noise effects. Regarding the output of a single-frequency cw laser, only two parameters have to be considered: intensity and phase noise. Both show a different behavior. The first one is influenced by a "restoring force" due to the gain process, tending to pull the output power towards a steady-state value. For the second, no reference exists so that the phase undergoes a random walk. This results in a finite emission linewidth of the laser. However, even if technical contributions are reduced, both intensity and phase noise underlie quantum-based effects [94]. In the case of intensity noise, quantum fluctuations of the

light field result in the so called shot noise. The phase noise is affected by two fundamental processes, namely spontaneous emission and losses inside the laser cavity (as, e.g., occurring at the output coupler mirror). The broadening of the emission linewidth due to those effects may be described using the Schawlow-Townes formula [78]. Besides this theoretical limit, a variety of effects contribute to the technical noise inherent to the obtained linewidth. For instance, noise properties of the pump source directly transfer into the lasing process. Additionally, changes of the cavity length due to mirror vibrations highly affect the phase stability, as well as temporal fluctuations in the gain medium. Moreover, a coupling between intensity noise and phase noise occurs, as for instance via the Kerr-effect. Thus, even the most simple laser system shows a complex noise scheme.

In the case of mode-locked lasers, the picture significantly complicates [95]. Here, different emission parameters have to be taken into account due to the spectral width and the pulsed nature of the output signal. Usually, the pulse energy, the gain, the optical phase of the central line, the pulse duration, the temporal position of the pulses and fluctuations of the carrier frequency are taken into account. A complex interplay between the fluctuations of these parameters has to be considered. Using the given or a comparable set of parameters, analytic models have been introduced to describe the resulting dependencies for mode-locked lasers [96–99]. A detailed description is a matter of ongoing research.

For the practical work using optical frequency combs in the way described in section 2.3, the timing jitter of consecutive pulses plays a major role. The temporal fluctuations of the individual pulses from their undistorted position are generally expressed with the term “timing phase noise” [93]. Similar to the optical phase noise (i.e. fluctuations of the optical carrier frequency), also the timing phase noise does not underlie a restoring force in a passively mode-locked laser and a random-walk-like behavior of the repetition rate is expected. This results in a broadening of the individual comb lines. In the quantum-limited case, it has been shown that the comb-line width around the center frequency is close to the Schawlow-Townes level, reaching the order of μHz [96, 100]. This is true for a typical Ti:Sa laser when amplitude-to-phase conversion is totally neglected. However, determined by the degree of suppression of the occurring amplitude fluctuation, the linewidth easily increases by factors of 100 to 10000 and by this even may reach Hz-level. For a free-running Ti:Sa laser, a linewidth on the order of mHz has been observed [101]. Furthermore, a frequency-dependent behavior of the comb-mode width is predicted. For the comb line n around the center frequency of the optical beam, the width scales with $n^{2/p}$. Thereby p ranges from 1 to 3, according to the dominant noise effects inherent to the laser system [102].

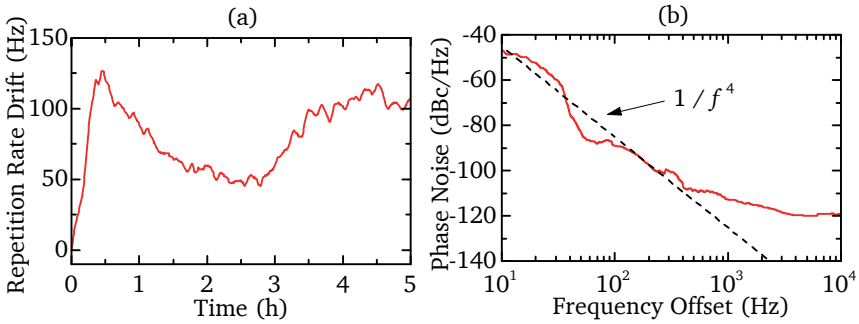

Figure 2.3 (a) Drift of the laser repetition rate over a 5 h period. (b) Timing phase noise of the free-running Ti:Sa laser measured at the fundamental repetition rate frequency of 76 MHz.

To visualize the effect of the various noise contributions on the repetition rate of the laser, figure 2.3 (a) shows the measured value of the repetition rate for the free-running Ti:Sa laser used in this work over a time interval of several hours. After a warm-up time of 0.5 h, a drift of the repetition rate over more than 60 Hz per hour occurs, reflecting a random walk-like behavior as expected. A detailed investigation of the noise properties is given in figure 2.3 (b). Here, a measurement of the timing phase noise is shown. Utilizing a signal analyzer (Agilent E4440A), the phase noise spectrum of the fundamental repetition rate of 76 MHz measured with a fast photodiode is evaluated. The measurement agrees with the $1/f^4$-dependency associated with the random walk behavior of the temperature-induced fluctuations of the laser resonator [96, 103].

Using external controls, the repetition rate of a Ti:Sa laser may be phase-locked to a reference signal [104, 105]. For this, following [95], the repetition rate is measured at a higher harmonic to reduce the influence of amplitude-to-noise conversion. The measured signal is then compared to the reference and via a feedback loop, piezo transducers are triggered to compensate for the cavity length fluctuations. Using such a technique, the phase noise spectrum as shown in figure 2.3 (b) is significantly reduced in the lower frequency region. As demonstrated in [105], nearly quantum-limited timing jitter may be obtained for a Ti:Sa laser. The performance of the repetition rate stabilization is hereby determined by the properties of the electronics used for the phase locking and the cavity stabilization process.

The Coherent Micra-10 Ti:Sa laser used in this work is equipped with a locking unit (Mira Synchro-Lock AP) utilizing the technique just described. The phase locking is performed at the 9^{th} harmonic. Nevertheless, in chap-

ter 3, an alternative approach is demonstrated to overcome limitations of the measurement accuracy due to the repetition rate fluctuations. Thus, unlike noted otherwise, the experiments shown in the following are obtained without using the stabilization unit.

2.3 Employing the Semiconductor Susceptibility for Terahertz Generation and Detection

As demonstrated in section 2.1, the light-matter interaction in semiconductors reveals a multi-faceted response. Depending on the properties of the semiconductor or the light field, the response reaches from the creation of charge carriers due to absorption effects to feedback reactions, modifying the parameters of the incident light. In the following, some of these features are analyzed in detail and evaluated with regard to their properties for the generation and detection of THz radiation. Parts of subsection 2.3.2 follow the description as given in [A1].

2.3.1 Terahertz Generation

To generate THz radiation, a variety of mechanisms are at hand. Brief reviews are given in [3, 17]. The presented THz sources may be classified according to their generation principle:

- All-electronic oscillators and amplifiers (e.g. frequency multiplier, Gunn- or IMPATT-diodes)
- THz lasers (e.g. quantum cascade lasers, gas lasers)
- Free electron sources (e.g. Gyrotrons, Backward Wave Oscillators, Free Electron Lasers)
- Optical THz generation (e.g. photoconductive antennas, nonlinear effects in matter)

This subsection reviews the present state of knowledge with respect to the last point, the optical generation processes. Here, the description is narrowed down to phenomena related to ultrafast carrier generation in a semiconductor material like GaAs. The basic principle is simple. A movement of the optically excited carriers equals a current flow $\mathbf{J}$, whose temporal behavior determines the electromagnetic field $\mathbf{E}_{\mathrm{THz}}$ radiated into free space,

$$\mathbf{E}_{\mathrm{THz}}(t) \propto \frac{\mathrm{d}\mathbf{J}(t)}{\mathrm{d}t} \,. \tag{2.25}$$

To induce an acceleration of the charge carrier, different mechanisms have to be considered which result in specific characteristics of the emitted electrical fields. Relevant for the remainder of this work are two particular all-optical effects, traced back to intrinsic semiconductor properties. On the one hand, drift- and diffusion-based current flows occur. On the other hand, coherent control of an induced carrier motion is realized by utilizing the properties of the pump light and the crystal structure.

Absorption-Based Effects: Drift and Diffusion Currents

When by ultrafast optical excitation of a semiconductor surface charge carriers are generated, ultrafast transport dynamics of the latter may be observed. The reason for this lies in the broken symmetry condition at the air/semiconductor interface, which affects the carriers in different ways. Primarily, two processes are relevant:

i. Already 1931 a current flow of photoexcited carriers in CuO_2 crystals and other semiconductor materials has been reported [106–108], in the following called photo-Dember (PD) currents. The origin of this current is found in the different mobilities and, correspondingly, the different diffusion constants of electrons and holes. Regarding individual electron-hole pairs of the excited carrier ensemble, a spatial separation of the charge carriers results. Without the influence of the material's interface, no net current flows due to the isotropic diffusion behavior. However, since the carrier diffusion takes place in a hemisphere inside the crystal centered around the excitation spot, the center of mass of electrons and holes separates and a charge dipole perpendicular to the material surface forms (refer figure 2.4 (a)).
The PD current is a diffusion-based current.

ii. Regarding the band structure of semiconductors, local differences are observed which are especially pronounced at the semiconductor surfaces. Here, a pinning of the Fermi level at the energetic position of occupied surface states occurs [109]. This bends the energy bands in the vicinity of the surface, forming a charge depletion region and thus a built-in static electrical field. The charge depletion field is directed normal to the surface, accelerating optically excited carriers [110, 111]. The field-induced carrier drift separates the electron-hole pairs. This equals a current flow which is denoted as surface-field (SF) current (see figure 2.4 (b)).
The SF current is a drift-based current.

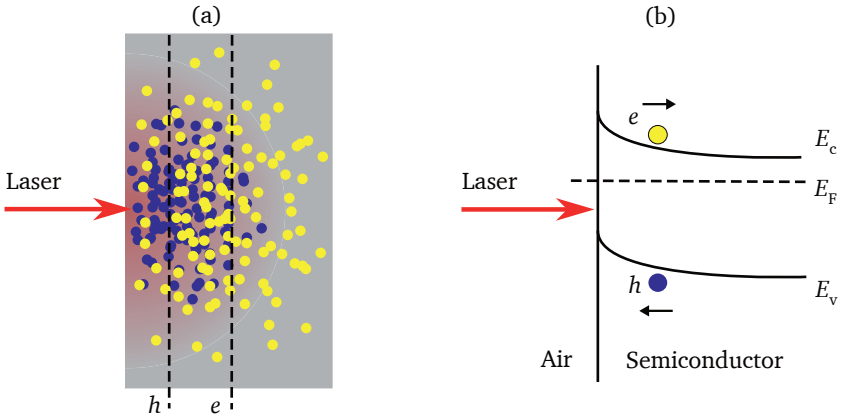

Figure 2.4 (a) Photo-Dember current: Due to the different velocities of electrons (e, yellow) and holes (h, blue) the corresponding charges' center of mass separate. This equals a net current flow perpendicular to the surface. (b) Surface-field current: The bending of conduction and valence band (E_c, E_v) at the semiconductor-air interface results in a surface field which separates optically induced electrons and holes. E_F denotes the Fermi level.

To investigate the carrier movement in detail, a variety of studies has been performed. Different theoretical models are proposed, based on diffusion equations, drift-diffusion treatments [112], hydrodynamic models [113], quantum-mechanical descriptions [114] or Monte Carlo approaches [115, 116]. Using these models, different semiconductors like GaAs, GaSe, InP, InAs and others have been analyzed to extract the basic dependencies of the current contributions. An introductive approach to describe the carrier distribution in time and space is given in the drift-diffusion equations for electrons and holes following [112]. They present a simple formulation of the Boltzmann transport equation, derived in the relaxation-time approximation. A one-dimensional continuity equation describes the carrier concentration distribution and temporal evolution, $n_i(z,t)$, along the z-direction perpendicular to the surface,

$$\frac{\partial n_i(z,t)}{\partial t} = G(z,t) + \frac{\partial}{\partial z}\left\{D_i(z,t)\frac{\partial n_i(z,t)}{\partial z}\right\} \pm \frac{\partial}{\partial z}\left\{\mu_i(z,t)E(z,t)n_i(z,t)\right\}. \tag{2.26}$$

In this expression, $i = (e,h)$ denotes the carrier type, G is the optical generation term, μ_i describes the carrier mobility, $D_i = k_B T_i \mu_i / e$ is the diffusion coefficient with the Boltzmann constant k_B and the carrier temperature T_i. During their motion in the surface field region the photocarri-

ers screen the surface field. Thus, the effective field acting on the carriers has to be recalculated for each step in time and space,

$$\frac{\partial E(z,t)}{\partial z} = \frac{e}{\epsilon_0 \epsilon} \left\{ n_h(z,t) - n_e(z,t) \pm n_d(z) \right\}, \tag{2.27}$$

with n_d being the doping concentration of the material. The starting point of these calculations is given by $E(z = 0)$ resembling the surface-space-charge field ($\approx 10^5$ V for intrinsic GaAs), decreasing monotonically over the depletion width with a length on the order of µm. Both values are deduced from the material's band bending following [117].

Although more elaborate models are necessary for a comprehensive description of the current behavior, already in expression (2.26) the most important dependencies for this work are included. First, it is shown that the carriers on the semiconductor surface tend to drift and diffuse simultaneously. Depending on the material parameter and excitation energies, an overall current flow dominated by PD or SF currents or a mixture of both may be obtained [118, 119]. For intrinsic GaAs at the excitation conditions utilized in this work, the SF current is the dominant current contribution [118]. Second, the direction of the current flow depends on the sign and strength of the surface field, influenced by the doping level [116, 120–122]. Third, according to the generation term, the rise time of the current flow is determined by the excitation laser pulse, with

$$G(z,t) = I(t)\alpha(1-R)e^{-\alpha z}. \tag{2.28}$$

Here, $I(t)$ denotes the laser intensity, α the absorption coefficient according to equation (2.17) and R the reflection coefficient at the material surface. The fast rise time of the current results in a broadband emission spectrum of the electrical field according to equation (2.25). Fourth, high-intensity excitation of the material is also covered by equation (2.26) which, extended by corresponding coupling terms, also models phonon [123,124] and plasmon [125,126] oscillations. The overall power scaling of the net current as shown in [115, 127] is based on more elaborated models, giving roughly linear power dependencies of the emitted THz amplitude for lower excitation densities. At high excitation densities, a saturation effect is predicted due to the shielding of the surface field by the induced carriers.

Second-Order Nonlinear Effects: Coherently Controlled Currents

Polarization in matter is attributed to a spatial separation of real and virtual charge carriers. Due to this, a temporal variation of the polarization

$\mathbf{P}$ equals to a modified spatial charge distribution. This denotes a current flow $\mathbf{J}$, whose temporal behavior is given by

$$\mathbf{J}(t) = \frac{\partial \mathbf{P}(t)}{\partial t}. \tag{2.29}$$

With equation (2.9), the temporal evolution of $\mathbf{P}(t)$ is related to an external electrical field $\mathbf{E}(t)$ via the susceptibility tensor χ. An elaborate description for the behavior of the latter in second order has been given in subsection 2.1.2. Following [75] and [128], equations (2.21) and (2.22) may be summarized to a general expression for $\chi^{(2)}$,

$$\begin{aligned}&\chi^{(2)}(\omega_\Sigma;\omega_p,\omega_q)\\ &= \chi^{(2)\text{Rect}}(\omega_\Sigma;\omega_p,\omega_q) + \frac{\eta^{(2)}(\omega_\Sigma;\omega_p,\omega_q)}{(-i\omega_\Sigma)^2} + \frac{\sigma^{(2)}(\omega_\Sigma;\omega_p,\omega_q)}{(-i\omega_\Sigma)}.\end{aligned} \tag{2.30}$$

In the following, the excitation of a semiconductor using a monochromatic field $\mathbf{E}(t) = \mathbf{E}_0 e^{-i\omega t} + \mathbf{E}_0^* e^{i\omega t}$ is assumed. Then, the first term of (2.30) describes the nonresonant component of the excitation. A static polarization occurs, that arises due to a displacement of virtually excited carriers. This component is nonzero for all ω, since there are always pairs of valence and conduction bands with an energy separation exceeding the photon energies. The other two terms are associated with resonant excitation, $\hbar\omega > E_{\text{gap}}$. They go along with the generation of carriers in the corresponding energy bands and, thus, may lead to electrical currents. Hereby the second term is related to the tensor $\eta^{(2)}$, which is antisymmetric in the last two Cartesian indices (i.e., $\eta^{(2)}_{abc} = -\eta^{(2)}_{acb}$) [75]. Due to this symmetry condition, in zinc-blende structures like bulk GaAs, GaP or ZnTe it vanishes and thus will not be treated further in this work. For completeness, the corresponding current flow is denoted as injection current. The third term of (2.30) reflects a spatial shift of the center of charge during excitation. This may be exemplary visualized for GaAs. Valence and conduction bands are separated in real space, with the former located around the arsenic atoms and the latter at the gallium atoms [129]. Thus, by optical excitation, a shift of the charge carriers on the order of a bond length occurs on femtosecond time scales. Depending on the crystal symmetry and the polarization of the electrical field, thereby certain transition paths exhibit preferred transition probabilities. Using figure 2.5, this behavior is schematically demonstrated. There, the four Ga neighbors of an As atom in the zinc-blende structure of GaAs are shown. The coordinate system is given such that the x-axis equals the crystallographic $[001]$-direction, $y = [1\bar{1}0]$ and $z = [110]$. For a light field polarized in, e.g., x-direction, the

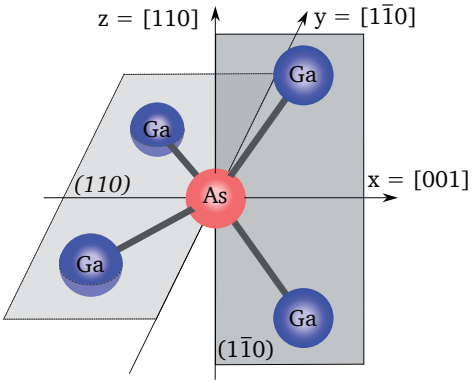

Figure 2.5 Schematic model of the atomic arrangement of a GaAs crystal in a coordinate system corresponding to certain directions of the zinc-blende material structure. In grey, the (110) and (1$\bar{1}$0)-plane are indicated.

transition probabilities for an electron to move from the As atom to one of the four neighbor atoms are equal and by this no net current flow results in the crystal. However, a polarization of the field along the y-direction would interact with the bonds in the (110)-plane. The excited electrons in the crystal primarily move along a common direction, which results in an overall current flow along the x-axis.

In the following, this behavior is described in a more formal way for pulsed excitation in the resonant case [128]. A field $\mathbf{E}(t) = \mathbf{E}_{\text{env}}(t)e^{-i\omega t} + \mathbf{E}^*_{\text{env}}(t)e^{i\omega t}$ with a pulse envelope function $\mathbf{E}_{\text{env}}(t)$ is assumed. Combining equation (2.29) with the second-order term of expression (2.9) utilizing the previously discussed GaAs symmetry conditions for (2.30), two current contributions remain when regarding the difference-frequency generation,

$$\begin{aligned}\mathbf{J}^{(2)}(t) &= 2\epsilon_0\chi^{(2)\text{Rect}}\frac{\partial}{\partial t}\left(\mathbf{E}_{\text{env}}(t)\mathbf{E}^*_{\text{env}}(t)\right) + 2\epsilon_0\sigma^{(2)}\mathbf{E}_{\text{env}}(t)\mathbf{E}^*_{\text{env}}(t) \\ &= \mathbf{J}^{\text{Rect}}(t) + \mathbf{J}^{\text{Shift}}(t). \end{aligned} \tag{2.31}$$

They are denoted as rectification (Rect) and shift currents. In this equation which neglects scattering effects, the temporal behavior of the currents is visualized. The rectification current follows the time derivative of the optical pulse envelope whereas the shift current follows the envelope directly. For resonant excitation and a comparable light-matter interaction length, the shift current dominates the overall current flow, being two orders of magnitude larger than the rectification current [128, 129]. The spatial behavior of the shift current is determined by the symmetry properties of the shift current tensor $\sigma^{(2)}$. For a material of zinc-blende structure, only specific tensor elements are nonzero. These values are listed in table (2.2) for three different axis systems, corresponding to differently cut crystals.

(001) $x, y, z = [100], [010], [001]$	(110) $x, y, z = [001], [1\bar{1}0], [110]$	(113) $x, y, z = [1\bar{1}0], [33\bar{2}], [113]$
σ_{xyz} , σ_{xzy}	σ_{xyy} , σ_{xzz}	σ_{xxy} , σ_{xyx} , σ_{xxz} , σ_{xzx}
σ_{yxz} , σ_{yzx}	σ_{yxy} , σ_{yyx}	σ_{yxx} , σ_{yyy} , σ_{yzz} , σ_{yyz} , σ_{yzy}
σ_{zxy} , σ_{zyx}	σ_{zxz} , σ_{zzx}	σ_{zxx} , σ_{zyy} , σ_{zzz} , σ_{zyz} , σ_{zzy}

Table 2.2 Nonzero elements of the shift current tensor $\sigma^{(2)}$ in zinc-blende symmetry for three different axis systems grouped after the first index (current flow direction). For each axis system, the relative strengths of the elements are equal. Due to reasons of clarity, the superscript $^{(2)}$ for the tensor elements is omitted.

The column names given in parentheses determine the surface plane of the crystal.

Evaluating $\mathbf{J}^{\text{Shift}}$ of expression (2.31) for a certain current flow direction using table (2.2), it follows e.g. with $\sigma^{(2)}_{yxy} = \sigma^{(2)}_{yyx}$ for the shift current along the y-direction in (110)-cut GaAs [130]

$$J_y^{\text{Shift}}(t) = 4\epsilon_0 \sigma^{(2)}_{yxy} E_x^{\text{env}}(t) E_y^{\text{env}}(t) \cos(\varphi_x - \varphi_y). \tag{2.32}$$

Here, $\varphi_{(x,y)}$ denote the phases of the light fields polarized along (x, y). The cosine term in this equation is of highest importance for the current generation process. With the dependency on the relative phase, it is possible to coherently control the sign of the current flow along the y-direction. For instance, by choosing the light fields to be in phase ($\varphi_x = \varphi_y$, linearly polarized light oriented at an angle of +45° with respect to the x-axis of the crystal), a current flow in positive y-direction is induced. If the light fields are out of phase by 180° ($\varphi_x = \varphi_y + \pi$, linearly polarized light oriented at -45° to the x-axis), the current flow is directed into the negative y-direction. In the picture of figure 2.5, this corresponds to an excitation along the one or the other bond direction in the (110)-plane of the crystal.

2.3.2 Terahertz Detection

For the detection of THz radiation, nowadays many different techniques may be employed [131]. It depends on the particular experimental requirements to decide which technique suits best. In the following paragraphs two specific detection schemes are introduced, which are widely

used for spectroscopic applications and furthermore allow for high-precision metrology as will be demonstrated in chapter 3. First, a description of photoconductive (PC) detection is given, based on the absorption of light in a semiconductor material. Second, electro-optic (EO) detection is introduced, utilizing light-matter interaction described by second-order terms of the susceptibility tensor.

Absorption-Based Effects: Photoconductive Detection

A milestone in the history of THz research was reached in the 1980s, when photoconductive antennas (PCAs) were introduced as emitters and detectors for THz radiation [132–135]. The operation principle of such PCAs is based on the optical injection of charge carriers. Due to the rapid dynamics of those carriers, PCAs allow for the observation of high-frequency electro-magnetic phenomena, taking place on the picosecond and even femtosecond timescale. Today's PCAs utilized for excitation wavelengths of 800 nm usually consist of a low-temperature grown gallium arsenide substrate (LT-GaAs), onto which metal contacts are evaporated. Via the contact electrodes, a voltage can be applied which accelerates the optically induced carriers and an electromagnetic signal is radiated into free space. In such a case, the PCA acts as a radiation source. Alternatively, instead of an applied voltage, a free-space electromagnetic signal can be used to accelerate the optically induced carriers. The contact electrodes are utilized to measure the resulting voltage signal and the PCA acts as a detector for free-space electromagnetic radiation. With the help of PCAs, time-domain spectroscopy systems in the far-infrared spectral region have been established for various measurement purposes, ranging from material science to medical applications [2, 6, 18, 136].

PCAs show a very broadband behavior and allow for the generation and detection of signals in the THz frequency range. The bandwidth is mainly given by the rise time of the optically induced carrier density n_c. As demonstrated in [137–139], midinfrared photoconducting detection reaching up to 50 THz is possible. For a detailed analysis of the bandwidth of a PCA-based detection system, the temporal evolution of the induced carrier density is important. Since in GaAs the mobility of holes is much smaller than the electron mobility, in the following only the latter are taken into account. The optical carrier generation results in a rate equation,

$$\frac{\mathrm{d}}{\mathrm{d}t} n_\mathrm{c} = -\frac{n_\mathrm{c}}{\tau_t} + G(t). \tag{2.33}$$

Here, τ_t refers to the carrier trapping time, which is the dominant mechanism with regard to the lifetime of free carriers in LT-GaAs. Due to the

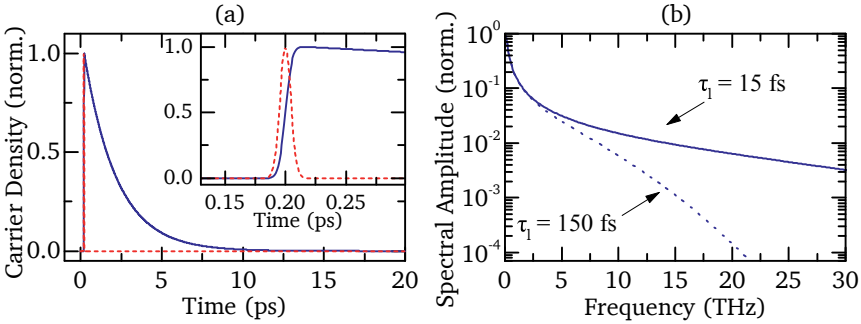

Figure 2.6 (a) Simulation of the carrier density $n_c(t)$ after excitation with a laser pulse centered at $t = 0.2$ ps. The FWHM of the excitation pulse is 15 fs, the carrier trapping time $\tau_t = 1.0$ ps. For comparison, the excitation pulse is displayed as well (dotted line). The inset shows a temporal magnification of the laser excitation. (b) Fourier transform of $n_c(t)$ for different values of the FWHM of the laser, τ_l.

low-temperature growth process and arsenic overpressure, midgap trap states are generated which lead to very fast trapping of carriers, reaching subpicosecond values [140]. The PCAs used in this work show a usual carrier trapping time of about 1 ps. In principle, long-lifetime photoconductors may be used for THz generation and detection as well [141–143]. But to inhibit the accumulation of charge carriers in the PCA and, thereby, decrease their noise contribution to the measurement process, a short lifetime of free carriers is beneficial for the detection process [144, 145]. In equation (2.33), $G(t)$ expresses the light-induced generation of charge carriers, which depends on the absorption rate $\alpha(\omega_0) \equiv \alpha_{\omega_0}$ at the laser center frequency ω_0 as given by equation (2.17) and the temporal evolution of the laser intensity $I(t) \propto |E(t)|^2$,

$$G(t) \propto \alpha_{\omega_0} |E(t)|^2 \propto \alpha_{\omega_0} e^{-\frac{t^2}{2\sigma^2}}. \tag{2.34}$$

For simplicity, the temporal profile of the field envelope is assumed to follow a Gaussian behavior with $\sigma = \tau_l/(2\sqrt{2\ln 2})$, τ_l being the FWHM of the pulse. With a laser system as described in section 2.2, values of $\tau_l \approx 15$ fs are reached. Solving equation (2.33) for $n_c(t)$, a temporal behavior as shown in figure 2.6 (a) results. The simulation parameters were set to $\tau_t = 1$ ps and $\tau_l = 15$ fs, the optical pulse is centered at $t = 0.2$ ps. As can be seen in the inset of figure 2.6 (a), the carrier density rises within the first 50 fs after the onset of the laser excitation. The subsequent carrier relaxation processes take place on a ps time scale. Due to the short rise time, the frequency spectrum of $n_c(t)$ stretches into the THz frequency

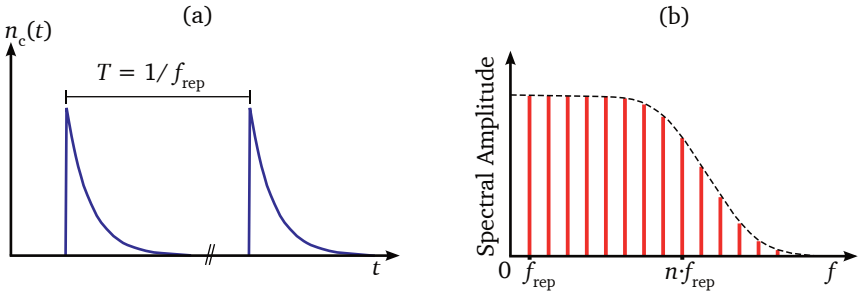

Figure 2.7 (a) Pulsed optical excitation of the semiconductor results in a pulsed carrier density n_c. (b) In frequency domain, the pulsed carrier distribution equals a comb structure. The modes of this THz frequency comb are exact multiples of f_{rep}.

range as shown in figure 2.6 (b). For comparison, also the simulation results for carrier excitation using laser pulses with a longer FWHM of 150 fs have been included. As can be seen, the high-frequency behavior of the carrier density is significantly influenced by the laser pulse FWHM. It should be emphasized that the simple model of equation (2.33) only yields an estimate of the frequency response of a PCA. More elaborated calculations considering additional material-related influences or the RC-time constant of the antenna structure may be found in the literature, as for example in [137, 139].

Due to the fast decay time of the carrier density, the excitation of a PCA using consecutive laser pulses as given by the laser system described in section 2.2 results in a pulsed temporal behavior of the carrier density as well. Thus the frequency response of n_c has to be described using a comb structure rather than a continuous spectrum, refer figure 2.7. According to the frequency response of the carrier density, this so called carrier frequency comb or THz frequency comb [53] covers a frequency range from DC to several THz. The THz comb may be regarded as an rectified optical frequency comb, as reflected by the intensity-dependence of n_c. Here, it is important to note that the carrier-envelope offset frequency f_{CEO} of the optical comb is eliminated by the rectification process. Hence, differing from equation (2.24) for the optical frequency comb, the THz frequency comb as created in a PCA consists of comb modes located at frequencies $f_{n,PCA}$ which are exact integer multiples n of the repetition rate f_{rep},

$$f_{n,PCA} = n f_{rep}. \tag{2.35}$$

Such a THz frequency comb may be utilized for the detection of free space cw signals with a frequency of f_{THz} in a straightforward manner [54].

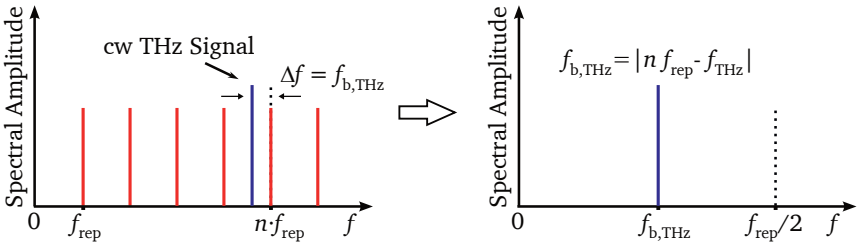

Figure 2.8 Measurement of a cw signal in the THz frequency range. A heterodyne mixing process between the THz signal and the nearest comb mode results in a beating signal with a frequency of $f_{b,THz}$ in the range between DC and $f_{rep}/2$.

The electromagnetic field $\mathbf{E}_{\mathrm{THz}}(t)$ of the cw signal affects the optically excited carriers and a current flow $\mathbf{J}(t)$ is induced,

$$\mathbf{J}(t) = e\, n_{\mathrm{c}}(t)\, \mu_{\mathrm{el}}\, \mathbf{E}_{\mathrm{THz}}(t). \tag{2.36}$$

Neglecting the contribution of holes, $\mathbf{J}$ depends on the elementary charge e and the electron mobility μ_{el}. For simplicity, dynamic effects of μ_{el} as well as resonance phenomena in the material are not taken into account here. A more thorough description is necessary in the case where a detailed investigation of the temporal behavior of the current pulse is of interest, confer [146]. However, for the following discussion only a specific feature of the pulsed nature of n_{c} and thus $\mathbf{J}$ is important. The frequency components of the detection signal are determined by a heterodyne mixing process between each line of the THz frequency comb and the cw THz signal. This process is schematically shown in figure 2.8. The lowest frequency component of the mixing processes is given by the beating frequency $f_{\mathrm{b,THz}}$ between the THz signal at f_{THz} and its nearest-neighbor comb line n,

$$f_{\mathrm{b,THz}} = |n\, f_{\mathrm{rep}} - f_{\mathrm{THz}}|. \tag{2.37}$$

Since the maximum distance of f_{THz} to the nearest comb line is half the repetition rate, the frequency $f_{\mathrm{b,THz}}$ is always located between DC and $f_{\mathrm{rep}}/2$. In this MHz-frequency range, standard electronics may be used for detection of the beating signal and the subsequent analysis processes. Higher frequency components of $\mathbf{J}$, resulting from the sum frequency of the mixing process or mixing with other comb lines either exceed the frequency range detectable with PCAs or are removed from the recorded signal via low-pass filtering. Using equation (2.37), f_{THz} can be deduced from the measurement of $f_{\mathrm{b,THz}}$ assuming n and f_{rep} are known. The laser repetition rate is easily measured, e.g., using a photo diode and a frequency

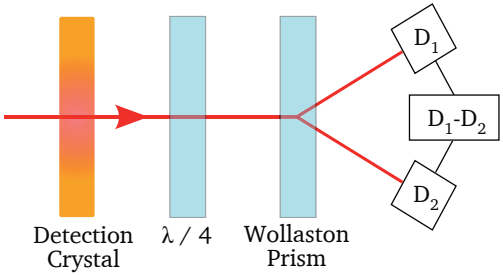

Figure 2.9 A balanced-detection setup is composed of the electro-optic detection crystal, where the phase of an optical probe beam is modified by the external field. A quarter-wave plate is used to convert the phase modulation into an amplitude modulation. The latter is measured by separating modulated and non-modulated parts of the probe light with, e.g., a wollaston prism and measuring their intensity difference using a balanced photoreceiver. A detailed description may be found in, e.g., [61].

counter. To determine n, a second measurement of the beating signal with a slightly detuned value of the repetition rate has to be performed. Assuming that the frequency f_{THz} of the cw signal is stable, n equals the ratio of the frequency shifts,

$$n = \frac{f_{\mathrm{b,THz}}^{(1)} - f_{\mathrm{b,THz}}^{(2)}}{f_{\mathrm{rep}}^{(1)} - f_{\mathrm{rep}}^{(2)}}, \tag{2.38}$$

where the superscripts denote the first and second measurement.

Second-Order Nonlinear Effects: Electro-Optic Detection

Next to the absorption-based detection technique, an alternative method related to higher-order terms of the susceptibility can be used to measure electromagnetic radiation in the THz frequency range. Since this technique is utilized for the detection of cw as well as for pulsed signals throughout this work, the following paragraphs describe the characteristics of both methods.

Pulsed THz radiation The modulation of an optical probe beam in an electro-optic crystal via the Pockels effect has been widely studied in the last decades. Subjecting the crystal to an electrical field introduces optical birefringence in the material. This changes the phase of the transmitting probe beam proportional to the field strength. In an ellipsometric detection scheme, the corresponding change of polarization can easily be evaluated, refer figure 2.9. First applications allowing for the measurement of fast repetitive electrical signals have been reported in the

1980s [147, 148]. The presented sampling technique is based on a variation of the temporal delay between the signal to be measured and the probe pulse. At each sampling position, the optical pulse train is exposed to a specific signal-induced birefringence of the detection crystal. By changing the relative temporal positions, different sections of the signal's waveform determine the phase change of the probe beam and a time-representation of the signal under study can be acquired.

Efforts to exploit this technique intensified when the detection of free-space electrical signals in the terahertz frequency range was achieved [149]. Since the focus of interest was given by the measurement of pulsed THz signals, a broadband detection scheme was necessary to cover high-frequency components of the pulses. Up to that time, materials like $LiTaO_3$ had been used, but the range of suitable materials quickly expanded. ZnTe and GaP showed to be promising candidates for broadband detection purposes [150, 151]. Studies of the response function of such detection systems followed, highlighting the importance of the detailed knowledge of the materials susceptibility for an exact modeling of the measurement process [152]. Subsequent work focused on a deeper understanding of the frequency-behavior of the light-matter interaction [152–154] and propagation effects on the measured waveform [155]. The geometric dependencies for optimal detection efficiency with respect to the crystallographic structure of the materials have been worked out in [156, 157].

To express the strength and orientation dependency of the light-matter coupling in terms of the material properties, a formal concept based on tensor notations has been developed. In this picture, the non-isotropic refraction effects of a crystal are described using the index-ellipsoid notation. The material properties are summarized in an electro-optic tensor r, whose elements follow the symmetry conditions given by the crystallographic class of the material. As derived in standard literature [60, 61], the electro-optic properties of materials of the $\bar{4}3m$-symmetry group (zinc-blende structure), i.e. ZnTe, GaAs or GaP, can be described using only one coefficient of r, namely r_{41}. For the materials relevant in this work, literature gives $r_{41}^{\mathrm{ZnTe}} = 3.9\ \mathrm{pm/V}, r_{41}^{\mathrm{GaAs}} = 1.1\ \mathrm{pm/V}, r_{41}^{\mathrm{GaP}} = 1.0\ \mathrm{pm/V}$ [60]. Also most of the previously cited publications are based on this notation, this is of course equivalent to a description using the material's susceptibility as given in section 2.1. There, a general expression for the second-order nonlinear susceptibility in the nonresonant limit has been introduced (equation (2.23)). As shown in [73], the dielectric permittivity connects both r and $\chi^{(2)}$ in a simple manner,

$$\chi^{(2)}_{abc}(\omega) = \frac{-\epsilon^2(\omega)}{2} r_{abc}(\omega) = \frac{-n^4(\omega)}{2} r_{abc}(\omega). \tag{2.39}$$

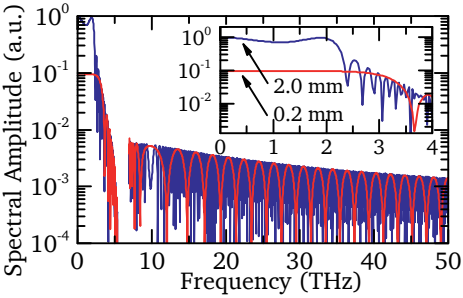

Figure 2.10 Transfer function of the electro-optic detection process, taking into account the group velocity mismatch between the THz signal and the optical pulse with a carrier wavelength of 800 nm. Depending on the interaction length (e.g. the crystal width), the strength of the amplitude modulation periodically varies. The inset is a magnification of the first 4 THz of the transfer function.

Considering the efficiency of the THz detection in electro-optic materials like ZnTe, the strong orientation dependency with regard to the crystal axis and the polarization of the probe beam and THz field has to be taken into account. Following the description of [156] and [157], the maximum detection signal I_{det} obtained for a well-aligned balanced-detection setup similar to the one shown in figure 2.9 is

$$I_{\text{det}} = I_0 \omega n^3 E_{\text{THz}} r_{41} L / c. \tag{2.40}$$

Here, I_0 denotes the intensity of the probe pulse with frequency ω, E_{THz} is the amplitude of the applied THz field and L is the interaction length of the probe beam inside the detection crystal. This expression represents an approximation, valid for a small field-induced change of the probe beam's phase and low THz frequencies (below $\approx$ 3 THz). At large crystal widths L or high frequencies, the different dispersion behavior of the THz and optical beam inside the detection crystal results in an accumulating phase mismatch of both signals. To account for this, a more complex dependency of I_{det} on L has to be considered [19,151]. Due to the phase mismatch, the amplitude of the detection signal periodically varies with the crystal length respectively the wavelength of the electromagnetic signals involved. In figure 2.10, the electro-optic transfer function of the detection process in ZnTe is shown for two different crystal thicknesses (0.2 mm and 2.0 mm) and a fixed wavelength of the probe beam (800 nm). At low frequencies of the THz signal, the scaling of the detection signal is proportional to L as expressed by equation (2.40). At high frequencies, both crystal thicknesses yield a comparable maximum amplitude of the transfer function, however the oscillation period significantly differs. From 5 THz to 6 THz, phonon resonances limit the detection sensitivity of ZnTe crystals.

Continuous-wave THz detection Within the preceding paragraphs it has been introduced how to employ the second-order nonlinear terms of the susceptibility for the detection of pulsed THz radiation. This technique will be used in chapter 4 to measure the THz emission of optically induced currents in GaAs. However, concerning the measurement scheme which will be presented in chapter 3, the detection of cw-THz radiation has to be analyzed with regard to frequency, phase and amplitude. For this purpose, a different point of view regarding the detection process is necessary, described in the following. More details are given, since the resulting dependencies are different as compared to the standard equation for the well established pulsed-THz detection.

Similar to the measurement of pulsed signals, cw-THz fields may be used to modify the phase of a probe beam in an electro-optic crystal like ZnTe or GaP via the Pockels effect. Yet, for a cw-signal, a sampling method as described before is not suitable to obtain the desired parameters of the electrical field. Instead, the field is regarded as a perturbation source, acting on the propagation of a probe beam inside the crystal [60]. Formulating the wave equation in media using the displacement field $\mathbf{D} = \epsilon_0\mathbf{E} + \mathbf{P}$, it follows with the power series (2.9) and $\epsilon^{(1)} = \epsilon_0(1 + \chi^{(1)})$

$$\nabla^2\mathbf{E}(t) - \mu\frac{\partial^2}{\partial t^2}\epsilon^{(1)}\mathbf{E}(t) - \mu\epsilon_0\frac{\partial^2}{\partial t^2}\chi^{(2)}\mathbf{E}^2(t) = 0. \tag{2.41}$$

Considering the superposition of an optical light field and a co-propagating cw-THz signal, $\mathbf{E}(t) = \mathbf{E}_{\text{sum}}(t) = \mathbf{E}_{\text{opt}}(t) + \mathbf{E}_{\text{THz}}(t)$ with frequencies ω_{opt} and ω_{THz}, the last term on the left side of equation (2.41) contains mixed terms of both electrical waves. Focusing on the latter, an approximation using $\omega_{\text{opt}} \gg \omega_{\text{THz}}$ results in a solution of the wave equation following

$$\mathbf{E}_{\text{sum}}(t) \propto \mathbf{E}_{\text{sum}} e^{i[\omega_{\text{opt}}t + \delta(\omega_{\text{opt}})\sin(\omega_{\text{THz}}t)]}, \tag{2.42}$$

which expresses the temporal evolution of the optical wave exiting the crystal. Here, $\mathbf{E}_{\text{sum}}$ is the amplitude of the wave. This equation denotes a phase-modulated wave with a modulation index $\delta(\omega)$, accounting for the coupling of the two waves in dependency on the crystal parameters,

$$\begin{aligned}\delta(\omega) &= -\frac{\omega}{c\, n_{\text{ref}}}\,\chi^{(2)}(\omega)\,\eta\,E_{\text{THz}} \\ &= \frac{\omega\, n_{\text{ref}}^3}{2c}\,r_{41}(\omega)\,\eta\,E_{\text{THz}}.\end{aligned} \tag{2.43}$$

Thereby n_{ref} is the unperturbed refractive index of the crystal, η expresses a scaling factor, reflecting the influence of the phase velocity mismatch of

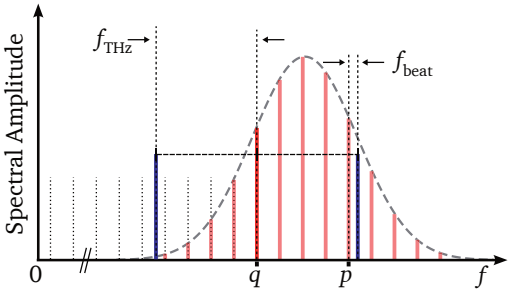

Figure 2.11 Frequency representation of the phase modulation caused by the electro-optic effect. Each comb mode develops sidebands at a distance of f_{THz}, these sidebands have a distance of f_{beat} to their next-neighbor comb modes. For simplicity, the sidebands of only one comb mode q are shown.

the THz signal and the probe beam over the length of the crystal and E_{THz} denotes the amplitude of the THz signal. The phase modulation results in the generation of sidebands of the carrier frequency ω_{opt}, which is easily shown using the first two terms of a Taylor expansion of equation (2.42),

$$\begin{aligned}\mathbf{E}_{\mathrm{sum}}(t) &\approx \mathbf{E}_{\mathrm{sum}}\, \mathrm{e}^{i\omega_{\mathrm{opt}}t}\,(1 + i\,\delta(\omega_{\mathrm{opt}})\,\sin(\omega_{\mathrm{THz}}t)) \\ &= \mathbf{E}_{\mathrm{sum}}\left(\mathrm{e}^{i\omega_{\mathrm{opt}}t} + \frac{\delta(\omega_{\mathrm{opt}})}{2}\,\mathrm{e}^{i(\omega_{\mathrm{opt}}+\omega_{\mathrm{THz}})t} - \frac{\delta(\omega_{\mathrm{opt}})}{2}\,\mathrm{e}^{i(\omega_{\mathrm{opt}}-\omega_{\mathrm{THz}})t}\right).\end{aligned} \tag{2.44}$$

In the right part of equation (2.44), the first pair of sidebands at frequencies $(\omega_{\mathrm{opt}} \pm \omega_{\mathrm{THz}})$ occurs. Using higher terms of the Taylor expansion, an infinite series of sidebands will be obtained.

The hitherto achieved expressions have been derived for a light field oscillating at one single frequency. Without much effort, this point of view is expanded to an optical frequency comb passing through the detection crystal. Expression (2.44) is valid for all comb modes. For this ω_{opt} has to be replaced by the individual comb mode frequency as given in equation (2.24) and the value of δ changes correspondingly. The resulting frequency expression resembles two additional comb structures, shifted by $\pm\omega_{\mathrm{THz}}$ and scaled according to the values of δ. This is schematically shown in figure 2.11, where for sake of simplicity only the sidebands of one particular comb mode q are shown. Due to this constant frequency shift, all sidebands have the same distance of f_{beat} to their next-neighbor comb mode. The importance of this issue is revealed in the following.

Similar to the setup used for the measurement of pulsed THz signals, a balanced detection setup as shown in figure 2.9 is employed for the measurement of the phase modulation. After passing the detection crystal, a quarter-wave plate is utilized to transfer the phase modulation into an amplitude modulation. This can be expressed by a matrix notation following the Jones Calculus [158]. Choosing the coordinate system and

the relative phase of the optical beam such that the beam is represented by a two-component vector with one unperturbed component and one phase-modulated component, the optical comb structure is expressed by a summation over all comb modes p as follows

$$\mathbf{E}(t) = \begin{pmatrix} \sum\limits_p E_p \, \mathrm{e}^{i\omega_p t} \\ \sum\limits_p E_p \, \mathrm{e}^{i\omega_p t} \left(1 + \frac{\delta(\omega_p)}{2} \mathrm{e}^{i\omega_{\mathrm{THz}} t} - \frac{\delta(\omega_p)}{2} \mathrm{e}^{-i\omega_{\mathrm{THz}} t}\right) \end{pmatrix}. \tag{2.45}$$

The effect of a $\lambda/4$-plate, with its optical axis having an angle of $\pi/4$ to the aforementioned directions, is described by the matrix

$$W = \frac{1}{\sqrt{2}} \begin{pmatrix} 1 & -i \\ -i & 1 \end{pmatrix}. \tag{2.46}$$

After multiplication of formulas (2.46) and (2.45) the electrical field after the $\lambda/4$-plate, $\mathbf{E}'(t)$, is obtained

$$\begin{aligned} \mathbf{E}'(t) &= W \cdot \mathbf{E}(t) \\ &= \frac{1}{\sqrt{2}} \begin{pmatrix} \sum\limits_p E_p \, \mathrm{e}^{i\omega_p t} \left(1 - i - i \, \frac{\delta(\omega_p)}{2} \mathrm{e}^{i\omega_{\mathrm{THz}} t} + i \, \frac{\delta(\omega_p)}{2} \mathrm{e}^{-i\omega_{\mathrm{THz}} t}\right) \\ \sum\limits_p E_p \, \mathrm{e}^{i\omega_p t} \left(-i + 1 + \frac{\delta(\omega_p)}{2} \mathrm{e}^{i\omega_{\mathrm{THz}} t} - \frac{\delta(\omega_p)}{2} \mathrm{e}^{-i\omega_{\mathrm{THz}} t}\right) \end{pmatrix} \\ &=: \begin{pmatrix} E_1'(t) \\ E_2'(t) \end{pmatrix}. \end{aligned} \tag{2.47}$$

Using a Wollaston prism, the polarization components E_1' and E_2' are separated and focused onto the two photodiodes of a differential detector. Subtracting both photodiode signals, it follows for the output signal D,

$$\begin{aligned} D &= |E_1'(t)|^2 - |E_2'(t)|^2 \\ &= \sum_{p,q} E_p \, E_q \, (\delta(\omega_p) - \delta(\omega_q)) \left[\mathrm{e}^{i(\omega_p - \omega_q + \omega_{\mathrm{THz}})t} - \mathrm{e}^{i(\omega_p - \omega_q - \omega_{\mathrm{THz}})t}\right]. \end{aligned} \tag{2.48}$$

This expression represents the mixing of each comb mode p with the sidebands of all other modes q of the comb by the summation over the indices p and q. With equation (2.24), the frequencies $\omega_i = 2\,\pi f_i$ can be rewritten using

$$\omega_p - \omega_q = 2\pi \, (n_p - n_q) \, f_{\mathrm{rep}} = 2\pi \, n_{pq} f_{\mathrm{rep}}, \tag{2.49}$$

with n_{pq} being the number of comb modes between mode p and q. Inserting 2.49 into 2.48 and grouping all terms with the same value of $n_{pq} \equiv n$, a rectified, offset-free frequency comb as described by equation (2.35) is obtained, which is composed of individual comb modes $f_{n,\mathrm{EOS}}$ being integer multiples of the repetition rate,

$$f_{n,\mathrm{EOS}} = n f_{\mathrm{rep}}. \tag{2.50}$$

Thus, analog to equation (2.37) for the use of PCAs, expression (2.48) describes a mixing process between the n^{th} comb mode of the rectified comb and the THz signal. Again, the lowest frequency component of the mixing product is given by those values of n, where $|n f_{\mathrm{rep}} - f_{\mathrm{THz}}|$ is minimal. This is equal to the mixing of each sideband with its next-neighbor comb mode of the rectified optical comb. Consequently, as already introduced in the case of PCA-based detection, the THz frequency can be deduced if f_{rep} and n are known. Analyzing equation (2.48) further, three additional remarks have to be made.

First, it becomes obvious that the frequency range of the mixing process is limited by the spectral width of the optical beam. If the bandwidth of the pulses is smaller than the THz frequency to be measured, the frequency-shifted sideband-combs do not provide a sufficient overlap with the optical comb. Consequently, either the next-neighbor comb modes or the sidebands involved in a mixing process have low spectral power and minimize the mixing result. On the other hand, if the bandwidth of the pulses is larger than the frequency to be measured, mixing partners with high spectral power are obtained. Thus, to have a sufficient amount of non-zero terms for a fixed n in the sum of (2.48), a large spectral width of the laser pulses is necessary.

Second, next to the properties of the optical beam, also the spectral behavior of the detection crystal plays a role. Via equation (2.43), the frequency dependency of the second-order susceptibility $\chi^{(2)}$, expressed by the tensor element r_{41}, influences the amplitude of the sidebands in (2.42). Due to this, material properties like phonon resonances result in a reduced detection ability in certain frequency ranges. For ZnTe, mainly frequencies around 5.1 THz are affected [153]. Nevertheless this limitation may be avoided by the choice of a different detection material in the corresponding frequency regions, i.e. GaP [152]. In appendix A, table A.1 lists the frequencies of the lowest optical phonon resonances for several materials suitable for the electro-optic detection process.

Third, the importance of bandwidth-limited pulses is revealed in expression (2.48). Only for pulses with a minimum value of the time-band-

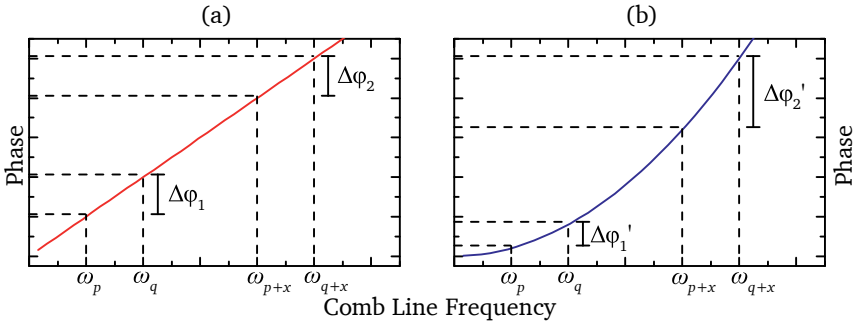

Figure 2.12 (a) For a bandwidth-limited pulse, different pairs of comb modes p and q with a fixed distance to each other show an equal relative phase difference $\Delta\varphi_1 = \Delta\varphi_2$. (b) If the pulse is chirped (e.g. linear chirp), the relative phase difference changes and $\Delta\varphi_1' \neq \Delta\varphi_2'$.

width product, a stringent coherence of all spectral components is realized. If the pulses deviate from this optimum value by showing a chirped behavior, different pairs of comb modes p and q, which have the same distance n to each other, will have a different phase relation (see figure 2.12). By this, in equation (2.48), terms with a common value for n will add destructively, reducing the obtained mixing signal.

To conclude this section, the most important findings of the preceding paragraphs are summarized. It has been introduced how to utilize the semiconductor susceptibility for THz generation and detection purposes. In both cases, a clear distinction between absorption-based and second-order nonlinear effects is given. Concerning the generation of THz radiation, the excitation of drift- and diffusion-based currents as well as coherently controllable shift currents has been described. The electromagnetic radiation emitted by these currents is utilized in chapter 4 to demonstrate an all-optical, steerable THz source. Also the for THz detection purposes, two different methods have been introduced. The photoconductive detection method based on the creation of charge carriers as well as the nonlinear electro-optic detection technique may be employed for the full characterization of cw-THz emitters. This is shown in chapter 3.

3 Terahertz Frequency Combs

3.1 Motivation and Review of Previous Work

Time and, thus, frequency plays a major role in today's society. This affects many different aspects of the daily life, but is especially important for modern electronic equipment. Regarding specific fields like, e.g., communication technology, the technical evolution from first radio-frequency devices in the early 20^{th} century up to today's optical data transmission techniques or global-positioning applications spans several orders of magnitude in carrier frequency and bandwidth. Similarly, major scientific progress is tightly bound to a more and more accurate measurement of time and frequency. This is why over decades increasing effort has been spent to establish a frequency standard with highest precision and accuracy [159]. Utilizing devices like atomic fountain clocks [160], it is possible to measure frequencies with an uncertainty of 10^{-16} [161]. The remarkable high accuracy of these atomic clocks is nowadays used to define the second within the SI. But already new generations of all-optical clocks are about to be established, achieving even higher frequency uncertainties of 10^{-18} [162–164].

To utilize such a frequency standard in a metrological sense, the optical frequency comb [88] has shown to be a perfect tool to connect the microwave-resonance of atomic clocks to optical frequencies [165, 166]. With this development, a revolution in frequency metrology started [89–91].

As introduced in chapter 1, the need of a corresponding measurement technique also exists in the THz frequency range. Due to the spectral properties of optical lasers, the aforementioned technique of the optical frequency comb may not be directly applied here. However, as derived in subsection 2.3.2, the optical comb can be converted to a THz frequency comb and utilized for measurement purposes with high accuracy [53–55, 58, 167]. The detection bandwidth of this technique reaches from DC to several 10 THz, as measurements of CO_2 laser lines at 30 THz show [168].

This chapter is organized as follows. In section 3.2 a detection scheme is introduced, capable of measuring the frequency of cw-THz radiation

with a hitherto unreached accuracy. A comparison of EO- and PC-based measurement techniques is given, with regard to the measurement accuracy as well as the detection sensitivity. Section 3.3 expands the concept of THz frequency combs to allow for spatially resolved measurements of phase and amplitude of a THz emitter. By this, the radiation pattern of THz sources may be characterized. The comparison between EO and PC detection gives insight about the invasiveness of both techniques. The frequency range of the detection schemes are analyzed in section 3.4 by employing a 30 THz source for the measurement process. Section 3.5 summarizes the obtained results, which have partly been published in references [A1, A3].

3.2 High-precision Frequency Measurements

In the following, a high-precision measurement scheme for the frequency determination of a free-space cw-signal in the THz frequency range is demonstrated. A prerequisite for precise and accurate frequency measurements is the suppression of the influence of the laser noise on the measurement process. This is realized using the so called transfer concept, which is introduced at first. After giving a detailed description of the experimental setup, the data analysis procedure is described, necessary for the correction of the measurement signal utilizing the transfer concept. After this preliminary work, the measurement results are presented and analyzed. This finally allows for a comparison of EO and PC detection techniques.

3.2.1 Transfer Concept

By utilizing an optical frequency comb for the generation of a THz frequency comb following the description given in subsection 2.3.2, noise properties of the optical comb directly transfer to the THz comb. This is true indifferent whether an EO- or PC-based detection scheme is chosen, as becomes obvious according to equations (2.35) and (2.50) where the repetition rate f_{rep} of the laser is included. Hence the mixing signal between the THz field with a frequency of f_{THz} and one comb line of the THz frequency comb, see expression (2.37), directly depends on the repetition rate of the optical oscillator. Since f_{rep} is not known exactly, the repetition rate fluctuations of a free running Ti:Sa laser as introduced in section 2.2 do not allow for high-precision measurements using THz combs without applying additional effort. Moreover, precision frequency measurements have to be analyzed with regard to a superior frequency standard, which has to be incorporated in the measurement setup. These issues may be accounted for by different approaches.

One possible approach uses an external stabilization of the laser cavity length in order to obtain a noise-reduced optical frequency comb, see section 2.2. Within this approach, an electronic control unit compares the optical repetition rate with an external reference signal and adjusts the laser cavity accordingly. Hence, by using a reference signal connected to a frequency standard, a measurement setup ready for high-precision measurements is obtained. However for this approach, external controls such as feedback loops and piezo transducers are necessary. This leads to a complex and costly setup, with an accuracy being limited by the performance of the electronic equipment.

A second approach reduces the complexity of the involved electronics by avoiding an active stabilization of the laser cavity. Using the so called transfer concept which has been introduced in the optical region [165], the repetition rate fluctuations are recorded and the measurement signal can be corrected for the latter. The optical comb acts as a transfer oscillator only, transferring the stability of a local oscillator into the measurement process of f_{THz}. With such an approach, possible limitations with regard to the measurement accuracy due to the properties of the mechanical stabilization of the laser cavity are avoided. Moreover, using the transfer concept a measurement scheme independent from a specific laser system endowed with a stabilization mechanism is obtained, thus a more flexible and less costly solution for high-precision frequency measurements is provided.

To realize the transfer concept, a second measurement process following equation (2.37) is set up. But instead of using a THz signal for the mixing process with the nearest (m^{th}) comb line, a local oscillator (LO) signal with a known and very precise frequency f_{LO} is used,

$$f_{\mathrm{b,LO}} = |m\, f_{\mathrm{rep}} - f_{\mathrm{LO}}|. \tag{3.1}$$

Since the LO frequency usually lies in the GHz range, this mixing process may be performed by electronic means, e.g., by use of a photodiode to rectify the optical comb and using a standard electronic mixer to mix the photodiode signal with the output signal of the LO. The mixing product at a frequency of $f_{\mathrm{b,LO}}$ is a precise measurement of the repetition rate, containing all fluctuations of f_{rep} during the measurement period. When now simultaneously $f_{\mathrm{b,THz}}$ and $f_{\mathrm{b,LO}}$ are measured, both signals can be combined in a third mixing step as shown in figure 3.1. For this, the frequency $f_{\mathrm{b,LO}}$ is shifted by a factor of n/m. This results in a difference frequency f_{cor} being independent of f_{rep},

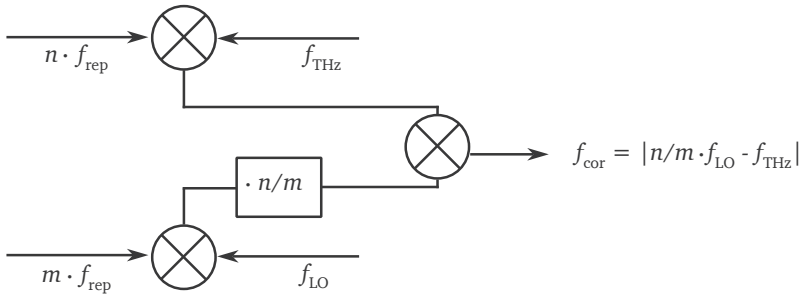

Figure 3.1 Scheme of the transfer concept. The THz signal and a local oscillator (LO) are mixed with different modes of the frequency comb. By changing the frequency of the LO mixing signal, a third mixing process results in a signal being independent of the fluctuations of the repetition rate f_{rep}.

$$f_{\mathrm{b,THz}} \otimes \frac{n}{m} f_{\mathrm{b,LO}} = \left| n\, f_{\mathrm{rep}} - f_{\mathrm{THz}} - \left(\frac{n}{m}\, m\, f_{\mathrm{rep}} - \frac{n}{m}\, f_{\mathrm{LO}} \right) \right| = \left| \frac{n}{m} f_{\mathrm{LO}} - f_{\mathrm{THz}} \right| = f_{\mathrm{cor}}. \tag{3.2}$$

Equation 3.2 shows that the accuracy and precision of the local oscillator can be used for the measurement of f_{THz} without the need for a repetition rate stabilization of the optical comb.

3.2.2 Experimental Setup

To realize a high-precision frequency measurement scheme utilizing either PC- or EO-based detection techniques, the setup shown in figure 3.2 is used. Based on the emission of a pulsed laser as described in section 2.2 (repetition rate $f_{\mathrm{rep}} \approx 76$ MHz, pulse length 100 fs, center wavelength 810 nm, spectral width 20 nm), an optical frequency comb with an average power of 10 mW is focused on the PCA or the electro-optic detection crystal. The PCA as shown in figure 3.3 is made of low-temperature-grown GaAs, providing carrier trapping times of about 1 ps. On top of the substrate, golden contact pads have been evaporated in a bow-tie-shaped form with an excitation gap of $6 \times 6\ \mu\mathrm{m}^2$. A comparison of signal-to-noise ratios obtained for different antenna geometries is given in appendix B. While the probe beam reaches the gap from the front, the free-space electromagnetic radiation of the THz source is guided to the backside of the PCA. Using a hemispherical silicon lens, the THz radiation is coupled into the PCA and accelerates the optically excited carriers, as expressed by equa-

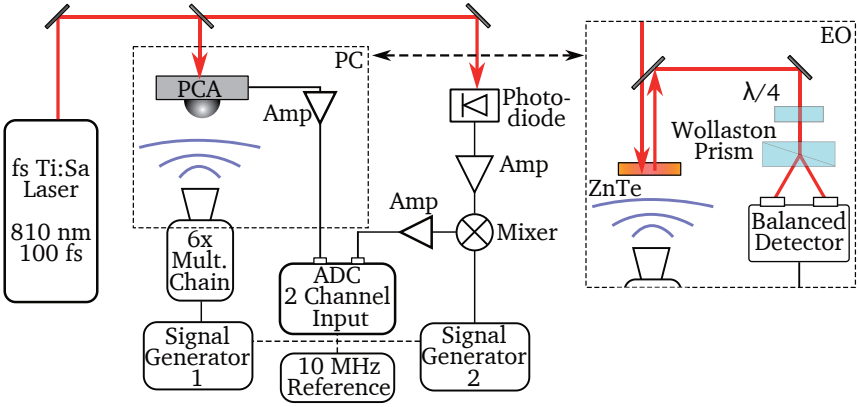

Figure 3.2 Schematic diagram of the high-precision frequency measurement setup (ADC = analog to digital converter, Amp = amplifier, PCA = photoconductive antenna). Either a measurement scheme based on PC or EO detection is used, depicted by the components inside the dashed boxes.

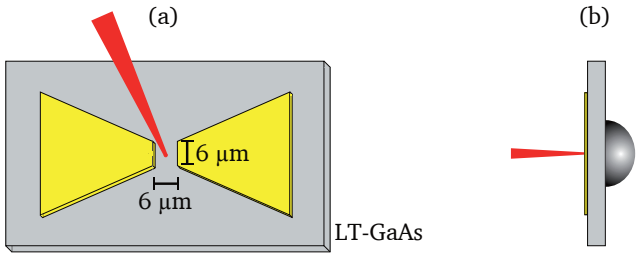

Figure 3.3 (a) The optical beam is focused onto a photoconductive antenna which is made of a low-temperature grown GaAs substrate and golden contact pads. (b) Side view of the PCA. A hemispherical Si-lens is attached to the backside, minimizing reflection effects of the incident THz radiation.

tion (2.36). Via the contact pads of the PCA, the current flow is measured as a voltage signal which is amplified (10^5 V/A transimpedance gain, 40 MHz bandwidth) and detected using an analog-to-digital converter (ADC, National Instruments NI-5122, 14 bit resolution, 10 MHz sampling rate). The device offers a two-channel signal input, providing the simultaneous acquisition of multiple signals.

In the case of EO-based detection, different materials have been tested for their usability as detection material. Details can be found in the appendix A. Here, a 3 mm ZnTe crystal is used. The incident optical beam passes through the crystal and gets reflected at the backside. Before the

Figure 3.4 Frequency-multiplier chain (Radiometer Physics, FE-110, multiplication factor 6, output power ≈ 10 dBm) with a W-band horn antenna (75-110 GHz).

reflection, only a minor phase-modulation of the optical beam takes place due to the large phase velocity mismatch of the forward-propagating beam and the THz field. After the reflection, the optical beam co-propagates with the THz radiation, resulting in the THz mixing phenomena as described in section 2.3.2. The phase modulation of the beam is analyzed using an EO-based detection scheme as described in figure 2.9 and the obtained signal from the balanced detector is measured with the ADC.

To analyze the accuracy of the measurement system, a precisely known THz signal is used. For this, an active frequency-multiplier chain (Radiometer Physics FE-110, multiplication factor 6, output power ≈ 10 dBm) set to an output frequency of $f_{\mathrm{THz}} = 100.02\,\mathrm{GHz}$ is connected to a signal generator (signal generator 1 in figure 3.2, Rhode and Schwarz SMF 100A). A detailed description of the emission properties of the antenna connected to the frequency-multiplier chain is given in section 3.3.

Additionally to the measurement of the THz beating signal, the temporal fluctuations of the repetition rate of the laser are measured. For this a second mixing process is set up. Here, a fast photodiode (Hamamatsu S5973, photoconductive mode) rectifies the optical comb. In figure 3.5, the circuit diagram and the spectral response of the diode, measured with an Agilent E4440 spectrum analyzer, is shown. As can be seen, a spectral coverage up to 4 GHz is obtained. Hence, the repetition rate of the laser can be measured at a higher harmonic, which provides increased sensitivity to laser timing jitter and reduced sensitivity to amplitude-to-noise conversion [95,105]. The choice of the appropriate high harmonic for this approach is a trade-off between the improved noise characteristics and the decreasing signal from the photodiode. Following equation (3.1), the m^{th} mode of the photodiode spectrum is mixed with an LO signal (signal generator 2 in figure 3.2, Anritsu MG3692C), set to the frequency f_{LO}. In the following, mixing processes utilizing the $m = 46^{\mathrm{th}}$ harmonic are analyzed. The influence of the use of other harmonics on the high-precision

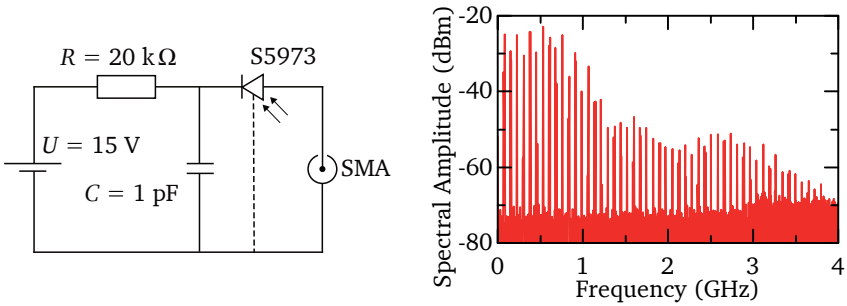

Figure 3.5 Circuit diagram and spectral response of the Hamamatsu S5973 photodiode illuminated by the Ti:Sa laser. For the transfer concept, a mixing process utilizing the 46$^{\text{th}}$ comb mode (3.496 GHz) is utilized.

measurement scheme is demonstrated in subsection 3.2.4. To suppress higher-order mixing modes and noise contributions, the mixing product is filtered using a 15 MHz-lowpass filter and a DC-block. After amplification, the signal is recorded using the second channel of the ADC. By this, both signals are acquired simultaneously, which is required for the application of the transfer concept.

Before the measurement results are presented, a specific feature of the detection setup has to be discussed. To provide a common time base for all devices of the measurement setup (i.e., both signal generators and the ADC), a 10 MHz quartz oscillator is used as a reference signal. Synchronizing source and detector to this signal, fluctuations of the reference frequency will cancel out. Using such a closed system, information about the accuracy of the setup are obtained. If an unknown THz source is to be analyzed, the setup has to be referenced to an external frequency standard. In such a case the measurement accuracy is limited either by the accuracy of the setup or the reference frequency. As reference signal, any standard available may be used: atomic clocks with a frequency accuracy of $2 \cdot 10^{-15}$ over 10 s [169], or a Global Positioning System (GPS)-disciplined oscillator providing frequency stability on the order of 10^{-9} to 10^{-11} over 10 s [170,171]. Due to the worldwide availability of the GPS signal, such a reference system also allows the realization of a portable setup, providing a non-laboratory-bound measurement device.

3.2.3 Data Analysis

To realize the transfer concept as described above, different implementations are possible. When the concept was first introduced [165], is was

based on a hardware approach, performing the involved frequency shifts and mixing processes via standard electronic components. In this work, a different strategy is applied. To avoid restrictions due to hardware limitations, e.g., resulting from limited frequency windows of the involved frequency shifters and -multipliers, a software-based solution has been developed. By this, the measurement scheme may be easily adopted for the analysis of cw-THz signals operating over a broad spectral range, as well as for laser systems providing different repetition rate frequencies. No additional devices (e.g. spectrum analyzer, frequency counters, phase-lock loops) have to be used. This considerably simplifies the experimental setup. The beating signals according to equations (2.37) and (3.1) are recorded using the two-channel ADC and a subsequent data processing algorithm is implemented to realize the correction process as given by expression (3.2).

The transfer concept is based on a multiplication of the frequency $f_{\mathrm{b,LO}}$ of the measured beating signal by a factor determined by the comb mode numbers, n/m. To realize this, the real-valued waveform $s(t)$ is converted to a complex representation using the Hilbert-transform H [172,173]. The Hilbert transform results in a 90° phase shifted signal (signal in quadrature), as shown in figure 3.6. Adding both signals, a complex time-domain signal is obtained,

$$\begin{aligned} z(t) &= s(t) + i\,H[s(t)] \\ &= a(t)\,e^{i\phi(t)}, \end{aligned} \tag{3.3}$$

composed of an amplitude $a(t) = abs[z(t)]$ and a phase $\phi(t) = arg[z(t)]$. Now the frequency multiplication is computed in a straightforward way by a simple multiplication of the phase values by the factor n/m,

$$z'(t) = a(t)\,e^{i\frac{n}{m}\phi(t)}. \tag{3.4}$$

To finalize the correction process, the real part of the resulting time trace is multiplied by the time trace of the THz beating signal $f_{\mathrm{b,\,THz}}$. This is equivalent to the mixing process as given in equation (3.2). As a result, the difference frequency f_{cor} is obtained, representing the corrected THz beating signal. Additionally to these steps of data analysis, the measured signals as well as the signal obtained after the mixing process have been frequency-filtered with a Gaussian filter centered at the beating frequencies (width $\approx$ 10 kHz for $f_{\mathrm{b,\,rep}}$ and $\approx$ 20 kHz for $f_{\mathrm{b,\,THz}}$) to suppress higher-order mixing products as well as other noise signals inherent to the experimental setup. No additional fitting, interpolation or other data processing methods have been used in the realization of the transfer concept.

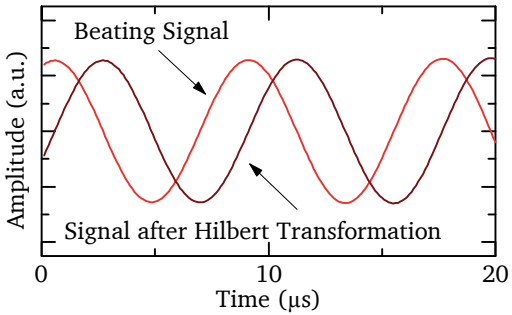

Figure 3.6 Schematic representation of the beating signal and its Hilbert-transform.

Next to this correction process, the complex representation of a measurement signal according to equation (3.3) may be utilized to evaluate the instantaneous frequency of the signal [174, 175]. This allows for an analysis of the noise behavior of the signal. The concept of the instantaneous frequency is easily understood with regard to a harmonic signal as represented by $s(t) = A\cos(2\pi\, f\, t + \theta)$ with an amplitude A, oscillation frequency f and a constant phase value θ. Expressing the argument of the cosine function, $(2\pi\, f\, t + \theta)$, as the time varying phase $\phi(t)$ using expression (3.3), the instantaneous frequency of the signal is obtained from

$$f_{\mathrm{i}}(t) = \frac{1}{2\pi}\frac{\mathrm{d}\phi(\mathrm{t})}{\mathrm{d}t} = \frac{1}{2\pi}\frac{\mathrm{d}\, arg[z(t)]}{\mathrm{d}t}. \tag{3.5}$$

3.2.4 Measurement Results

Before the detection of free-space cw-THz radiation is demonstrated, the noise properties of the optical resonator are analyzed with respect to the fluctuation of the repetition rate. According to equation (3.1), the latter may be extracted from the beating signal between the local oscillator and one comb mode of the rectified optical comb. Corresponding signals are shown in figure 3.7 (a) and (c), revealing the normalized spectral power obtained for 10-s long time-domain measurement intervals. For (a) the output signal of the local oscillator was set to a frequency of $f_{\mathrm{LO}} = 3.4961$ GHz and the repetition rate of the comb was $f_{\mathrm{rep}} \approx 76.00$ MHz, for (b) the values have been $f_{\mathrm{LO}} = 3.495$ GHz and $f_{\mathrm{rep}} \approx 75.98$ MHz. Hence the $f_{\mathrm{LO}}/f_{\mathrm{rep}} \approx 46^{\mathrm{th}}$ mode of the optical comb has been used for the mixing processes. The two measurements reveal significant differences in the resulting 3 dB width, being approximately 40 Hz in (a) and nearly 400 Hz in (b). This variance is attributed to a different behavior of the optical comb during both measurement periods. To analyze this in detail, the concept of instantaneous frequency

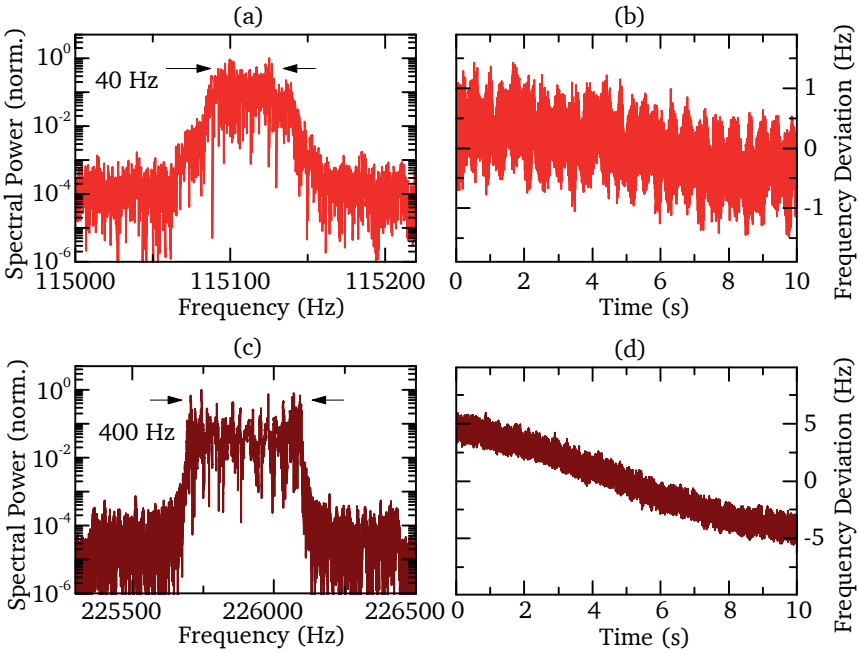

Figure 3.7 (a),(c) Power spectra of the beating signals between the 46^{th} harmonic of the repetition rate and a local oscillator at 3.4961 GHz and 3.495 GHz output frequency, respectively. The measurements were taken over a 10 s interval. The arrows denote the 3 dB-width of the signal. (b),(d) Repetition rates evaluated from the beating signals using the concept of instantaneous frequency.

is utilized to extract the repetition rate of the laser. Following expression (3.5) the instantaneous frequency of the beating signals, $f_{\mathrm{i}}(t)$, is calculated. Subsequently the frequency of the repetition rate is computed using $f_{\mathrm{i,\,rep}}(t) = |f_{\mathrm{i}}(t) - f_{\mathrm{LO}}|\,/m$. The resulting deviation of the repetition rate from its mean value over the measurement period of 10 s is shown in figure 3.7 (b) and (d). In (b), short-time fluctuations on the order of 1 Hz are present. In addition to these short-time fluctuations, in figure 3.7 (d) a large drift of the repetition rate over a range of 10 Hz is visible. This reflects the large spectral width of the beating signal shown in (c). The observed fast fluctuations as well as the long-term drift are the result of various technical and fundamental noise sources of mode-locked Ti:Sa lasers as introduced in section 2.2. In optimal operational conditions, large drifts are uncommon and the noise characteristics are dominated by the short-time fluctuations on the order of 1 Hz.

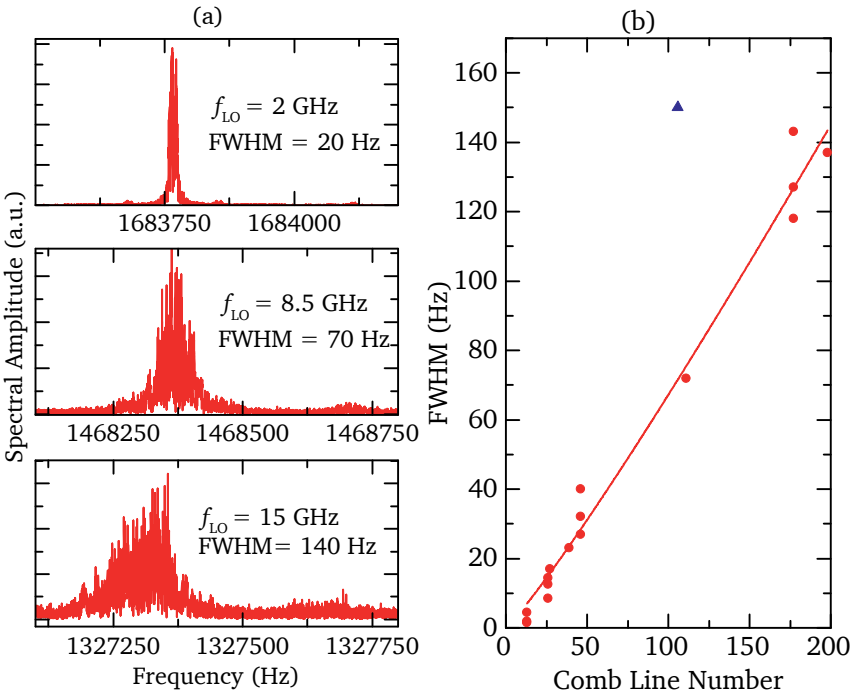

Figure 3.8 (a) Spectral amplitudes of beating signals between the rectified optical comb and a local oscillator signal at different frequencies. (b) Relation between the comb line FWHM and its mode number between line #13 (≈1 GHz) and #198 (≈15 GHz). The straight line denotes a least square approximation of the expression $A \cdot n^{2/p}$ with $A = 0.405$ Hz and $2/p = 1.110$. The triangle corresponds to an uncommonly large fluctuation of the repetition rate, excluded from the approximation.

Evaluating beating signals at different LO frequencies, an estimate of the frequency-dependent width of the optical comb lines is obtained. Figure 3.8 (a) shows the resulting beating signals at LO frequencies (comb-line numbers) of 2.051 GHz ($n = 27$), 8.423 GHz ($n = 111$) and 15.027 GHz ($n = 198$). These measurements were realized by an additional amplification of the photodiode signal as compared to the spectrum shown in figure 3.5. The corresponding FWHMs of those and of additional measurements are given with respect to their comb line numbers in figure 3.8 (b). Here, also measurements of the comb line width using a signal analyser (Agilent E4440A) are included (comb line numbers 13 to 40). A least-square approximation of a scaling function of the form $A \cdot n^{2/p}$ for the comb line width, refer section 2.2 and [102], results in a nearly linear de-

pendency between the line number and the FWHM, with an exponent of $2/p = 1.110$ and a coefficient of $A = 0.405$ Hz. The parameter $p = 1.8$ indicates that the noise behavior seen in the experiments is not solely based on effects occurring in the Ti:Sa crystal (which would result in $p = 3$ according to [102]), but also incorporates additional effects, most likely attributed to the fluctuations of the laser cavity length. It is important to emphasize that the scaling function only yields an estimate for the resulting FWHMs of the measured beating signals at different mixing frequencies. As indicated in figure 3.7, the repetition rate of the laser may largely drift. Especially for long measurement periods and high mixing frequencies, this significantly affects the FWHM of the beating signals. For instance, such a drifting behavior is assumed to be responsibly for the increased FWHM at the $n = 106^{\text{th}}$ comb line, as shown by the triangle in figure 3.8 (b).

After the analysis of the repetition rate fluctuation, the mixing process between the cw signal of a frequency multiplier emitting at $f_{\text{THz}} = 100.02$ GHz and 99.99 GHz and the THz frequency comb is demonstrated. With a repetition rate of ≈ 76 MHz, it follows for the measurement of the free-space signal that the mixing process (for both frequencies) utilizes the $n = 1316^{\text{th}}$ line of the THz frequency comb. In figure 3.9, the normalized spectral power of the beating signals obtained from a 10 s measurement interval using either the PC- or the EO-based detection scheme are shown. For comparable distances of about 2 cm between the detection apparatus and the THz source, the PCA-based measurements show a higher signal-to-noise ratio (SNR) as compared to the EO detection. The results given in figure 3.9 are representative throughout a multitude of measurements, equally reflecting the relative behavior in different experimental geome-

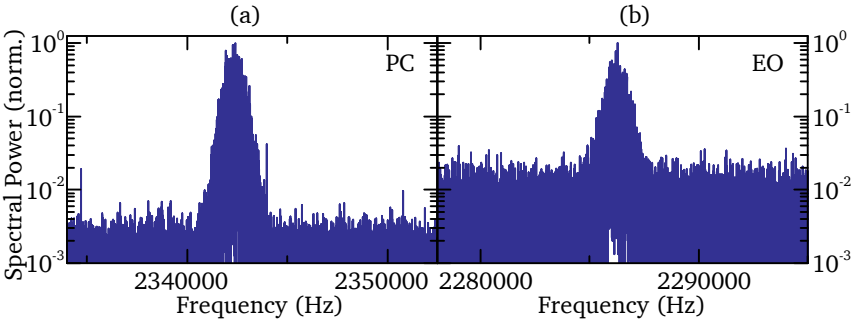

Figure 3.9 Normalized spectral power of the beating signal of a free-space signal at $f_{\text{THz}} = 100.02$ GHz, obtained via (a) photo-conductive and (b) electro-optic detection.

tries with respect to the position of the THz source. Thus, the detection sensitivity of the PCA-based measurement is found to be higher as compared to the EO detection. However the 3 dB width of the beatings is comparable for both detection methods, with $\mathrm{FWHM_{PC}} = (1400 \pm 24)$ Hz and $\mathrm{FWHM_{EO}} = (1295 \pm 33)$ Hz being the resulting mean values with the corresponding standard deviation of the mean, obtained by a variety of measurements. These results roughly agree with the calculated value according to the scaling behavior of the comb line FWHM with the comb line number, $A \cdot n^{2/p}$. With the parameters for A and $2/p$ derived from the measurements shown in figure 3.8, a FWHM of 1174 Hz is predicted for the 1316^{th} comb line.

For the measurements shown in figure 3.9, the mixing comb line number n has been deduced in a straightforward way by dividing the frequency of the free-space signal, f_{THz}, by the laser repetition rate f_{rep}. In general, the frequency of the source to by analyzed cannot be considered as a known quantity. In such a case, the random drift of f_{rep} allows for an easy determination of n. In figure 3.10, two consecutive measurements of the beating signal between f_{THz} and the THz comb are shown. They were recorded several seconds apart. In this time, the repetition rate has changed by 13.58 Hz. This results in a shift of the center position of the beating signals of about 17876 Hz, which reveals n according to equation 2.38. This simple calculation depends strongly on the accuracy of the determination of the incorporated frequency shifts. To avoid miscalculations due to the uncertainty of the frequency measurements, a large shift of f_{rep} is beneficial as can be seen in table 3.1. For the 100.02 GHz source and 10 s measurement intervals, a repetition rate shift larger than 10 Hz is necessary to obtain a reliable value for n.

In the next step, the application of the transfer concept is demonstrated. As shown in figure 3.11, the combination of the simultaneously recorded measurements of the beating signals at frequencies of $f_{\mathrm{b,rep}}$ and

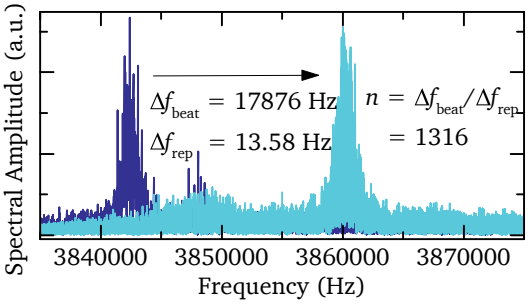

Figure 3.10 Two consecutive measurements of the THz beating signal. The drift of the laser repetition rate in between both measurements results in a drift of the beating signal's position. The ratio of both shifts equals the mixing comb mode n.

#	$f_{\mathrm{b,THz}}$ (Hz)	f_{rep} (Hz)	$\lvert\Delta f_{\mathrm{b,THz}}\rvert$ (Hz)	$\lvert\Delta f_{\mathrm{rep}}\rvert$ (Hz)	n_{exp}
1	3853757.39	76000111.18			
2	3860023.62	76000106.37	6266.23	4.81	1302.75
3	3842147.62	76000119.95	17876.00	13.58	1316.35
4	4432921.82	75999671.06	590774.20	448.89	1316.08

Table 3.1 Experimental deduction of $n_{exp} = \left|\frac{f_{b,THz}}{f_{rep}}\right|$ using different measurements of $f_{b,THz}$. The true value is $n = 1316$. The larger the shift of the repetition rate between two measurements, the closer n_{exp} approaches n.

$f_{\mathrm{b,THz}}$ can be utilized to obtain a narrow-band signal following expression (3.2). For the data in figure 3.11, the $m = 46^{\mathrm{th}}$ line of the rectified optical comb has been mixed with the LO signal at 3.4961 GHz, resulting in a beating signal at a frequency of $f_{\mathrm{b,rep}} = 115\ \mathrm{kHz}$. The free-space signal at 100.02 GHz is mixed with the $n = 1316^{\mathrm{th}}$ comb line of the THz comb using a PCA. To eliminate the influence of the repetition rate, the frequency $f_{\mathrm{b,rep}}$ is first changed by a factor of n/m. This results in a signal at 3.29 MHz, which is subsequently mixed with the signal at $f_{\mathrm{b,THz}}$. The mixing product with a frequency f_{cor} shows a resolution-limited peak in frequency domain with a FWHM below 0.1 Hz. This value is equal to the frequency spacing as obtained from a measurement time of 10 s, which is the maximum time interval over which continuous measurements are possible with the available data acquisition hardware. Thus, the influence of the fluctuations of the laser's repetition rate on the corrected signal have been reduced to a level not detectable at the maximal resolution of the measurement setup.

To visualize the SNR of the corrected signal, figure 3.12 (a) shows a semi-logarithmic-scaled plot of the data. A value of about 60 dB for the measurement time and sampling rate as discussed above is realized. Shown in (b) is the corrected beating signal for a measurement based on the EO detection scheme. Here, a reduced SNR is obtained, on the order of 45 dB. For comparison, also the beating signal resulting from a stabilized optical comb is displayed in (c). Using the stabilization mechanism of the laser cavity as described in 2.2 which is based on a phase analysis of the 9^{th} harmonic of the repetition rate, a SNR of 50 dB is obtained. Thus, regarding the detection sensitivity of the measurement system including the correction mechanism, the PCA-based technique is superior to EO detection. Moreover, the correction algorithm outperforms the particular mechanical laser stabilization used in these measurements.

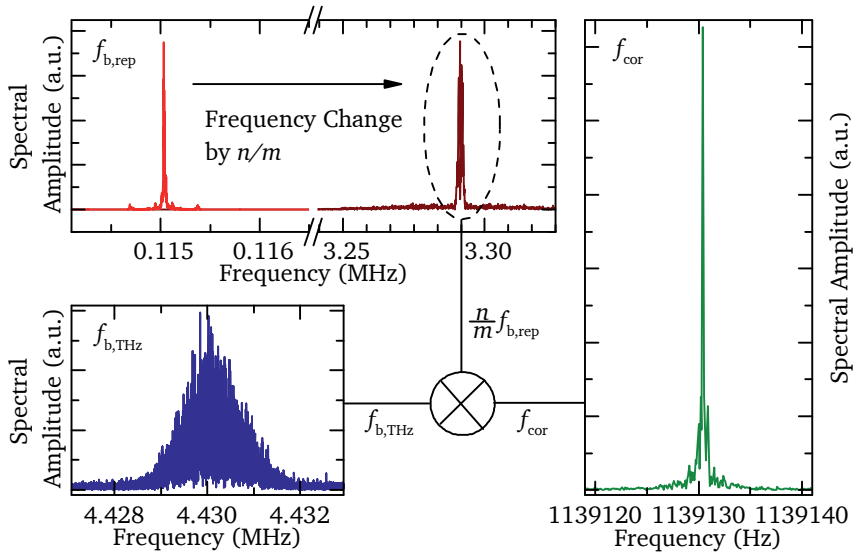

Figure 3.11 Application of the transfer concept: The frequency-shifted beating signal $f_{b,rep}$ is mixed with the beating $f_{b,THz}$. The FWHM of the resulting mixing product f_{cor} is drastically reduced with respect to the measured signals, reflecting the spectral width of the narrow-band THz source and the LO.

To deduce the frequency of the free-space signal from the obtained corrected beating signal, the determination of the frequency of the latter with highest precision is crucial. For this purpose, a software-based frequency counter is utilized. The time-domain waveform as obtained after the application of the correction algorithm is analyzed with respect to the zero crossings over the measurement time. By use of this technique, the frequencies of the signals shown in figure 3.12 are $f_{\mathrm{cor}}^{(a)} = 1139130.434$ Hz, $f_{\mathrm{cor}}^{(b)} = 2608695.661$ Hz and $f_{\mathrm{cor}}^{(c)} = 3999999.899$ Hz (the different frequencies are a result of slightly different settings of f_{LO} and f_{THz}). From these values the frequencies of the THz signal are calculated using relation (3.2). Table 3.2 displays the involved figures of $f_{\mathrm{cor}}, \frac{n}{m} f_{\mathrm{LO}}$ and f_{THz}. For the latter it is distinguished between the set and the measured values.

For all of the three measurements demonstrated, a minor deviation between $f_{\mathrm{THz}}^{\mathrm{meas}}$ and $f_{\mathrm{THz}}^{\mathrm{set}}$ on the order of a few mHz results. However, the smallest difference is obtained for the PCA-based measurement, the worst for the measurement with the stabilized laser. This behavior is exemplary for the different measurement techniques as demonstrated by an evaluation of a multitude of measurements. In figure 3.13, the frequency devi-

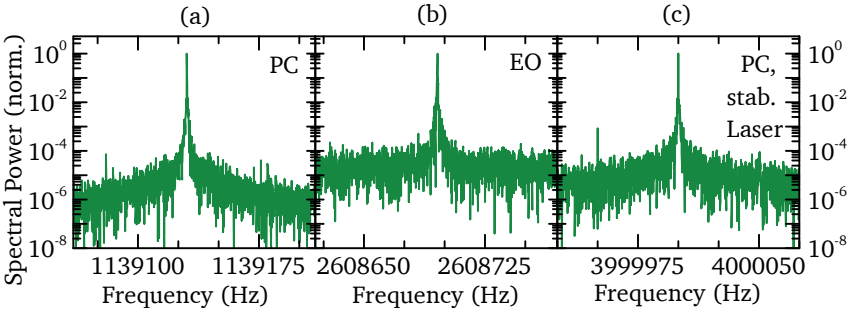

Figure 3.12 Semi-logarithmic plot of (a) the corrected beating signal at f_{cor} shown as right curve in figure 3.11 obtained using a PCA, (b) the beating signal as obtained by an EO measurement and (c) as obtained with a stabilized optical frequency comb using the laser stabilization mechanism.

	f_{cor} (Hz)	$\frac{n}{m} f_{\mathrm{LO}}$ (Hz)	$f_{\mathrm{THz}}^{\mathrm{meas}}$ (Hz)	$f_{\mathrm{THz}}^{\mathrm{set}}$ (GHz)
(a)	1139130.434	100018860869.565	100019999999.999	100.02
(b)	2608695.661	99987391304.348	99990000000.009	99.99
(c)	3999999.899	100016000000.000*	100019999999.899	100.02

*Table 3.2 Experimental determination of the free-space signal's frequency $f_{THz}^{meas} = f_{cor} + \frac{n}{m} f_{LO}$ for the measurements shown in figure 3.12. Additionally, the adjusted frequency f_{THz}^{set} of the THz source is given. For (c), the laser was stabilized and equation (2.37) can be applied directly. The value marked with * denotes the frequency of the $n = 1316^{\mathrm{th}}$ comb mode of the stabilized THz comb ($f_{rep}^{stab} = 76$ MHz).*

ations between $f_{\mathrm{THz}}^{\mathrm{meas}}$ and $f_{\mathrm{THz}}^{\mathrm{set}}$ for more than 20 individual measurements using the PC- and EO-based technique are shown. A statistical analysis reveals a mean frequency deviation with a corresponding standard deviation of the mean of (-0.009 $\pm$ 0.003) Hz and (-0.019 $\pm$ 0.006) Hz for the PC and EO measurements, respectively. The resulting mean deviation obtained using the laser stabilization technique is (-0.079 $\pm$ 0.013) Hz. As can be seen, the PC-based detection technique utilizing the transfer concept offers the highest measurement accuracy and precision. The difference in the standard deviation when compared to the EO measurements is most probably related the slightly differing detection sensitivities of both methods, as shown in figure 3.12. The accuracy of the measurements using the mechanical laser stabilization shows a larger deviation as compared to the data obtained with the correction algorithms. However, since

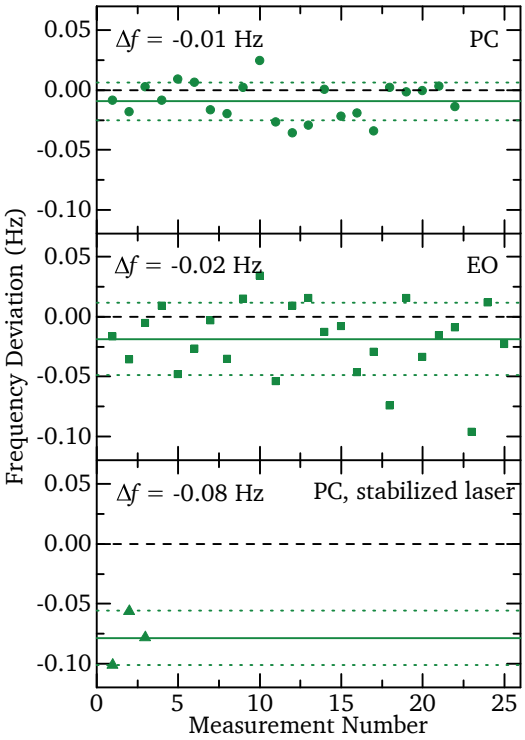

Figure 3.13 Frequency deviation between f_{THz}^{meas} and f_{THz}^{set} for the PC- and EO-based detection techniques. For comparison, also the results obtained with a stabilized optical frequency comb using the laser stabilization mechanism is given. The dotted lines denote the 1σ confidence interval, the dashed lines represent a deviation of zero.

only three measurements using one specific laser have been considered, no detailed conclusions should be drawn with respect to a principle difference in measurement accuracy between both approaches.

Before closing the section about high-precision frequency measurements using THz frequency combs, a last dependency is analyzed. According to the previous considerations, the measurement of the repetition rate fluctuation is best realized using a high harmonic of the fundamental repetition rate. Thus, for the results presented so far, the $m = 46^{\text{th}}$ harmonic has been utilized to obtain a suitable signal at f_{rep} to apply the transfer concept. This value has been chosen since, according to the spectral response of the utilized photodiode and available amplifiers (refer figure 3.5), in this frequency range a suitable detection signal was obtained. With higher amplification of the photodiode signal, even higher mixing frequencies can be realized. To evaluate the influence of the mixing mode on the accuracy of the correction algorithm, additional measurements at higher LO frequencies ($f_{\text{LO}} = 8.0562\,\text{GHz}$, $m = 106$ and $f_{\text{LO}} = 13.4525\,\text{GHz}$, $m = 177$) have been performed. The resulting fre-

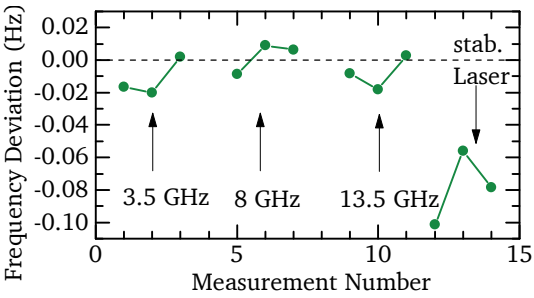

Figure 3.14 Frequency deviation between f_{THz}^{meas} and f_{THz}^{set} for different mixing frequencies of the repetition rate measurement relevant for the application of the transfer concept. For comparison, the frequency deviation obtained with the laser stabilization system is also shown.

quency deviation between $f_{\mathrm{THz}}^{\mathrm{meas}}$ and $f_{\mathrm{THz}}^{\mathrm{set}} = 100.02$ GHz are shown in figure 3.14. Although only a few data points are considered and consequently only a rough estimation of the frequency-dependent behavior is possible, no significant differences in measurement accuracy and precision occur at different LO frequencies. Thus, the choice of the easily accessible 46^{th} harmonic of the repetition rate is feasible. In the scope of this consideration, also the accuracy of the measurement technique based on an active laser stabilization has to be reflected. One possible explanation for the reduced accuracy of the latter with respect to the transfer concept may be found in the fact that the laser stabilization system is based on a mixing process of the 9^{th} harmonic. At low harmonics, a frequency-dependence of the repetition rate measurement precision is expected according to [95], affecting the efficiency of the laser stabilization process. However, also the bandwidth and quality of the piezo transducer incorporated in the stabilization system may be responsible for the reduced measurement accuracy achieved with the stabilized laser.

3.2.5 Summary

To summarize this section, the detection of cw signals at frequencies of 100 GHz has been realized using THz combs based on PC and EO techniques. Analyzing the frequency dependence of the comb line width at low mixing frequencies, the necessity of a correction process for high-precision frequency measurements is evident. Consequently, the determination of the THz comb mode n used for the mixing process is demonstrated. This allows for an application of the transfer concept, correcting the measurement signal for the influence of the repetition rate drifts of the Ti:Sa laser. With this method, signal-to-noise ratios of about 60 dB for the PC-based and about 45 dB for EO-based measurement technique are achieved. Finally, the relative accuracy $\Delta f / f_{\mathrm{THz}}$ for a high-precision frequency measurement is given, with Δf being the mean frequency deviation of the

measured frequency and f_{THz} the signal frequency setting. The PC-based detection setup results in a relative accuracy of $\Delta f_{\mathrm{PC}}/f_{\mathrm{THz}} = (9\pm3)\cdot10^{-14}$. The remaining deviation is most likely caused by the software correction algorithm and the limited data acquisition time of 10 s. The EO-based system allows for a measurement accuracy of $\Delta f_{\mathrm{EO}}/f_{\mathrm{THz}} = (19\pm6)\cdot10^{-14}$ and, by this, differs by a factor of ≈ 2 from the PC-based measurement technique. This minor deviation can be attributed to a decreased detection sensitivity of the measurement process. However, using either PC- or EO-based detection schemes, the introduced correction mechanism outperforms the measurement accuracy achieved with a stabilized frequency comb utilizing the stabilization unit of the laser.

3.3 Amplitude and Phase Measurements

Besides frequency, electromagnetic radiation carries additional parameters of interest: phase and amplitude. Thus, an obvious step following the high-precision frequency measurements of a free-space signal as described in the previous section is given by an extended analysis of the measured signal. Again the beating signal between the radiated field and one comb mode of the THz frequency comb is considered, as expressed by equation (2.37). Assuming a coherent THz source, the observed phase and amplitude values may be determined relatively to a reference signal with the same frequency as the beating signal. Such a technique allows for a detailed study of the emission characteristics of the emitting THz antenna (antenna under test, AUT), i.e. the phase pattern or the spatial distribution of the emitted power may be analyzed. This is demonstrated in the following. First, the fundamental measurement principle will be introduced, then a detailed investigation of spatially resolved emission patterns obtained by EO detection is presented. Finally, a comparison between the PC- and EO-based detection technique is given.

3.3.1 Experimental Setup

The determination of phase and amplitude is realized by a simple comparison of the reference signal at a frequency f_{ref} and the beating signal at $f_{\mathrm{b,\,THz}}$, as schematically shown in figure 3.15 (a). A correction process as described in the previous paragraphs is not necessary, as long as the reference signal contains the same fluctuations of the laser's repetition rate as the THz beating. Such a reference signal may be obtained in several ways. For instance, a purely electronic setup is suitable, comparable to the mixing process between the rectified optical frequency comb and the LO

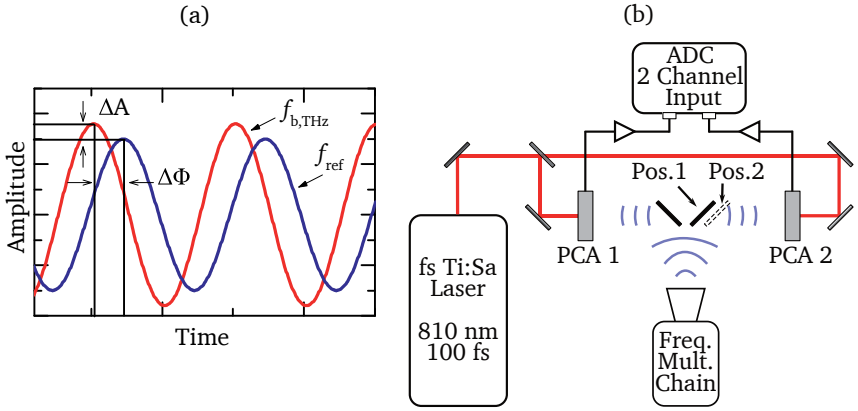

Figure 3.15 (a) Schematic representation of the relative amplitude (ΔA) and phase ($\Delta\Phi$) determination of the beating signal $f_{b,THz}$ using a reference signal f_{ref}. (b) Experimental setup used for the measurement of $f_{b,THz}$ and f_{ref}. Utilizing metal mirrors, the signal of a frequency multiplier chain is split up and detected by two PCAs. Changing the propagation distance between the source and one detector, a change of the relative phase and amplitude is observed.

signal at the frequency f_{LO} as described in figure 3.2. For this, f_{LO} has to be harmonically related to f_{THz}, which is easily realized when the latter is tuned to the same or a multiple frequency of the LO. A different frequency setting of f_{LO} and f_{THz} may be necessary when the THz source emits a signal with a frequency exceeding the bandwidth of the photodiode involved in the electronic mixing procedure. Of course a non-equal frequency of the reference signal and the beating signal requires additional data processing for the phase analysis.

In the following a different approach is introduced in which the reference signal is obtained using a mixing setup based on free-space radiation as well. In this way, the analysis of the radiation pattern of an arbitrary THz source is allowed. Such a source is not necessarily driven by an electronic signal as the frequency multiplier chains used here. To account for this, it is important that the experimental realization is not restricted by an electronic mixing process.

The experimental setup for such a proof-of-principle measurement is demonstrated in figure 3.15 (b). Here, the reference signal is obtained using the field emitted by the AUT itself. The 39.32 GHz-signal of a frequency multiplier chain (HP 83554A Millimeter-Wave Source Module, multiplication factor 2, 26-40 GHz output frequency) is guided onto two PCAs using metal mirrors. To generate the THz frequency combs used for the detec-

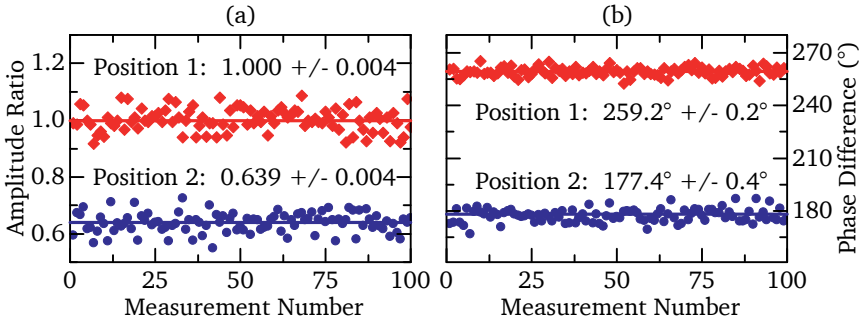

Figure 3.16 Determination of the (a) relative amplitude and (b) phase for two different paths between the signal source and the detector according to figure 3.15 (b) for a signal frequency of 39.32 GHz.

tion of the free-space radiation, the same Ti:Sa laser system as utilized in the previous section is used. The beating signals obtained from both PCAs are recorded using the two-channel ADC as described before. By changing the beam path from the source to one of the detectors by moving the metal mirror as indicated in figure 3.15 (position 1 to position 2), the amplitude and phase relations of both beating signals change. Evaluating 100 consecutive measurements (0.1 s time interval, 10 MHz sample rate) of the relative amplitude ΔA and phase $\Delta\Phi$ at both mirror positions, a drop of the amplitude ratio of about 36 % and a phase change of about 82° results, refer figure 3.16. Thus, with the described measurement technique, spatially resolved emission characteristics of the AUT may be obtained.

However, for a detailed study of the emission properties of the AUT, the given setup is not beneficial. To avoid distortions, the emission of the source should reach the detector without being redirected by a mirror. In such a case, for a spatially resolved measurement scheme a relative movement between the source and the detector has to be realized, whereas the reference detector has to remain in a fixed spatial relation to the source. A suitable experimental geometry may be realized in different ways. But before focusing on this, the usability of the different detection techniques, EO and PC sampling, has to be investigated with regard to their sensitivity and invasiveness. To elaborate on this, a setup is used in which the distortion of the field emitted by the AUT is as small as possible. Hence, the reference signal is obtained from a spatially separated detection setup, using a second cw-THz source. As shown in figure 3.17, two frequency multiplier chains (HP 83554A and Radiometer Physics FE-110) are used, driven by a common signal generator. As AUT a standard gain horn (20 dB gain, 9 mm x 13 mm aperture) is utilized. Similar to the previous setup,

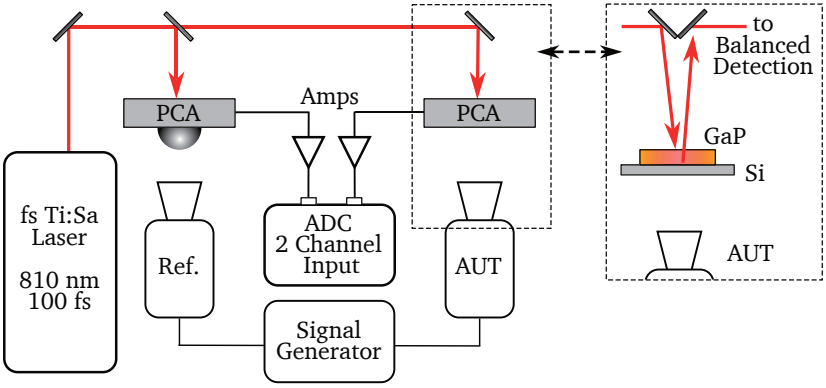

Figure 3.17 Setup for relative phase and amplitude measurements. For the characterization of the AUT, detection methods either based on a PCA or electro-optic detection via a GaP crystal placed on a Si substrate are used.

the measured beating signals are recorded using the two-channel ADC. To compare the performance of the PC- and EO-based detection schemes, the corresponding parts of the setup may be exchanged, as indicated by the dashed boxes in figure 3.17. The PCAs used in the setup are similar to the one described in figure 3.3, although for the characterization of the AUT no silicon lens is attached to the PCA to avoid additional field distortions. The EO-based detection is performed using a 0.5 mm thick GaP crystal. For better handling and to introduce minimal field disturbance, the crystal is attached to a large and homogeneous Si substrate. The backside of the substrate reflects the probe beam towards a balanced detection setup similar to figure 2.9.

To introduce the spatial movement between AUT and detector, the signal source is mounted on a two-dimensional translation stage (Physik Instrumente M-405.DG) allowing for a 5 cm x 5 cm raster-scanning movement with sub-wavelength resolution (step width 0.5 mm), as schematically depicted in figure 3.18.

3.3.2 Spatially Resolved Measurements

In figure 3.19, spatially resolved emission patterns of the intensity and phase measurements of the AUT are shown. Here, the distance between the source emitting at 84.34 GHz and the EO-based detection scheme was 11 cm. According to the antenna dimensions a slightly elongated intensity profile is obtained, figure 3.19 (a). With a dynamical range of about 15 dB over a distance of $\pm$ 2.5 cm (corresponding to an angle of $\pm$ 12.5°),

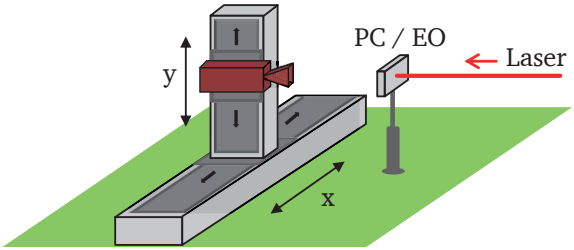

Figure 3.18 To establish a relative movement between the AUT and the detector, the THz source is mounted on a two-dimensional translation stage allowing planar scans over a range of 5 cm x 5 cm.

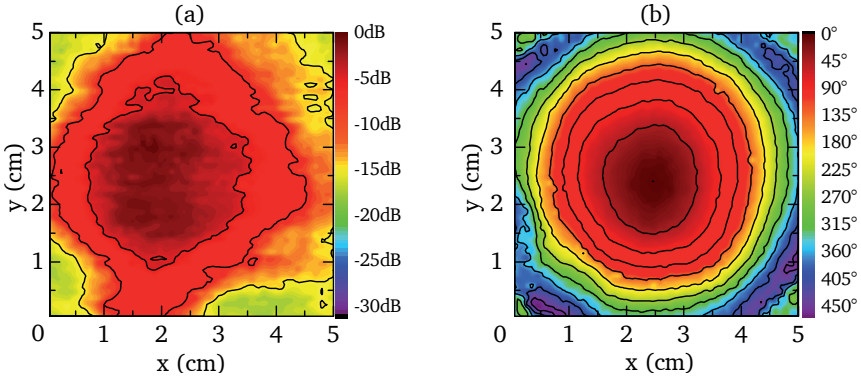

Figure 3.19 Spatially resolved emission pattern of a standard gain horn (20 dB gain) emitting at 84.34 GHz using EO-detection technique. The distance between the source and detector was 11 cm. (a) Intensity; (b) Phase.

typical antenna gain patterns are resembled. The phase pattern, subframe (b), shows a symmetric behavior with more than 2π phase shift. Due to the 11 cm distance between source and detector and the limited traveling range of the translation stage ($\pm$ 2.5 cm), additional features of the AUTs intensity profile, i.e. sidelobes, are not resolved. They are expected to be found at approximately $\pm$ 30°. To access corresponding angular emission directions of the AUT, the distance to the detector has to be reduced. However, at close distances, the spatially resolved measurements do not allow for a straightforward interpretation of the obtained results. Figure 3.20 shows the measured intensity and phase patterns obtained at 1 cm and 5 cm distance to the detector. As visible in the phase patterns, strong distortions of the field are present. The origin of the disturbance in the measurement signal is not clear yet, it may either be related to near-field effects or reflections of the radiated field, causing standing waves between the AUT and the detector. At distances larger than about 6 cm, these effects are suppressed and do not significantly affect the measurements.

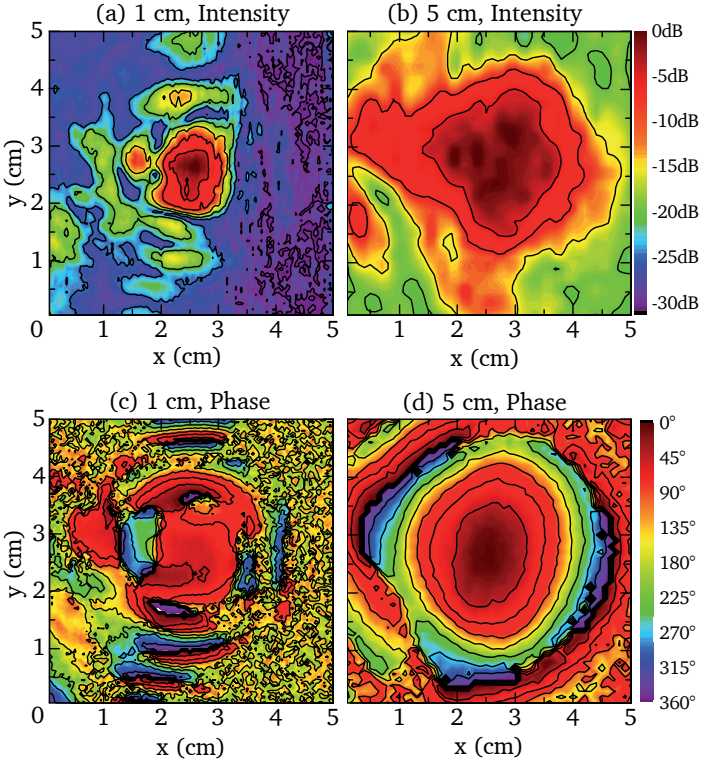

Figure 3.20 Near-field effects on the intensity (upper) and phase (lower) pattern obtained at 1 cm (left) and 5 cm (right) distance between the AUT and the EO-detection scheme. f_{THz} was set to 84.34 GHz.

Although features attributed to the occurrence of side-lobes are observed in the 1 cm intensity pattern, the measurement result is not suitable for a reliable analysis. To investigate the intensity characteristics in detail, a setup providing a larger travel range of the translation stages is necessary.

To continue the comparison between PC- and EO-based detection technique, the measurement accuracy of the experimental setup is evaluated by analyzing amplitude and phase measurements at a fixed positions of the AUT and the corresponding detectors. For this purpose, 100 consecutive 0.1 s long measurements (sampling rate 10 MHz) of the beating signals are recorded at the peak of the AUT's emission cone. Here, the THz source was set to a frequency of $f_{\mathrm{THz}} = 88.47$ GHz. The deviation of each measurement value to the mean is shown in figure 3.21. As can be seen, the resulting standard deviations show slightly different results for

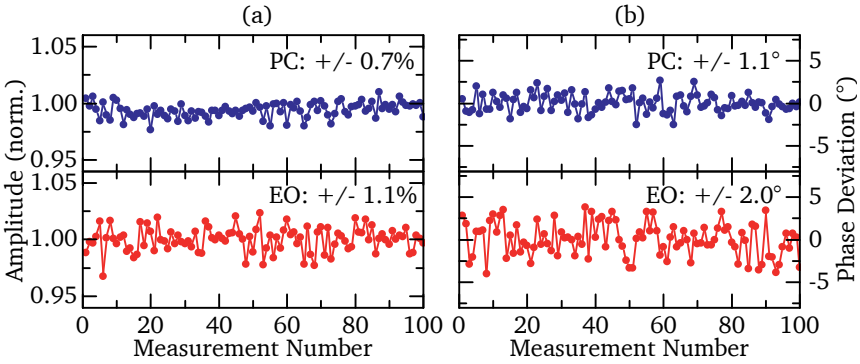

Figure 3.21 (a) Amplitude and (b) phase measurements at a fixed position of the AUT and the reference antenna using the PC- (upper) and EO-based (lower) detection technique. The measurement time for each data point was 0.1 s.

the different detection methods. PC detection yields a standard deviation for a single measurement (standard deviation of the mean) of the relative amplitude of 0.7 % (0.07 %), whereas the EO-based method reaches a value of 1.1 % (0.11 %). For the phase measurements the standard deviation of a single measurement (standard deviation of the mean) is 1.1° (0.11°) and 2.0° (0.20°) for PC and EO detection, respectively.

Figure 3.22 demonstrates another difference of both techniques. The spatially resolved emission patterns for PC- (left) and EO-based detection (right) are not perfectly equal. Here, the upper part of the figure displays the intensity distribution, the lower part the phase distribution of the signal emitted at 100.99 GHz. Both detection techniques reveal a clearly focused intensity distribution of the electromagnetic field. However, while the intensity profile is symmetric in the case of EO detection, strong distortions can be seen in the measurement employing PC detection. This effect is even more dominant for the phase distribution. While EO detection produces a close-to-perfect round shape for the phase, the use of PC detection leads to severe distortions of the measured phase. This is most likely due to reflections resulting from the metallic parts of the PCA. To avoid these reflections corresponding parts such as cables and wires should be removed from the detection devices. This is not that easy for PCAs, which requires electrical connections, while it can be accomplished in a relatively easy way for the EO-based method. Although there are still a number of possibilities to reduce reflections using PCAs, EO-based detection will remain less invasive as it allows for nearly non-distorted measurements. Nevertheless, it has to be emphasized that for both techniques optimization pro-

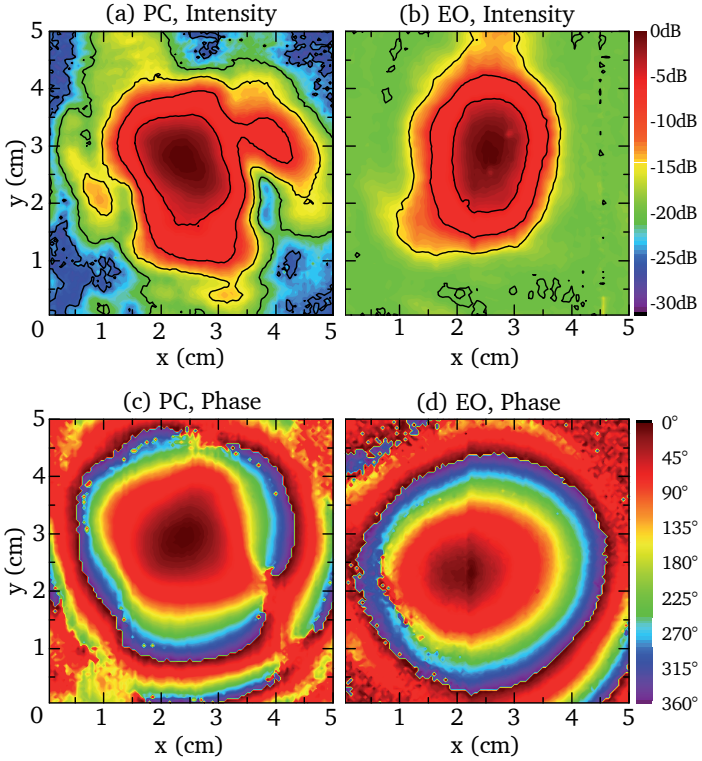

Figure 3.22 Intensity (upper) and phase (lower) distribution of the AUT obtained from a planar scan of 5 cm x 5 cm with 7 cm distance between AUT and the detector. Left: PC detection. Right: EO detection using GaP.

cesses are necessary to eliminate reflections resulting from components of the experimental setup. To demonstrate this issue, in figure 3.23 exemplary measurements using PC and EO detection techniques are shown, where the setup was not perfectly prepared. Severe deviation from the previously shown AUT emission patterns are present, which result from field distortions due to metallic parts of the detector holder. The signal frequency was 28.11 GHz and the distance between source and detector 6 cm.

3.3.3 Summary

To conclude, both PC- and EO-based detection techniques have been utilized to measure the spatial distribution of the amplitude and phase pat-

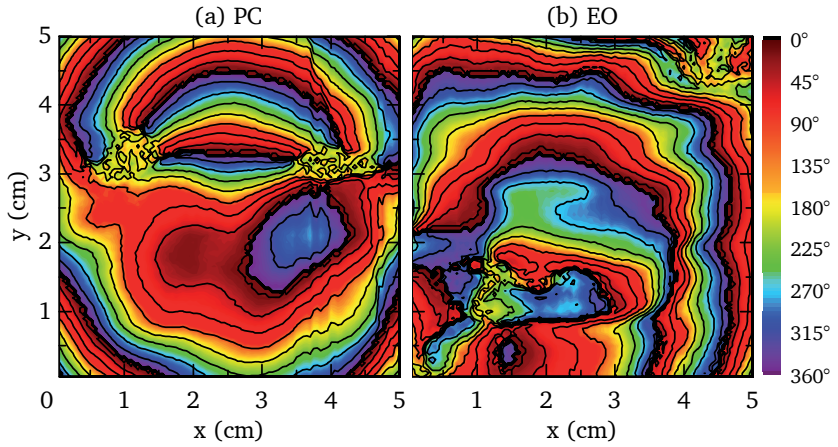

Figure 3.23 Distorted phase patterns due to reflection effects, measured using (a) PC-based and (b) EO-based detection techniques.

tern of an AUT emitting at frequencies between 28 and 100 GHz. Comparing both techniques, PC-based detection offers a standard deviation of 0.07 % and 0.11° for measurements of amplitude and phase, whereas EO-based detection shows a standard deviation of 0.11 % and 0.20°. Also with regard to the measurement sensitivity, PC detection slightly outperforms EO detection. However, since the PCA causes higher field disturbances as compared to an EO detection crystal, using the latter might result in more reliable measurements of the emission characteristics of an AUT.

3.4 Frequency Range

Before concluding the chapter on THz frequency combs, the frequency range of the detection techniques is investigated. As described in subsection 2.3.2, for both the EO- and PC-based method the frequency coverage crucially depends on the temporal width of the optical pulse. The laser system used in this work, refer section 2.2, allows for the generation of pulses with a temporal FWHM of 15 fs and a spectral width of 70 nm $\hat{=}$ 32 THz centered at 786 nm. This is demonstrated in figure 3.24, where in (a) the intensity autocorrelation signal is shown (for the sech^2-shaped laser pulses, the measured $\mathrm{FWHM_{AC}}$ is 1.54 times larger than the actual pulse width $\mathrm{FWHM_{pulse}}$), (b) represents the spectral power of the laser emission. Both are measured at the position of the detection crystal, as will be illustrated later (see figure 3.25). According to the measured tem-

poral and spectral widths, a time-bandwidth product of 0.48 follows. This is slightly above the value of bandwidth-limited sech^2 pulses with a time-bandwidth product of 0.32. Since the laser pulse passes through several optical components till it reaches the detection crystal, the deviation may be explained with a non-perfect correction of the thereby induced chirp by the pulse compressor. Nevertheless, with these laser pulses, both, PC- and EO-based detection should yield a detection bandwidth of about 30 THz. This is examined and analyzed in the following.

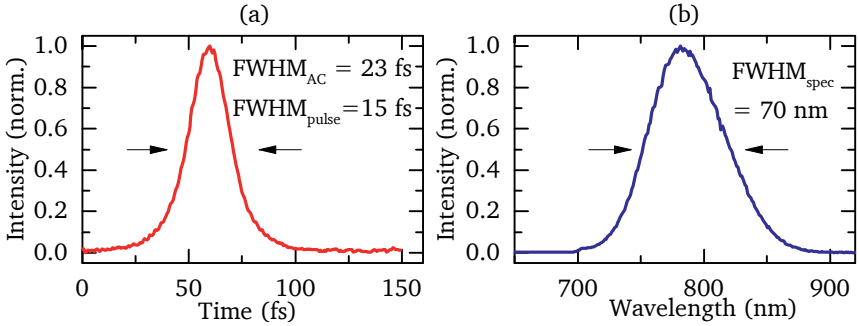

Figure 3.24 Measured autocorrelation and spectral behavior of the optical laser pulse. A time-bandwidth product for the sech^2-shaped puse of 0.48 follows.

3.4.1 Experimental Setup

To investigate the detection bandwidth, the emission of a CO_2 laser tuned to the 10P20 line of the CO_2 spectrum acts as a THz source with a frequency of about 28.323 THz [176], see figure 3.25 (a). Here, a mixing with the $n = \frac{28.3\ \mathrm{THz}}{76\ \mathrm{MHz}} \approx 372000^{\mathrm{th}}$ line of the THz frequency comb is approached. Since the resonator of the CO_2 laser is stabilized via an air-based temperature control mechanism only (as opposed to, e.g., water-based temperature control), the output frequency may not be considered as a stable quantity. Instead, a drifting behavior has to be expected, complicating the exact determination of n.

The CO_2 laser is incorporated into an experimental setup as shown in figure 3.25 (b). The CO_2-laser emission copropagates with the optical pulses emitted by the Ti:Sa laser after utilizing a GaAs wafer in (001) growth direction as beam combiner. The latter acts as a suitable mirror for the Ti:Sa-laser emission and as an attenuator for the CO_2-laser emission. Behind the beam combiner, the beam power is set to about 500 mW and 50 mW for the CO_2-laser and Ti:Sa-laser, respectively. Focusing both beams using a parabolic mirror with 12.5 mm focal length, the PC- and

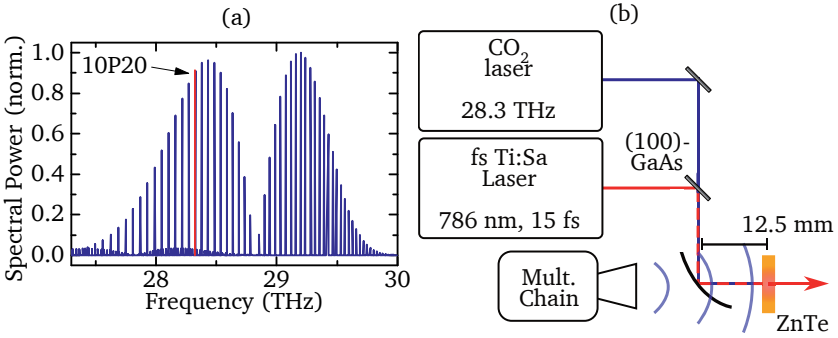

Figure 3.25 (a) CO_2 laser emission spectrum according to HITRAN database. For the demonstration of the frequency range of the detection system, the 10P20 transition at 28.323 THz has been used. (b) Measurement setup for the simultaneous detection of the 28.3 THz-signal and the emission of a 15.8 GHz source. A parabolic mirror with a focus length of 12.5 mm focuses both lasers onto the 0.5 mm thick ZnTe detection crystal.

EO-based detection schemes are placed at the focal point of the 786 nm beam. In figure 3.25 (b), only the setup utilizing a 0.5 mm ZnTe crystal for EO detection is shown. Behind the crystal, the modulated optical beam is guided to the balanced detection setup according to figure 2.9. Alternatively to the EO-based setup, the PCA as introduced in section 3.2 is used.

Additional to the CO_2 laser, a frequency multiplication chain (multiplication factor 2, HP 83554A) is incorporated into the setup as shown in figure 3.25 (b). With the latter operating at a signal frequency of 15.8 GHz, two sources spanning a frequency difference of more than three orders of magnitude are set up.

3.4.2 Measurement Results

Using the introduced measurement setup, indeed two beating signals can be observed. In figure 3.26, the amplitude spectrum of the EO detection signal is shown for a 0.01 s measurement interval, recorded at a sampling frequency of the ADC of 100 MHz. The peak at 19.5 MHz results from the signal of the frequency multiplier, the signal at 28.5 MHz originates from the CO_2 laser. Using a PCA, it was not possible to observe the CO_2-induced signal. This even holds for larger power of the Ti:Sa or CO_2 lasers or using differently shaped PCAs, e.g. using dipole antennas instead of a bow-tie shaped one. Possible explanations for this observation are discussed in subsection 3.4.3.

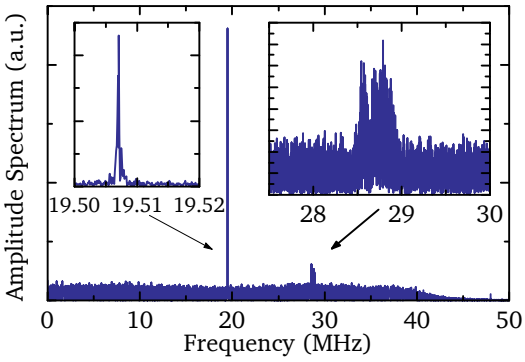

Figure 3.26 Beat notes between the THz comb and the emission of a frequency multiplier chain emitting at 15.8 GHz (left inset) and the output of a CO_2 laser tuned to the 10P20 line (28.3 THz, right inset).

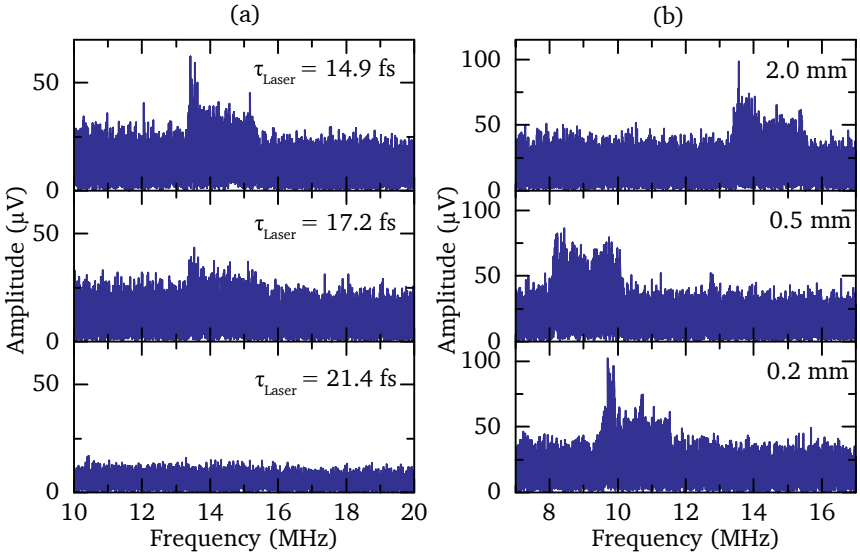

Figure 3.27 Dependency of the beating signal on (a) the pulse width τ_{Laser} of the Ti:Sa-laser emission and (b) the thickness of the ZnTe crystal used for EO detection.

Returning to the EO detection scheme, different parameters influencing the detection signal have been investigated. In figure 3.27 the 10P22 line of the CO_2 emission spectrum is selected for the beating process. Since in this mode the laser operates less stable than compared to the 10P20 mode, the resulting beat signals show a significantly larger width of about 2 MHz. For the 10P20 mode, FWHM values on the order of 0.3 MHz have been obtained. In figure 3.27 (a) the dependency of the beating signal on the pulse width of the Ti:Sa laser emission is shown. The latter has been

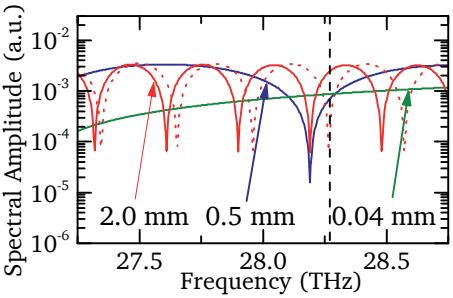

Figure 3.28 Electro-optic transfer function of 0.04 mm-, 0.5 mm- and 2.0 mm-thick ZnTe crystals in the vicinity of the 10P22-line (28.27 THz, dashed line) of the CO_2 laser emission spectrum. The calculations are performed for an optical wavelength of 786 nm. The dotted line corresponds to a crystal width of 2.0 mm and a wavelength of 800 nm.

enlarged from 14.9 fs to 21.4 fs by chirping the optical beam, thereby the spectral width was kept constant. According to subsection 2.3.2, this destroys the coherence in the rectification process. Such a behavior is immediately reflected in the measurement results, where a slight increase of the pulse width goes along with a significant decrease of the beating signal, finally vanishing at about 21 fs pulse width.

A second measurement row, figure 3.27 (b), investigates the influence of the width of the detection crystal on the amplitude of measured beating signal. Again working with 14.9-fs long optical pulses, measurement traces have been recorded using ZnTe crystals with thicknesses of 0.04 mm, 0.08 mm, 0.2 mm, 0.5 mm, 1.0 mm and 2.0 mm. Only for three crystals width, 0.2 mm, 0.5 mm and 2.0 mm, the beating is observed. For these thicknesses, no significant changes in the signal's amplitude result, as can be seen in the figure. According to the electro-optic transfer function as introduced in figure 2.10 of subsection 2.3.2, the detection sensitivity depends on several parameters. Due to the difference in the dispersion properties of the optical beam and the THz signal, the transfer function periodically varies with the THz frequency respectively the crystal width at a fixed frequency of the optical beam. For the center wavelength of the 768-nm probe beam and three crystal widths (0.04 mm, 0.5 mm and 2.0 mm), the transfer function is shown in figure 3.28. The view is restricted to the spectral region around 28.27 THz, corresponding to the 10P22-line of the CO_2 emission spectrum. As can be seen, a variation in the detection sensitivity is expected for the particular crystals widths. However, for the different wavelength components of the optical pulse with a spectral width of 70 nm, the transfer function significantly shifts in frequency. This is indicated by the dotted trace in figure 3.28, evaluated for a crystal thickness of 2.0 mm and a wavelength of 800 nm. As a result, the overall transfer function of the detection method using a broadband optical pulse comprises an averaging process over the involved optical fre-

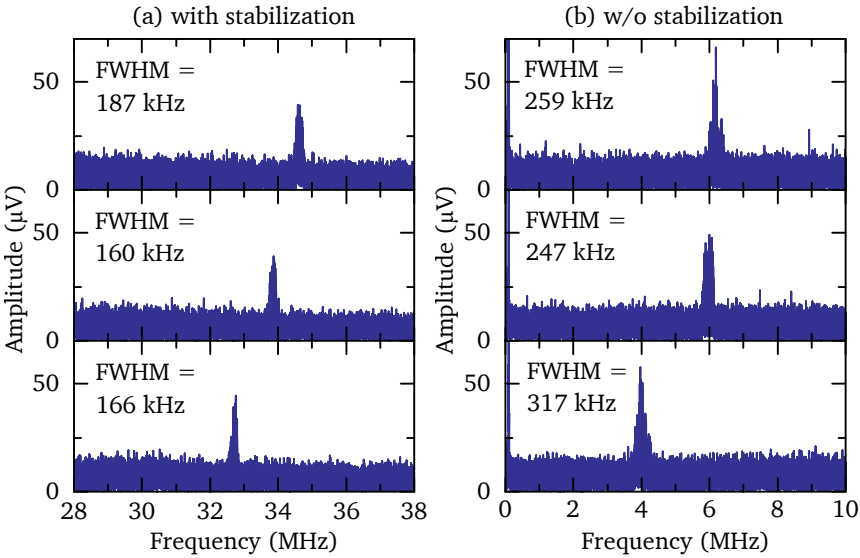

Figure 3.29 Influence of the Ti:Sa-laser repetition rate stabilization technique on the measured beating signal. (a) The repetition rate is locked to a frequency of 76.001 MHz. (b) Measurements obtained without stabilization technique.

quencies. This explains the results shown in figure 3.27 (b), where with a crystal width of 0.2 mm and larger no significant changes in the detection sensitivity are obtained. Most likely, the averaged detection sensitivity of the 0.04 mm and 0.08 mm crystal is not high enough to allow for the detection of the CO_2 emission. This has to be confirmed in further studies. For the specific 1.0 mm crystal used in the measurement row, subsequent investigations showed an overall reduced detection sensitivity which has to be related to a poor crystal quality. Details may be found in appendix A.

The beating signals depicted in figure 3.27 (b) show a large fluctuation of their mean frequencies throughout the different measurements recorded several minutes apart. To analyze this behavior in more detail, the influence of the repetition rate drift of the Ti:Sa laser is minimized by use of the stabilization unit of the device and locking the repetition rate to 76.001 MHz. Again using the 10P20-emission line, the measured beating signals obtained with and without stabilization mechanism are shown in figure 3.29 (a) and (b). Contradictory to the measurements obtained with the frequency multiplier chains as demonstrated in section 3.2, the stabilization of the comb results in minor differences for the CO_2 laser-induced beatings. The FWHM of the signals is reduced by less than a factor of 2, the

drifting behavior is hardly affected. Thus, the remaining frequency drift and the width of the signals is attributed to the drift of the CO_2 laser emission frequency. The temperature stabilization of the laser cavity using air coolers is not sufficient to realize a fixed-frequency THz source. A stable frequency is necessary to apply the high-precision frequency measurement scheme including the transfer concept. Otherwise, the determination of n according to equation (2.38) is not possible.

3.4.3 Summary

In this section, the response of the PC- and EO-based detection schemes has been investigated with regard to a high-frequency signal at 28.3 THz. Although for both detection techniques a frequency range reaching up to 30 THz was expected, only the EO measurement technique yields a beating signal. Here the signal-to-noise ratio hardly exceeds 2, reflecting that the measurements are performed at the frequency limit of the detection technique. This is confirmed by a variation of the coherence properties of the optical frequency comb, where a slight increase of the pulse width results in significant drop of the detection sensitivity. By this the importance of a bandwidth-limited setup is emphasized, providing a spectral width of the optical frequency comb larger than the signal to be measured.

Also for PC detection, the Ti:Sa laser fulfills the necessary conditions to extend the measurement range to several tens of THz. However, since no signal has been detected, it is assumed that the simplifying assumption of a frequency-independent carrier mobility as given in equation (2.36) does not hold at frequencies of 28.3 THz. A reduced mobility will result in a decreased detection sensitivity of the PCA, such that the corresponding signal-to-noise ratio is not high enough to allow the observation of the beating signal. To investigate this further, a more detailed approach utilizing a frequency-dependent mobility as for instance given in [139] is necessary.

Finally, the properties of the available CO_2 laser are revealed to be insufficient to utilize the latter as a signal source for high-precision measurement scheme. Due to the frequency drift over the measurement window, the application of the transfer concept is not possible.

Nevertheless, it is demonstrated that by use of EO detection, an ultrawide frequency range from GHz to THz frequencies is covered. Although phonon resonances occurring in the frequency-dependent susceptibility $\chi^{(2)}(\omega)$, e.g. at about 5.1 THz in the case of ZnTe, reduce the detection sensitivity at these frequencies, this may be circumvented by changing the detection material and use, e.g., GaP. (Refer table A.1 in appendix A for a list of phonon resonance frequencies for different materials.)

3.5 Summary and Outlook

In the three preceding sections, the usability of first- and second-order based effects of the semiconductor susceptibility has been investigated with regard to the detection of cw radiation in the GHz and THz frequency range. Utilizing PCAs for PC detection (first-order effects) and ZnTe or GaP for EO detection (second-order effects), both detection techniques have been analyzed concerning their high-precision frequency measurement capability (section 3.2), spatially resolved amplitude and phase measurement schemes (section 3.3) and the frequency range of the detection process (section 3.4).

Resuming the main findings and focusing on the comparison between PC and EO techniques, a detailed view is necessary to outline the advantages and disadvantages of both techniques. For the high-precision measurement technique, the investigations clearly approve that both methods accomplish highest measurement accuracy. After suppressing the noise contribution of the Ti:Sa laser, either technique outperforms previously published results for the frequency measurement accuracy of the measurement setup [53,55,58], reaching values of $\Delta f_{\mathrm{PC}}/f_{\mathrm{THz}} = (9 \pm 3) \cdot 10^{-14}$ and $\Delta f_{\mathrm{EO}}/f_{\mathrm{THz}} = (19 \pm 6) \cdot 10^{-14}$ for PCA- and EO-based measurements over a 10-s long sampling period, respectively. The reduced detection sensitivity and, correspondingly, the enhanced noise figure of the EO-based method suggests that an improvement of the experimental setup will result in an even better agreement of both PC and EO detection method. Here, especially differences in the utilized electronic components (i.e., the balanced detector and the amplifier) have to be investigated. It has been shown that under certain experimental conditions the spectral response of both techniques may coincide [138]. However, since PC detection strongly depends on the individual properties of the PCA, this may not be generalized.

For both detection methods, the experiments shown here indicate a systematic difference of some mHz between the frequency setting and the mean value of the measured values. Subsequent studies have to be performed to investigate this issue in more detail. Most likely, the correction algorithm used for the application of the transfer concept causes this systematic error. Next to the approach described here, also different hardware- or software-based realizations may be applied and compared to the solution presented so far. Another approach to narrow down this issue is given by an longer data acquisition period as possible with a different experimental hardware. Extending the measurement time by one or two orders of magnitude, more precise measurements are achieved. With the reduced fluctuation of the measurement values, a deviation between measured and expected values may be interpreted more clearly.

Concerning the results of the spatially resolved amplitude and phase determination, the measurements presented here provide a proof-of-principle study for antenna characterizations utilizing THz frequency combs. The achieved dynamic range (35 dB and 20 dB for PC and EO detection, respectively), amplitude stability (0.07 % and 0.11 % for PC and EO detection) and phase sensitivity (0.11° and 0.20° for PC and EO detection) is sufficient for the analysis of THz emission patterns of a 10dBm signal source. This is true for both detection methods. Again the PCA-based measurements show a better performance with regard to the signal-to-noise ratio, nevertheless the EO detection scheme is more suitable for characterization purposes due to the reduced invasiveness of the method. However, the work as demonstrated here does only allow for measurements over a small angle of the emission cone due to the limited travel range of the utilized translation stages. To finally conclude on this topic, measurements over a larger area are necessary. Currently, such work is in progress [B1], using 30 cm translation stages. Here, the measurement technique is even expanded to a quantitative measurement of the amplitude.

Regarding the spectral coverage of the PC and EO detection scheme, it has been expected that both methods yield comparable results at low frequencies as well as for 30 THz. This has not been confirmed. PC detection does not allow for a straightforward implementation of the described measurement technique at the far end of the former THz gap. To further investigate the behavior of PCAs at high frequencies, the fabrication of samples with various electron mobility is necessary. By this, the resulting influence of this parameter onto the spectral response of the PCAs may be analyzed further. Additionally, an optimization of the RC-constant of the utilized antenna structure could result in a better response at 30 THz. Nevertheless, also for EO detection the obtained signal-to-noise ratio of the measurement signal is hardly satisfactory. To large extent, this may be attributed to the drifting behavior of the emission frequency of the utilized CO_2 laser. Clearly, additional investigations utilizing different THz sources are necessary for a deeper analysis of the applicability of the transfer concept at high THz frequencies. Here, the use of quantum cascade lasers seems promising due to sophisticated stabilization techniques of their emission frequencies.

As a final remark it has to be emphasized that most of the measurements shown in this chapter are based on an optical frequency comb without stabilization mechanism. This demonstrates that even for highest measurement accuracy free-running laser systems may be employed. Thus an attractive solution is introduced, allowing for mobile, less costly and highly flexible measurement schemes for the accurate and precise detection of cw-THz radiation.

4 Coherent Control of Steerable THz Emitters

4.1 Motivation and Review of Previous Work

As introduced in chapter 1, the last decade in THz research resulted in an extensive growth of the availability of THz systems and THz sources. However, concerning one specific aspect the development falls behind: still there is a critical the lack of appropriate active system components, capable of dynamically modifying the emission properties of the THz radiation. Especially for applications based on imaging and spatially resolved spectroscopy, sophisticated methods for the steering of the THz direction are needed [59]. In order to solve this issue, various technical realizations have been proposed. Here, it may be divided into approaches utilizing a spatial movement of the THz source or of the emission system [177–179] or using diffractive elements like gratings [121, 180–184]. However, the mechanical movement of components within a measurement setup limits the speed of the measurement process and diffraction effects usually show strong frequency-dependent steering angles. Thus, the development of techniques that allow for non-mechanical and broadband steering of the THz beam is desirable.

In this chapter, an alternative approach for a pulsed, steerable THz emitter is presented which fulfills these demands. Via all-optically generated currents in a semiconductor material like GaAs, THz emission is induced. Due to the properties of the semiconductor and the excitation conditions, different types of currents are generated, namely SF and shift currents as described in section 2.3.1. Interference effects of the corresponding electromagnetic fields emitted by these currents result in a spatially directed emission pattern. Via the properties of the optical excitation, the behavior of one of both current contributions is modified and, accordingly, the THz emission pattern changes. By this, a fast and reliable mechanism for THz beam steering is realized, allowing for steering angles of more than 8° [A2].

The structure of this chapter is as follows. Section 4.2 schematically introduces the temporal shapes of the THz fields emitted by the induced currents. The resulting interference effects of the fields are described. In section 4.3, the experimental setup used for the demonstration of the steering effect is presented. An analysis of the obtained measurements is given. To gain a better understanding of the underlying dependencies, chapter 4.4 introduces a simple dipole model capable of simulating the measured field distribution. With the help of this model, the current behavior is investigated in more detail. Based on the hereby obtained results, chapter 4.5 gives an outlook regarding a further optimization of the demonstrated THz steering effect.

4.2 Schematic Description

The directed emission of THz radiation as described in the following is based on all-optically induced currents in semi-insulating GaAs. Unlike noted otherwise, the samples are cut such that the surface is parallel to the (110) plane of the crystal structure. To simplify the notation, the $[001]$, $[1\bar{1}0]$, and $[110]$ axes are denoted as the x, y, and z axes, respectively. In general, the optical excitation of the material using photons with above-band-gap energy $\hbar\omega > E_{\text{gap}}$ results in complex carrier dynamics. By utilizing specific properties of the carrier generation process, two different effects may be combined to induce the THz steering mechanism. In section 2.3.1, these two current generation processes have been introduced. First, the drift-based surface field (SF) current occurs. Second, all-optically controlled shift currents may be induced. As discussed in the theoretical introduction, the current flow directions of both currents depend on the pump light and crystal properties. The latter affects the SF current via the band structure. The shift current highly depends on the relative orientation of the crystal's axis system with respect to the pump polarization. In figure 4.1, both mechanisms are depicted schematically and the corresponding electron flow directions with respect to the coordinate system of the GaAs crystal are visualized. With regard to the direction of the band bending, intrinsic GaAs behaves comparable to n-doped GaAs, reference [110], and shows a curvature of valence and conduction band as depicted in figure 2.4 (b). As a result of this bending direction, the electron movement is directed into the GaAs material, refer figure 4.1 (a). A SF current flow perpendicular to the semiconductor surface results. For the crystal orientation used in the following experiments, this equals a current flow along the z-axis. In contrast to this, the shift current flow direction may be controlled by the polarization of the pump light. According

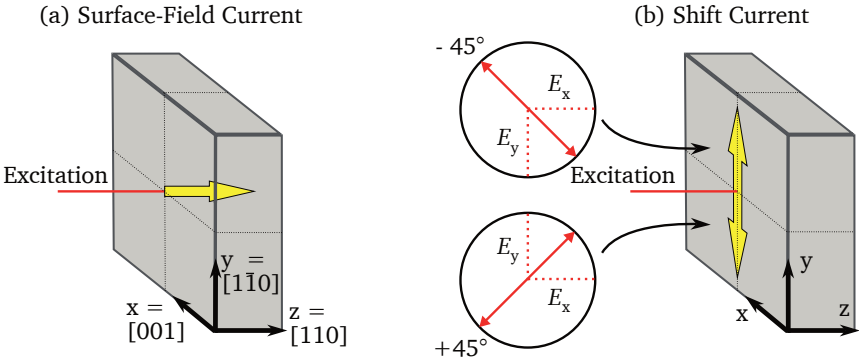

Figure 4.1 Schematic representation of the all-optically induced electron movement in intrinsic GaAs cut along the (110) direction. (a) The surface-field current flows perpendicular to the surface of the crystal. The generation mechanism does not depend on the polarization of the pump light. (b) In contrast, the sign of the in-plane shift current along the y direction may be reversed by rotating the linear polarization of the pump light by 90°.

to equation (2.31) and table 2.2, current flows in x, y and z-direction may be optically induced. However, for pump light at normal incidence and a (110) crystal geometry, only shift currents along x and y are allowed. Especially the current flow along y is of interest for the THz steering mechanism. Following expression (2.32), the current direction depends on the relative phase of the electrical polarization components along x and y. In figure 4.1 (b), this dependency is depicted schematically. Applying normally-incident pump light with a linearly polarized field at an -45° angle with respect to the crystal's y-direction, an electron flow along the positive y-direction is induced. Rotating the linear polarization by 90°, i.e. adding a phase of 180° to the y-component of the electrical field, the electron flow direction reverses and points towards the negative y-direction.

4.2.1 Temporal Shape of the THz Traces

To introduce the emission of pulsed THz signals and to briefly outline the expected waveforms for both SF and shift current, figure 4.2 relates the THz trace to the induced current flow. In (a), the current density J is shown. Here, it is assumed that the current instantly follows the Hyperbolic-Secant-shaped intensity profile of the laser pulse with a FWHM of 100 fs centered at $t = 1.0$ ps. This assumption is approximately realized for both SF and shift current. Regarding SF currents, equation (2.26) shows that the carrier density is connected to the generation term G,

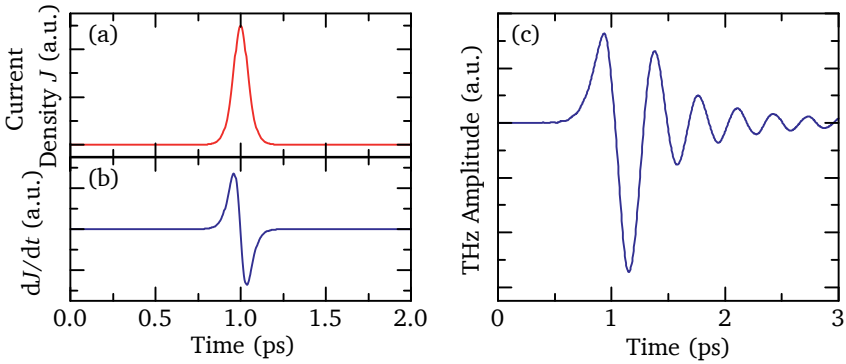

Figure 4.2 (a) Current flow J with 100 fs FWHM. In (b), the time derivative of J is shown, equaling the initial THz field radiated into space. Due to propagation and detection effects, the measured THz trace deviates from the latter, as shown in (c) for a detection crystal of 0.5 mm thickness.

which is proportional to the intensity envelope of the laser pulse. The excited charge carriers are instantaneously accelerated by the static SF. Thus, the onset of the current flow follows the laser pulse. The decay of the current is governed by the shielding of the SF by the separated charge carriers. The shielding takes place on a sub-ps time scale as well [115]. The exact duration until total shielding is reached depends, among other influences, on the amount of charge carriers created. For the excitation densities reached here, it is expected that the falling edge of the current pulse is slightly slower than the rising edge. However the order of magnitude of rise and fall time is assumed to be comparable. The temporal behavior of the shift current is given by equation (2.32), which shows a direct proportionality between the time-dependence of the current flow and the laser pulse envelope.

For both currents, the radiated field resembles the time derivative of the current pulse. Hence, in figure 4.2 (b) the derivative of (a) is shown. The first peak is attributed to the fast rising edge of the current pulse, having a similar form for SF and shift current. If the dynamics of the SF and shift current pulse deviate, this should be reflected by a different evolution of the second peak of the radiated field. However, the exact determination of the radiated fields is difficult due to additional effects inherent to the detection mechanism. Due to propagation effects of the radiated fields [155] and, most importantly, the electro-optic sampling process utilized for the measurement of the THz pulse [151, 154], the recorded waveform deviates from the radiation emitted by the current flow. Figure 4.2 (c) demon-

strates this effect, showing the influence of the sampling process on the signal given in (b). In this simulation, a 0.5 mm thick ZnTe crystal and a 100-fs long probe pulse at 810 nm are assumed, resembling the experimental conditions described in section 4.3. The measurement process acts as a low-pass filter, suppressing the high-frequency components of the signal (refer subsection 2.3.2). Additionally, due to the influence of electro-optic sampling process, the main THz signal is followed by a damped oscillating signal. Despite the deviations between (b) and (c), the main features of the signal as for instance the current flow direction or the spectral components up to approximately 4 THz are contained in the measurement process. This will be utilized in the following to demonstrate the THz steering effect.

4.2.2 Interference of the Emitted Fields

As described before, a temporal dynamic of the current flow on the order of the optical pulse length is expected. Hence, with such short current pulses the emission of THz radiation goes along. Using the most simple model, the current pulses may be regarded as small dipole emitters, oriented parallel to the current flow directions. Using this picture, the emitted fields can easily be modeled. For the geometric orientation given in figure 4.1, a notation as shown in figure 4.3 is used. According to the crystal axis system with the (110)-plane parallel to the xy-plane of the coordinate system, θ defines the polar angle between the y-axis and the position vector $\mathbf{r}$. ϕ denotes the angle between the projection of $\mathbf{r}$ onto the xz-plane and the z-direction. Expressed in spherical coordinates, the far field component of the dipole pattern at a distance r is given by a contribution along the $\hat{\theta}$-direction [185]. Depending on the orientation of the dipoles, a sinusoidal and a cosine behavior results for the shift current

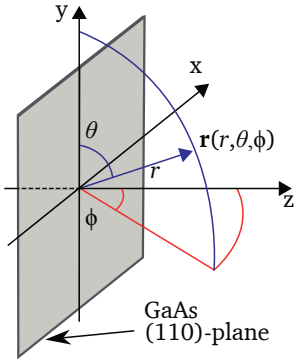

Figure 4.3 Position vector $\mathbf{r}(r, \theta, \phi)$ in the coordinate system of the (110)-cut GaAs sample according to the experimental setup used in the following. θ denotes the polar angle between the y-axis and $\mathbf{r}$, ϕ the azimuth angle between the z-axis and the projection of $\mathbf{r}$ onto the xz-plane.

dipole oriented along y and the SF current dipole directed parallel to the z-axis, respectively.

$$\mathbf{E}^{\text{Shift}}(\theta, \mathbf{r}) \propto \frac{\sin\theta}{r}\hat{\theta},$$
$$\mathbf{E}^{\text{SF}}(\theta, \mathbf{r}) \propto \frac{\cos\theta}{r}\hat{\theta}. \tag{4.1}$$

Figure 4.4 (a) shows the corresponding electrical fields E_{SF} and E_{Shift} emitted from the dipoles p_{SF} and p_{Shift} attributed to the SF and shift current, respectively. The view is restricted to an intersection along the yz-plane of the experimental geometry. In the figure, the shift current dipole oriented along positive y-direction with its corresponding field is depicted. Although the main emission direction of the SF dipole is oriented in the xy plane, non-zero electrical field components have to be considered even for small deviations from the z-direction. Regarding the superposition of both dipole fields, interference effects occur. Due to the rotational symmetry along the z-axis, the sign of E_{SF} is different on either side of the excitation spot along y. This leads to destructive and constructive interference between E_{SF} and E_{Shift} at the upper and lower side, respectively, of the emission pattern. As a consequence the overall emission pattern is tilted by an angle β with respect to the z-direction as shown in figure 4.4 (b). By inverting the direction of the shift current, i.e. the direction of the corresponding dipole, the interference effect and, consequently, the tilt angle

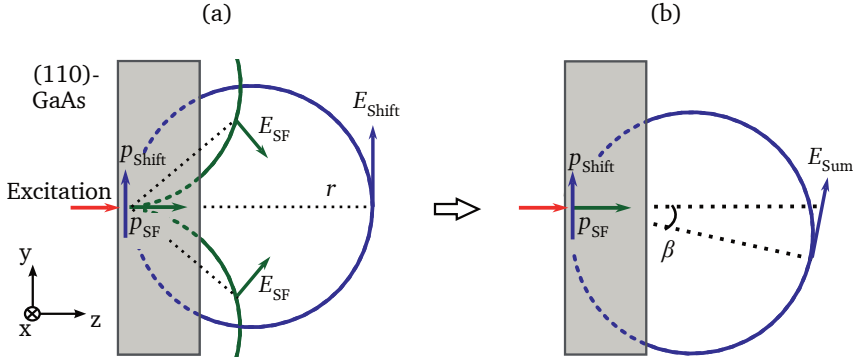

Figure 4.4 Schematic representation of the steering mechanism. In (a), the individual THz fields emitted from shift and surface-field (SF) dipole are shown. In (b), the resulting overall emission pattern is depicted, tilted by an angle β with respect to the surface normal. For reasons of clarity, refraction and diffraction effects are not included in the scheme.

can be reversed. This mechanism allows for a coherently controlled steering of the direction of the overall THz emission. As will be described in section 4.4, this simple model reproduces the experimental observations of the THz steering effect very well. It should be noted that the model takes refraction and diffraction effects into account as well. For sake of simplicity, those are not included in figure 4.4.

4.3 Experimental Demonstration

4.3.1 Experimental Setup

To induce and detect THz emission resulting from current pulses in GaAs, an electro-optic sampling setup for pulsed radiation as described in subsection 2.3.2 is utilized. According to equation (2.40), a detection signal proportional to the field amplitude at a certain relative time delay between probe pulse and THz pulse results. Figure 4.5 shows the experimental setup used for the measurements. To excite the GaAs sample and to detect the emitted radiation, the Ti:Sa laser system described in section 2.2 is used. At a central frequency of 810 nm, pulse widths of about 100 fs are obtained. The emitted pulse train is divided into pump and probe pulses. The pump light is focused onto the (110)-oriented GaAs sample using a 150 mm lens. Depending on the distance between the lens and the sam-

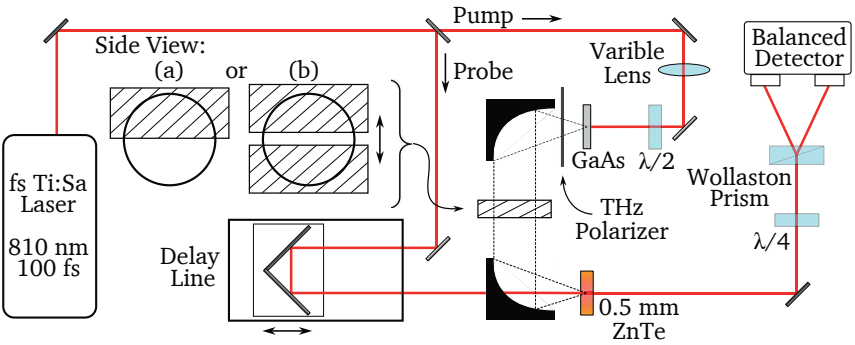

Figure 4.5 The measurement scheme is based on a standard electro-optic sampling setup. The polarization of the pump beam is adjusted using a $\lambda/2$ plate. Via a variable lens the laser pulses are focused onto the GaAs sample, allowing for different focus-spot sizes. The emitted THz radiation is polarization-filtered using a THz polarizer and focused on the 0.5 mm-thick ZnTe detector crystal via 90°-off-axis parabolic mirrors (OPM). Between the OPMs, polypropylene or metal sheets may be inserted, either (a) covering half the OPM cross section or (b) acting as a movable slit.

ple, a $1/e^2$-diameter of the excitation spot ranging from approximately 125 μm to 400 μm can be adjusted. The average excitation power may be varied within a range between 100 mW to 280 mW. The pump-pulse polarization is controlled by adjusting a $\lambda/2$-plate. It should be emphasized that the polarization can also be rapidly modified by all-electronic (i.e., non-mechanical) means by utilizing, e.g., an electro-optic modulator. The THz emission of the GaAs is guided towards the ZnTe crystal (thickness 0.5 mm) using two 90° off-axis parabolic mirrors (OPM) with a focal length and a diameter of 76.2 mm. A THz polarizer placed between the sample and the first OPM ensures that only currents along a certain direction contribute to the measured THz signal. After passing a delay line allowing to control the temporal delay between THz and probe pulse, the probe beam is focused onto the ZnTe crystal. The phase modulation of the probe beam induced in the crystal is analyzed using a balanced detection scheme as introduced in figure 2.9.

For the subsequent investigation of the spatial distribution of the emitted THz radiation, the experimental setup is utilized in three different ways.

1. Using the setup as described so far, the OPM next to the GaAs collects the THz radiation emitted by the crystal in a solid angle of 53.1°. The full THz radiation collected by the first OPM is focused by the second OPM onto the ZnTe crystal used for the detection process.

2. As indicated by the inset (a) in figure 4.5, the spatial profile of the radiation between the OPMs may be distorted by covering half of the cross section with a delay medium made of 1.5 mm thick Polypropylene. This material provides a nearly constant refractive index of about $n_{\mathrm{PP}} = 1.5$ in the THz frequency range and a small absorption coefficient α_{PP} ranging from 1 cm^{-1} to 3 cm^{-1} [186]. Thus, the radiation propagating through the material is only slightly attenuated, but significantly delayed in time as compared to the radiation propagating entirely through air. A delay of about 2.5 ps results. Consequently, the sampling-based detection process yields two temporally separated signals. The undistorted part of the signal is measured first and the radiation propagating through the Polypropylene appears at a later temporal position.

3. The inset (b) of figure 4.5 sketches a second method to analyze the spatial distribution of the radiation between the OPMs. Fabricating a slit into either a Polypropylene or metal mask, only a small portion of the undistorted field between the OPMs is detected. Using Polypropylene with a thickness of 1.0 cm ensures that the delayed

parts of the signal do not contribute to the measurement process. Scanning the slit through the entire cross section of the OPMs, a spatially resolved emission profile is obtained. For a slit width of 7 mm which is significantly larger than the THz wavelength (approximately 150 μm), refraction effects induced by the slit may be neglected.

In the following, results obtained by these three measurement methods are presented. By this, first the existence of the THz steering mechanism is unambiguously demonstrated. In a subsequent step, a quantification of the steering effect and a deeper analysis of the underlying dependencies is performed.

4.3.2 Measurement Results

In figure 4.6 (a), the first 2.2 ps of a THz time trace obtained following method 1 (no delay medium between the OPMs) is shown. Here, the crystal orientation is chosen such that the y-axis is parallel to the detection geometry of the setup. The latter is given by the adjustment of the THz polarizer and the ZnTe crystal as well as the pump beam polarization. Here and in the following, the detection system is set up to be sensitive for radiation polarized perpendicular with respect to the optical table. As predicted by table 2.2 and equation (2.32), in this geometry the maximal signal is expected for a pump beam oriented at $\pm 45°$ with respect to the crystal's y-axis where both the $\sigma^{(2)}_{yxy}$ and $\sigma^{(2)}_{yyx}$ tensor elements are excited.

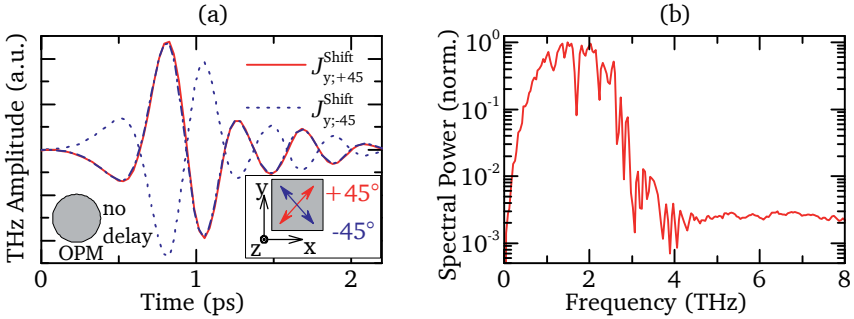

Figure 4.6 (a) THz field emitted by the shift current along the y-direction of the GaAs crystal, induced by $\pm 45°$ polarization of the pump light with respect to the y-axis. The dash-dotted line is the inverted trace of the $J^{Shift}_{y;-45}$-current, matching perfectly with $J^{Shift}_{y;+45}$. For these measurements, no delay medium is inserted between the OPM's. (b) Normalized spectral power of a 24-ps long time trace of the $J^{Shift}_{y;+45}$-current.

The straight and dotted lines in figure 4.6 (a) denote the corresponding measured THz signals, related to the induced currents $J^{\text{Shift}}_{y;+45}$ and $J^{\text{Shift}}_{y;-45}$ where the subscript denotes the axis of the current flow and the orientation of the pump light polarization. As can be seen, the signals are inverted to each other. This proves the inversion of the current flow direction from positive to negative y-direction upon a 90° rotation of the pump polarization. For clarity, the dash-dotted line represents the dotted signal $J^{\text{Shift}}_{y;-45}$ multiplied by (-1). It perfectly matches the signal attributed to the $J^{\text{Shift}}_{y;+45}$-current. In figure 4.6 (b), the normalized spectral power of the full time trace of 24 ps of the measured THz trace resulting from the $J^{\text{Shift}}_{y;+45}$-current is shown. As stated earlier, spectral components up to 4 THz are measured with the experimental setup.

In the second step, the Polypropylene delay medium is inserted between the OPMs such that the upper half is covered by the material. Again THz signals with vertical polarization are detected. Figure 4.7 shows the measurement results for four different orientations of the crystal axis and the pump polarization. As can be seen, in each measurement geometry the signal is split up into a non-delayed part (signal at a temporal position of about 0.8 ps) and a delayed part (temporal position of about 3.1 ps). This delay of about 2.3 ps corresponds to the expected effect induced by the Polypropylene sheet. In subframe (a), the experimental geometry is such that the x-axis of the crystal is parallel to the detection direction. The pump polarization is either parallel or orthogonal to the x-axis. Thus, according to table 2.2, either no shift current or the $J^{\text{Shift}}_{x;90}$-current linked to the $\sigma^{(2)}_{xyy}$ tensor element has been excited. This corresponds to the measurement results, showing either a very weak or a strong signal. Here, the weak signal is attributed to a current flow along the z-direction of the GaAs crystal, originating from the SF effect. This assumption is justified when analyzing the sign of both the delayed and non-delayed part of the signal. The trace shows an inverted behavior of both peaks, corresponding to the rotational symmetry of the field emitted by a dipole oriented along z. Without the Polypropylene-induced temporal delay, no signal is expected. This has been confirmed in additional measurements, i.e. using (110)-oriented GaAs without delay medium or utilizing different geometries, e.g. a (001)-cut GaAs crystal. With this observation it is demonstrated that the aperture angle of the OPM is sufficient to collect the radiation of such a current flow, which is a prerequisite to detect the steering mechanism as introduced in section 4.2. Analyzing the signal induced by the pump light polarization parallel to y, it is now clear that the measured trace in figure 4.7 (a) is the sum field of the shift current and the SF current. Indeed a slight deviation of the peak-to-peak values for the

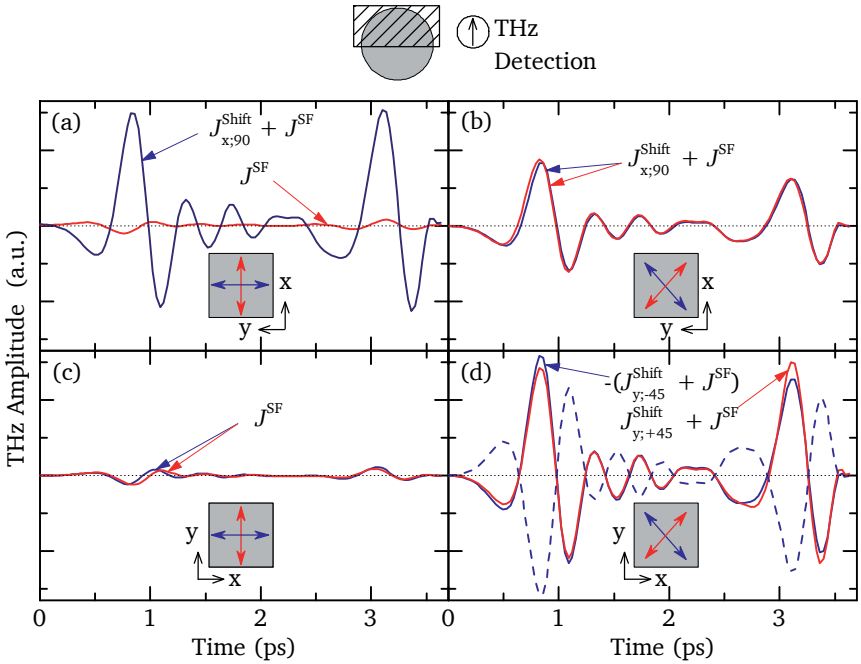

Figure 4.7 THz traces along the x and y-direction of the GaAs crystal (a,b and c,d, respectively) for pump light polarized either parallel or at $\pm 45°$ with respect to the crystal axis (a,c and b,d, respectively). One half of the OPM cross section is covered with a delay medium, retarding parts of the signal. The signal earlier in time is related to the uncovered half of the OPM, the later to the covered half. The y-axis of all figures are scaled equally.

delayed and non-delayed signal may be found, resulting from constructive and destructive interference of the fields. However, since the positioning of the delay material is crucial for the amplitude distribution between upper and lower half of the OPM cross section, this geometry is not suitable to analyze the interference effects in detail.

Proceeding to subframe (b), now the pump beam polarization is set to $\pm 45°$ with respect to the x-axis of the crystal. As a result, again the $J^{\mathrm{Shift}}_{x;90}$-current is excited. Due to the orientation of the light field, only a part of the electrical field of the pump pulse contributes to the current generation. Consequently, the detected signals show a reduced amplitude as compared to (a). The measurement traces for both excitation polarizations are identical within the measurement accuracy. This is expected, since the shift current strength and direction are similar for both polarizations, and, thus, the sum of shift and SF field is identical for both settings.

In subframe (c), the orientation is such that no net shift current flow due to the excitation of $\sigma^{(2)}$ is induced. Hence, only the SF current contribution is detected. As can be seen, the signal amplitudes do not depend on the polarization of the pump light.

In the last subframe (d), the THz steering mechanism is visible. Now the crystal is oriented such that the y-axis is parallel to the detection direction and the pump beam is polarized at an angle of $\pm 45^\circ$ with respect to y. By this, as already shown in figure 4.6, an inversion of the current flow direction is realized. However, this time the upper and lower half of the OPM cross section are analyzed individually due to the temporal delay induced by the Polypropylene. For one polarization of the pump beam, the emitted field of the SF current interferes with the shift current field destructively. Now changing the pump beam polarization, the shift current flow is inverted and the interference changes from destructive to constructive. This can nicely be seen in the measurement traces. For clarity, again one trace has been multiplied by (-1). Between the non-delayed and delayed part of the signal, a change in amplitude is visible when rotating the pump polarization. This effect cannot be attributed to a possibly improper alignment of the setup, but reflects optically controlled THz steering

4.3.3 Analysis of the Current Properties

To further analyze the fields emitted by shift and SF currents, the following two figures show the data of figure 4.7 in processed form. First, it is verified that the shift currents induced along the x and y-direction show an equal current strength, i.e. THz amplitude. This is predicted by the symmetry conditions of the shift current tensor $\sigma^{(2)}$, refer table 2.2. To analyze this, the contribution of the SF current J^{SF} is removed from the measurements shown in figure 4.7 by a simple subtraction of the waveforms,

$$(J_i^{\mathrm{Shift}} + J^{\mathrm{SF}}) - J^{\mathrm{SF}} = J_i^{\mathrm{Shift}}, \tag{4.2}$$

with $i = (x; 90), (y; +45), (y; -45)$. Here, J^{SF} as measured in the geometry of subframe (a) has also been used for the correction of the measurements shown in subframe (d). As can be seen in figure 4.8, the resulting corrected THz traces as emitted by the shift current alone show a high agreement with each other. Now the currents along y do not show significant differences anymore, highlighting that the steering mechanism as seen in figure 4.7 (d) indeed depends on the current contribution along the z-direction. A second conclusion may be drawn when comparing the temporal evolution of shift and SF currents. Using, e.g., the non-delayed parts of the corrected trace of $J_{x;90}^{\mathrm{Shift}}$ and the inverted trace of J^{SF}, fig-

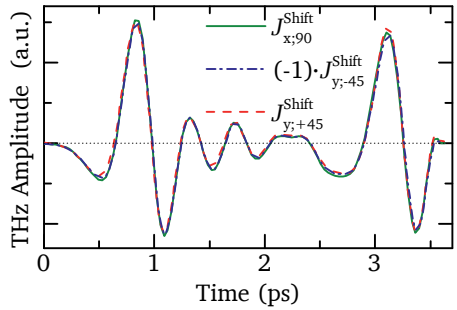

Figure 4.8 THz traces of the shift currents J^{Shift} shown in figure 4.7 (a) and (d), corrected for the influence of the SF current J^{SF}.

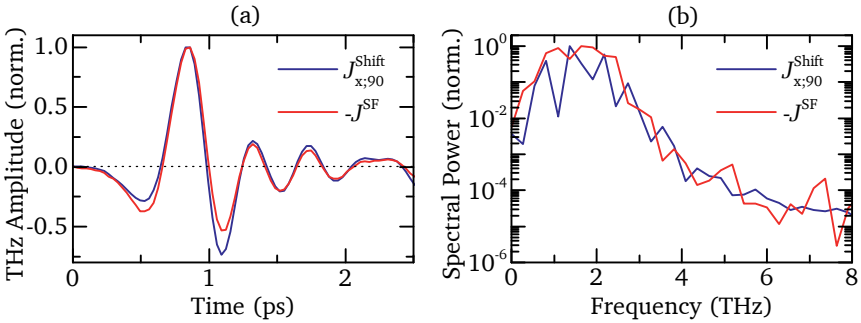

Figure 4.9 (a) Normalized THz traces of $J^{Shift}_{x;90}$ and -J^{SF}. (b) Spectral power of $J^{Shift}_{x;90}$ and -J^{SF} as obtained from 3.5 ps long time traces comparable to figure 4.7 (a).

ure 4.9 (a) proves that the temporal evolution of both currents is comparable. Normalizing both time traces to the maximum value, the extreme values of both signals coincide. Also regarding the frequency behavior, figure 4.9 (b), no significant difference in the power spectra may be recognized. Here, the Fourier transforms are obtained from the 3.6-ps long time traces, thus the frequency resolution is reduced as compared to figure 4.6. Hence at the given excitation density, the screening of the SF by the optically excited carriers takes place on a time scale comparable to the laser pulse duration.

With this analysis of the current properties, it is on the one hand confirmed that the measurement technique as described before yields consistent measurement results in line with the expected behavior of shift currents. On the other hand the fundamental assumption of an interference-based steering effect is validated. The spectral analysis of the signals related to SF and shift current reveals that both THz fields show a similar time- and frequency behavior. At least for the frequency range detectable

with the measurement setup as described before, no time or frequency dependencies of the steering mechanism are expected.

4.3.4 Spatial Profile of the Emission Pattern

So far, the steering effect has been verified using delay-based measurements. Such a measurement technique complicates a quantitative description, furthermore the results as shown in figure 4.7 (d) may lead to an underestimation of the effect due to the relatively small change in amplitude. To outline that the steering mechanism may be utilized for more than just academic purposes, the spatial distribution of the emitted THz field is analyzed using the movable slit between the OPMs. As trade-off between spatial resolution and signal strength, a slit width of 7 mm is chosen. Analyzing the peak-to-peak amplitude of the THz signal measured at the non-delayed temporal position, the spatial distribution of the radiation between the OPMs is obtained. The geometric properties were set similar to figure 4.7 (d). As depicted in figure 4.10, a pronounced shift of the maximal peak-to-peak amplitude is obtained for the different settings of the pump light polarization. According to the geometric properties of the OPMs, the measured shift of 10 mm equals an angular deviation of 8°. Comparable results are obtained, indifferent whether a metal or a Polypropylene mask has been utilized. A steering angle of 8° represents the maximum value achievable with the given setup with a pump power of 280 mW and a focus spot size of 123 µm. For lower pump power and larger spot sizes, e.g. a lower excitation density, the steering angle decreases as will be shown later. For a better understanding of the underlying

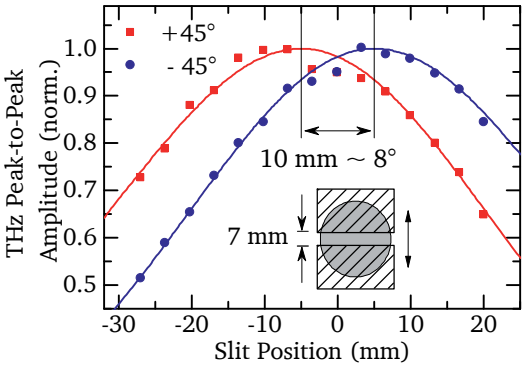

Figure 4.10 Normalized THz peak-to-peak amplitude of the currents induced by linearly polarized light at ±45° orientation with respect to the y-axis, measured at different positions of a 7 mm-wide slit. The excitation power is 280 mW, the focus spot size 123 μm. The straight lines are based on a simulation of the steering effect with parameters $p_1 = 1.72$ and $p_2 = 0.87$, explained in detail in section 4.4.

mechanisms, a simple model has been set up which allows for a simulation of the steering effect. A detailed description of the model is given in the next section. However, in figure 4.10 the calculated field distribution obtained from the simulation is already shown as straight lines, matching the measured data very well. The only significant deviations are found in the vicinity of 0 mm. The observed decrease of the peak-to-peak amplitude for both polarization directions is considered as an experimental artifact traced back to the drilled hole fabricated into the second OPM. As indicated in figure 4.5, the probe beam passes through the OPM to reach the ZnTe crystal. For this, a hole with a diameter of ≈ 2 mm has been drilled into the OPM. Consequently, the reflectivity of the corresponding part of the mirror is reduced as visible in figure 4.10.

4.4 Dipole Model

4.4.1 Fundamental Relations

The simulation of the THz steering effect is realized using a simple dipole-based model. Extending the schematic introduction used in section 4.2, this approach also allows for a precise description of the observed field pattern. As shown in figure 4.9, the temporal behavior of shift and SF currents may be assumed to be comparable, both performing in-phase dipole-like oscillations. To calculate the overall THz field emitted from each current contribution at an arbitrary position $\mathbf{r}$ in space, standard dipole radiation patterns in the far-field approximation are assumed [187],

$$\mathbf{E}_{\text{Dipole}} = \frac{1}{4\pi\epsilon_0}\frac{k^2 e^{ikr}}{r}(\hat{\mathbf{n}} \times \mathbf{p}_{\text{Shift,SF}}) \times \hat{\mathbf{n}}. \tag{4.3}$$

Here, ϵ_0 denotes the electric constant, k is the wave number, r is the distance from the dipole to the observation point, $\hat{\mathbf{n}}$ denotes the unit vector in direction to the observation point and $\mathbf{p}_{\text{Shift,SF}}$ represents the dipole moment of each current contribution, with $\mathbf{p}_{\text{Shift}}$ and $\mathbf{p}_{\text{SF}}$ being oriented along the y and z-direction, respectively. Again, the spherical coordinate system as introduced in figure 4.3 is used. The resulting magnitude of the individual field patterns for both dipoles at a fixed radial distance r is shown in figure 4.11 (a). Thereby, the upper and lower graph represents the field corresponding to the shift current dipole and SF dipole, respectively. The center point of the graphs at $\theta = 90°$ and $\phi = 0°$ denotes a point on the z-axis at distance r from the origin. Corresponding to the dipole orientation, the resulting field pattern of the shift dipole shows a rotational symmetry along ϕ and a sine behavior along θ. The SF dipole points along z, result-

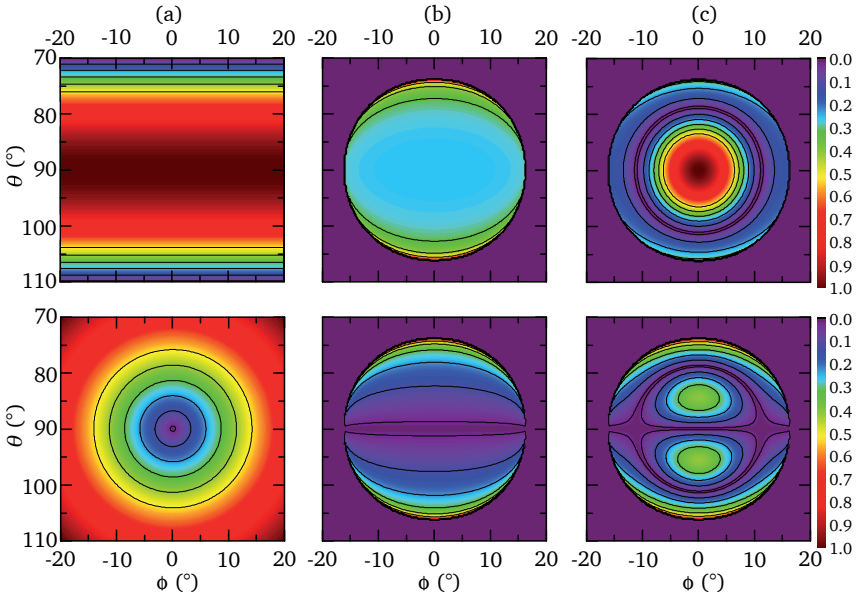

Figure 4.11 Simulated magnitude of the dipole field patterns for shift (upper) and SF (lower) current. In (a), the field at fixed radial distance is shown. (b) shows the field at the GaAs/air interface at distance r_i to the excitation spot. Refraction effects following the Fresnel formulas are included. Additionally the effect of the THz polarizer is accounted for, suppressing field components orthogonal to the θ-direction. In (c), Fraunhofer diffraction effects due to an excitation spot size comparable to the THz wavelength are regarded. The range of the color code of all graphs is set to [0,1].

ing in a cosine behavior along θ and a sine behavior along ϕ. This results in a rotational symmetry around the z-axis.

The THz radiation generated inside the GaAs crystal underlies several modifications until it is collected by the OPMs of the measurement setup. The most dominant contributions are given by refraction and diffraction effects. To reflect the polarization-dependent refraction occurring at the GaAs/air interface at distance r_i to the excitation spot, the model includes the Fresnel formulas to scale the emitted electrical field appropriately. Figure 4.11 (b) shows the resulting field patterns at the interface. With refractive indices of $n_{\mathrm{GaAs}} = 3.6$ and $n_{\mathrm{Air}} = 1$, only a fraction of the radiation exits the crystal. The largest part is totally reflected at the GaAs/air interface, with the critical angle given by Snell's law being $\arcsin(n_{\mathrm{Air}}/n_{\mathrm{GaAs}}) = 16.1°$. The increase of the field strength right before the critical angle along the θ-direction for both plots of part (b) is caused by the maximum transmittance of the radiation at the Brewster angle of

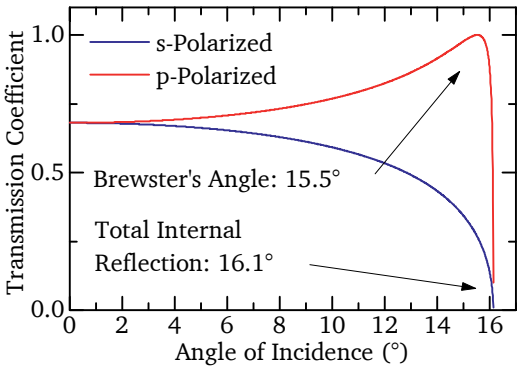

Figure 4.12 Transmission coefficients for light polarized parallel (p) and orthogonal (s) to the plane of incidence in GaAs (refractive index $n_{GaAs} = 3.6$).

$\arctan(n_{\text{Air}}/n_{\text{GaAs}}) = 15.5°$. For better comprehension, figure 4.12 shows the corresponding transmission coefficients for light polarized parallel (p) and orthogonal (s) to the plane of incidence in GaAs. In figure 4.11 (b) also the effect of the THz polarizer is included, suppressing field components orthogonal to the θ-direction.

The model also considers diffraction effects resulting from the size of the excitation spot diameter. Since the dimension of the spot is on the order of the center THz wavelength, the focal spot acts as a circular aperture and in the far field the well known Fraunhofer diffraction pattern results [188]. This leads to another scaling of the fields, where the intensity distribution is given by the Airy pattern,

$$I(\vartheta) = I_0 \left(\frac{2J_1(n_{\text{GaAs}}\, k\, a \sin\vartheta)}{n_{\text{GaAs}}\, k\, a \sin\vartheta} \right)^2 . \tag{4.4}$$

Here, ϑ is the angle between the position vector $\mathbf{r}$ and the z-axis, I_0 denotes the maximum intensity at the center position of the pattern, J_1 is the Bessel function of the first kind of order one, a is the radius of the aperture and $k = 2\pi/\lambda$ equals the wavenumber of the radiation with the free-space wavelength λ. In figure 4.11 (c), the resulting diffraction effects are visible. Focusing on the field emitted by the shift current dipole, the emission pattern shows the maximum of 0^{th} order centered at $(\theta, \phi) = (90°, 0°)$. The maximum is surrounded by the concentric minimum of 1^{st} order with a diameter depending on the ratio of the aperture diameter $d = 2a$ and the wavelength, d/λ. As a rule of thumb for the given experimental geometry, this restricts the main emission cone of the radiation inside the GaAs crystal to an angular region of $\pm 10°$ with respect to the z-axis. Following Snell's law, the emission cone outside the material covers angles between $\approx \pm 39°$. The diffraction pattern of the field emitted by the SF dipole shows

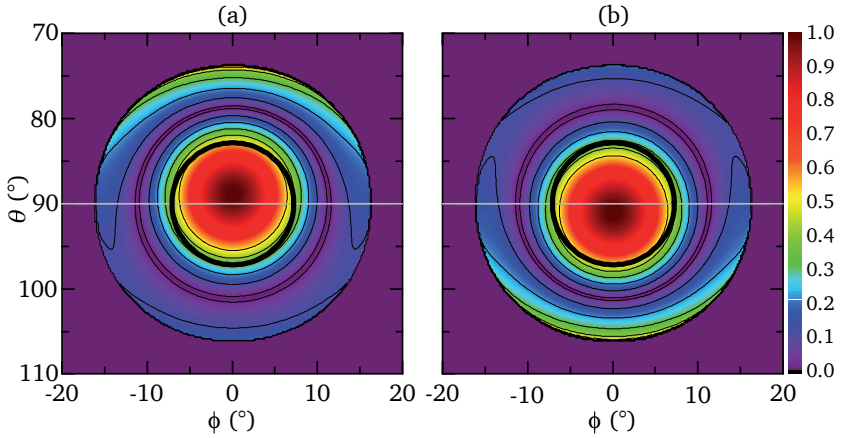

Figure 4.13 Simulated superposition of the electromagnetic fields emitted by the SF and shift current dipoles. Comparing (a) and (b), the orientation of the shift current dipole has been reversed. The bright lines denote the horizontal emission direction at $\theta = 90°$. The field emitted at angles inside the black circle is collected by the OPM with a numerical aperture of 0.45.

a more complex behavior. Here, two maxima are formed inside the region of the 1^{st} order minimum. Due to the initial rotational symmetry of the field, both maxima show an opposed orientation of the field vector.

Evaluating equation (4.3) for both dipoles and superimposing their electrical field vectors, the overall emission pattern is obtained. The resulting field distribution is shown in figure 4.13 for two orientations of the shift current dipole. As can be seen, the maximum of the 0^{th}-order emission cone is shifted by several degrees above or below the center line at $\theta = 90°$, represented as bright line. Reversing the dipole orientation along y results in an inversion of the shift angle. In addition, figure 4.13 shows the limited observation angle due to the numerical aperture (NA) of the OPM used in the setup. The NA of 0.45, corresponding to a solid angle of approximately $\pm 26.5°$, the majority of the field is collected. Nevertheless, since not the whole emission contributes to the measurement, a correction process is necessary to compensate the influence of the NA. Otherwise the steering effect would be underestimated in the measurements. The correction is done by evaluating a scaling factor for each slit position from the simulations and correct the measured peak-to-peak amplitude accordingly. Later in this section, this procedure is described in detail.

The slit-based measurement method of the emitted fields corresponds to an integration of the radiation patterns along ϕ. Thus, to compare sim-

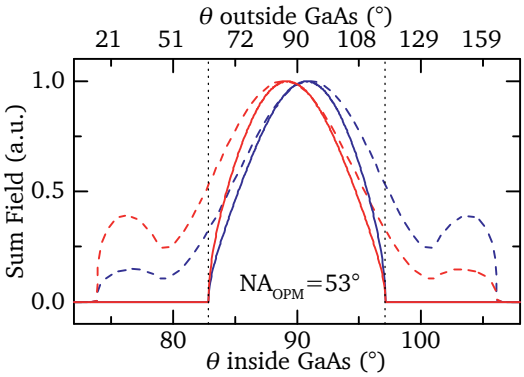

Figure 4.14 Integration along ϕ of the field distribution shown in figure 4.13. The blue and red traces correspond to subframes (a) and (b), respectively. The dashed lines represent an integration over the full emission patterns, the straight lines are limited to the area covered by the NA of the OPM.

ulation and measurement, the calculated field distributions are integrated as well, compare figure 4.14. Differentiating between an integration over the full emission patterns (dashed lines) and the part of the field collected by the OPM (straight lines), the asymmetry of the sum field along θ is clearly recognized. For better comprehension, the NA of the OPM is also depicted in the figure. The exact shape of the resulting field distribution now depends on the parameters used in the simulation. According to equations (4.3) and (4.4), the model is based on two parameters only.

i. The ratio between the strength of surface-field and shift current, denoted by the ratio of the absolute values of the dipole moments,

$$p_1 = \frac{|\mathbf{p}_{\mathrm{SF}}|}{|\mathbf{p}_{\mathrm{Shift}}|}. \tag{4.5}$$

ii. The influence of diffraction depending on the ratio between the center THz wavelength λ and excitation spot size d,

$$p_2 = \frac{d}{\lambda}. \tag{4.6}$$

The dipole model can now be used to approximate the measured data by an optimization of these parameters using a least-squares algorithm. This is performed utilizing the measured data and the simulation results which take into account the influence of the NA. To display the actual size of the steering effect, the influence of the NA is excluded from the measurement data in a subsequent step of data analysis. The ratio between the simulation results with and without considering the NA yields a scaling factor. Using this factor, the measured amplitude values at each slit position are corrected for the influence of the limited NA of the OPM. This is done

separately for each polarization setting. The obtained correction of the resulting steering angles is less than 10 % of the uncorrected values. All figures shown in sections 4.3 and 4.4 are based on the corrected data.

As already shown in figure 4.10, the model shows an excellent agreement to the experiment with the parameters set to $p_1 = 1.72$ and $p_2 = 0.87$. Thus, for the given excitation conditions with a pump power of $P = 280\,\mathrm{mW}$ and a focus spot size of $d = 123\,\mu\mathrm{m}$, the model predicts a relative strength of the SF current of 1.72 times the shift current. Moreover, with the given spot size, a central THz wavelength of $\lambda = 141\,\mu\mathrm{m}$, corresponding to a frequency of 2.1 THz, results. As commented on later, care has to be taken when interpreting the exact values. However, the order of magnitude coincides with the expectation and, thus, shows that the model is suitable for a general description of the observed steering mechanism as well as to obtain detailed information about physical dependencies.

Quadrupole Emission Before closing the description of the dipole model, one additional remark is given. So far, the modeling of the THz steering effect has been based on the assumption of a current flow along the z-direction and a corresponding dipole-like emission pattern. Alternatively, also a different current behavior can be used to explain the observed field distribution. As described in the theoretical fundamentals, refer figure 2.4, the photo-Dember effect results in an isotropic current flow in the half sphere inside the crystal around the focus spot of the laser. Thus, oppositely oriented current components along the positive and negative y-direction around the excitation spot may be found, forming an electrical quadrupole. Considering the limited detection angel resulting from the NA of the OPM, the corresponding quadrupole emission closely resembles the relative field pattern as obtained from a dipole oriented along z as obtained with the introduced measurement setup. However, the absolute field strength of such a quadrupole emission is significantly lower than compared to the field of a dipole of equal strength. Simulations utilizing this alternative approach have been performed. The results show that in order to allow for a comparable THz steering effect, a current strength is needed which is nearly two orders of magnitude higher than the one related to the dipole emitter. Consequently, since already the contribution of the PD current along z is negligible in intrinsic GaAs under the given excitation conditions, such quadrupole components can be excluded from the model.

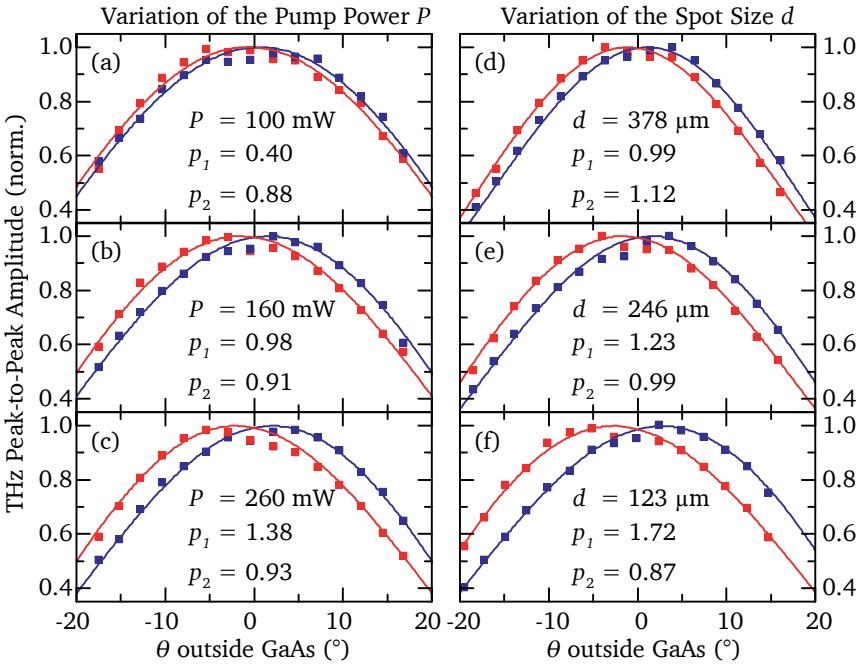

Figure 4.15 The variation of the experimental conditions results in a change of the steering angle. In (a) to (c) , the pump laser power P is varied. (d) to (f) correspond to different excitation spot sizes d. The straight lines represent the calculated field distributions using the dipole model with parameters p_1 and p_2 as given in the subframes.

4.4.2 Variation of Parameters

To obtain a better understanding of the contribution of shift and SF current to the overall emission pattern and to determine the influence of the diffraction effects, the model is utilized to extract the parameters p_1 and p_2 for different experimental conditions. Obvious experimental parameters to be investigated are the pump power P (affecting the individual current strengths) and the spot size d (affecting the diffraction properties). In figure 4.15, the measurement results obtained for different settings of theses parameters are shown. The subframes (a) to (c) correspond to an increase of the excitation power ranging from 100 mW to 260 mW at a fixed spot size of 180 µm (variation of the excitation intensity from 50 MW/cm^2 to 135 MW/cm^2). As can be seen, the modification of the pump power goes along with a significant change of the emitted field patterns. Regarding the steering angle, values of below 2° up to 6° are reached for minimum

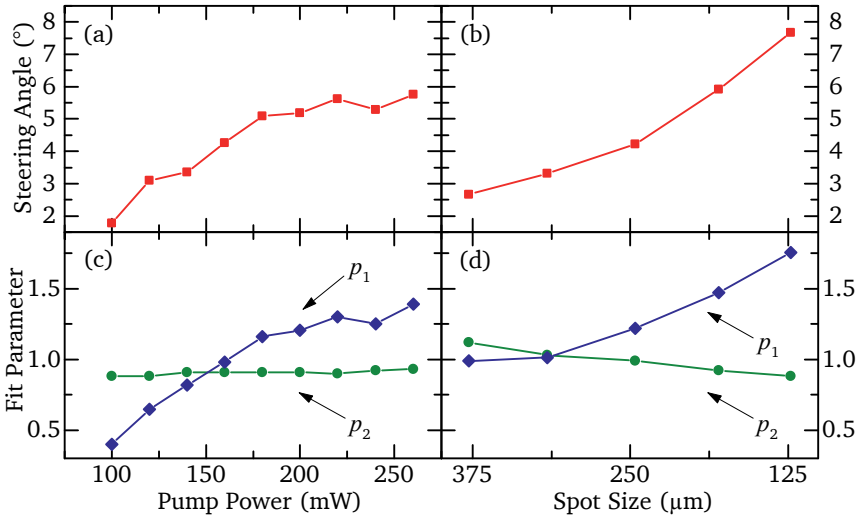

Figure 4.16 (a) Variation of the steering angle for modified pump power at a fixed excitation spot size of 180 μm and (b) modified spot size at a fixed pump power of 280 mW. Subframes (c) and (d) show the resulting values of the parameters p_1 and p_2 of the dipole model after least-square approximations of the experimental data.

to maximum power, respectively. According to the changed emission patterns, also the dipole model parameter p_1 and p_2 vary, resulting in an excellent agreement between simulation and experiment after the least-square approximation process. (This is not the case for measurement data in the vicinity of $\theta = 90°$. As already discussed, the reason for this lies in the experimental setup and, thus, these points are excluded from the least-square algorithm.) Subframes (d) to (f) show the corresponding change in the measurement data as well as in the model for a decrease of the spot size from 378 µm to 123 µm at an excitation power of 280 mW (variation of the excitation intensity from 33 MW/cm^2 to 310 MW/cm^2). This results in an even larger variation of the steering angle as compared to the power variation, ranging from 2.5° up to 8°. Again, the model nicely fits to the experimental results.

In figure 4.16, the variations of the measured steering angle and the corresponding parameters of the dipole model are shown in compact form. Here, (a) and (c) correspond to the pump power variation, (b) and (d) to the modified excitation spot size. In the upper frames, the experimentally observed steering angles are depicted. The lower frames show the corresponding fit parameter extracted from the model. A significant dependency between the steering angle and the model parameters can be

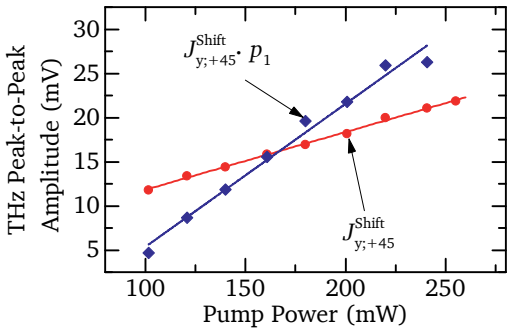

Figure 4.17 In red, the measured power dependency of the $J^{Shift}_{y,+45}$-current peak-to-peak THz amplitude is shown for an excitation spot size of 180 μm. The blue diamonds denote $p_1 \cdot J^{Shift}_{y,+45}$, corresponding to the strength of the surface field current J^{SF}.

seen. Regarding (c), it becomes clear that the rise in power results in a saturation behavior of p_1. This indicates a different power scaling of the involved shift and SF currents. For the shift current, it has been shown that a saturation of the corresponding THz peak-to-peak signal is to be expected [128,130]. To confirm this behavior, the peak-to-peak amplitude of the shift current $J^{\text{Shift}}_{y,+45}$ is measured for a pump power ranging from 100 mW to 280 mW at an excitation spot size of 180 µm (excitation intensity of 50 MW/cm^2 to 135 MW/cm^2 per pulse). The resulting power dependency is shown by the red bullets in figure 4.17. Due to the small variation of the excitation density, the sublinear behavior may not be extracted from the measurements, however the saturation is visible in the non-zero interception of a linear least-square approximation, indicated as red line in the figure. For the SF current, the power scaling is expected to be more complex. In the high-excitation regime, the current also saturates due to the shielding of the SF by the shifted charge carrier distribution. However, for the low-excitation regime, simulations predict a linear dependency of the THz-pulse amplitude on the excitation density [115]. For intermediate excitation powers as given here, an overall saturation smaller as compared to the shift current is expected. Due to the challenging measurement process, a convincing determination of the SF field amplitude dependency on the excitation power was not possible. Hence, the latter has to be extracted utilizing the model parameter p_1 and the measured amplitude behavior of the shift current $J^{\text{Shift}}_{y,+45}$. A multiplication of these values, $p_1 \cdot J^{\text{Shift}}_{y,+45}$, yields the power behavior of the THz amplitude of the SF current. The corresponding results are shown as blue diamonds in figure 4.17. Again utilizing a linear approximation of the data, a steeper slope than compared to the shift current is observed. This confirms that at the given excitation intensity, the saturation of the SF current is less dominant as compared to the shift current saturation.

Returning to figure 4.16, subframe (c) additionally shows that the variation of the steering angle due to a modification the pump power only slightly affects the diffraction properties expressed by p_2. This is in accordance with equations (4.4) and (4.6), where no power-dependency of p_2 is expected. A different behavior is noted in subframe (d), where both model parameters vary. Decreasing the excitation spot diameter for constant pump power goes along with an increasing power density and, consequently, p_1 increases as discussed before. Moreover, due to the change of the spot size, diffraction effects vary as well. This leads to a decrease of the fit parameter p_2 with decreasing spot size according to equation (4.6). In fact a sublinear dependence of p_2 on d is obtained, which may be attributed to wavelength-dependent diffraction, i.e., the center wavelength λ depends on d, too [180]. This assumption is confirmed by measurements of THz spectra, which show a stronger suppression of lower frequency components for smaller spot sizes, see figure 4.18. By this, the center wavelength of the THz field shifts to higher frequencies. Although this trend is clearly visible, the variation of the center frequency is significantly smaller than predicted by the sublinear course of p_2. Calculating the resulting THz frequencies using equation (4.6) with the parameters given in figure 4.15, only for 123 µm the calculated and the measured center wavelengths coincide. For larger spot diameters, the model predicts a more dominant shift of the frequency spectrum as can be seen by the dashed lines in figure 4.18 for spot sizes of 378 µm and 246 µm. This discrepancy is attributed to several reasons. First, an enlarged suppression of low-frequency components of the emitted radiation due to propagation and refraction effects reduce the spectral power at low frequencies. Second, also the detection process utilizing an OPM to focus the THz radiation results in a suppression of lower frequency components. Here, the wavelength-dependent size of the focal spot size inside the ZnTe reduces the detection efficiency for lower frequency components. Next to these known limitation of the detection setup, the simple dipole model may not be able to entirely cover the underlying dependencies. However, the fundamental agreement between the simulation and the measurements directly confirms the dipole model.

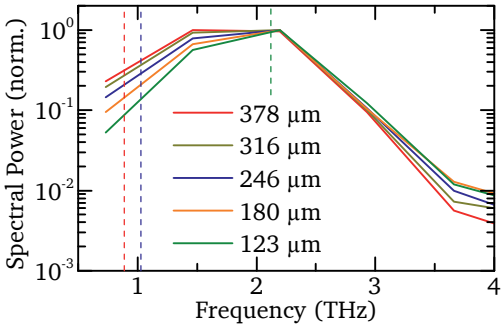

Figure 4.18 Normalized spectral power of the maximum THz field measured at different spot sizes. The dashed lines represent the center frequencies for spot sizes of 378 μm, 246 μm and 123 μm as predicted by the dipole model.

4.5 Summary and Outlook

The treatment of the THz steering effect as illustrated throughout chapter 4 shows that the control of all-optically induced currents provides a powerful mechanism for a fast and reliable spatial modification of electromagnetic fields at THz frequencies. The work as presented so far enables a deeper understanding of the fundamental effects contributing to the steering mechanism. Especially with the simple dipole model as introduced in section 4.4, details of the dependencies of the steering angle on the input parameters are revealed. The validity of the model is approved by comparisons between model predictions and experimental observations. With the reproduction of theoretically predicted power scaling of the THz amplitudes or the observation of the frequency shift of the emitted THz spectra, strong indications are given that the simple approach adequately describes the dominant contributions to the THz steering effect. With the introduced observations and relations, the topic of coherent control of steerable THz emitters is not conclusively dealt with. Several points immediately arise, calling for further research in this topic.

The main focus hereby may be given by an investigation regarding the improvement of the steering angle. To employ the steering mechanism for applications based on directed THz emission, angular deviations exceeding the hitherto reached values of about 8° are beneficial. Here, several approaches are apparent. For instance, as the simulations have shown, the steering angle may be greatly enlarged by reducing the large index-of-refraction mismatch between GaAs and air. In figure 4.19, the calculated field distribution without an index-of-refraction mismatch is shown. As can be seen, a steering angle of more than 16° is reached for identical excitation conditions as given in figure 4.10, i.e. $p_1 = 1.72$ and $p_2 = 0.87$. To reach a comparable result, a first approach is given by a modification of the spatial geometry of the semiconductor/air boundary. By attaching

a hemispherical lens with the focal position coinciding with the optical excitation spot, the radiation emitted by the point dipole will hit the matter/air interface under normal incidence. Thus, total internal reflection will not limit the emission cone. Here, easy-to-use lenses made of silicon which are commercially available, might be manufactured to exactly match the geometric requirements. Even if a difference in the refractive indices persists, the steering angle is expected to increase. However, care has to be taken in determining appropriate dimensions and exact position of the lens, such that the emitted THz radiation does not underlie focusing effects. This would complicate the interpretation of the resulting emission patterns and possibly even reduce the steering effect.

Following the basic idea of the simple dipole model, an obvious parameter affecting the effectiveness of the steering mechanism is given by the relative current strengths. Increasing the relative strength of the current flow along the z-direction will result in larger interference effects. This is expressed in the model calculations, yielding an increase of p_1 with increasing steering angle. To achieve a relative increase of the current along z, several possibilities exist. The most easy approach lies in a reduction of the shift current strength. This may be achieved by using an "unfavorable" pump light polarization with regard to the excitation of the $J^{\mathrm{Shift}}_{y;\pm 45}$-current. In figure 4.20, the resulting difference in the steering angle is shown for measurements with (a) an optimal polarization of $\pm 45°$-orientation with respect to the y-axis of the crystal and (b) a pump polarization at an angle of $\pm 15°$. The emission pattern greatly changes, revealing a significantly enlarged shift of the emission cones for both polarizations of the pump light. Although first measurements have been performed, resulting in an increase of the steering angle by more than a factor of two, additional experiments have to be performed to confirm this observation. However, the reduction of the shift current strength goes along with a reduction of the overall THz emission power of roughly a factor of 2 for the shown ex-

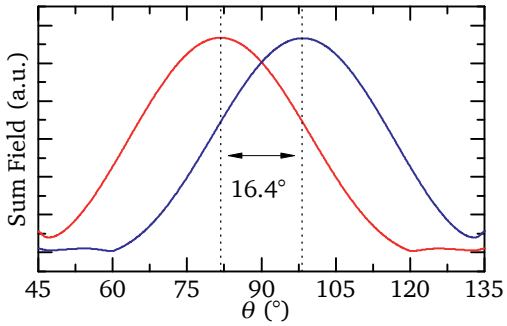

Figure 4.19 Steering effect as simulated without an index-of-refraction mismatch. A steering angle of 16.4° results.

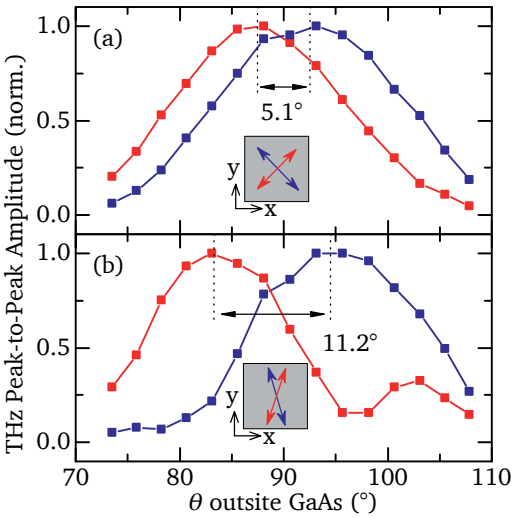

Figure 4.20 Normalized THz peak-to-peak amplitude of the interference pattern, induced with a different orientation of the linear polarization of the pump light. In (a), the polarization is oriented at ±45° to the y-axis of the crystal, in (b) at ±15°.

periment. Since already under optimal excitation conditions all-optically induced currents result in a comparably low THz emission as compared to other THz sources, this is not the best approach to realize enlarged THz steering angles. Instead, an increase of the SF current strength is favorable. Here, a tailoring of the semiconductor band structure may be feasible. Modifying the surface states, the band structure bending may be altered such that the resulting surface field strength increases. However, care has to be taken when scaling the relative strength of the current along z. If it is too strong, an effect as visible in the red trace of figure 4.20 (b) at a slit position of about $\theta = 103°$ occurs. Here, the SF current radiation overcompensates the shift current-related field, which results in the formation of a second maxima.

Another topic of interest for subsequent studies is the realization of a multi-directional steerable THz emitter. First experiments have been performed utilizing GaAs with a different orientation of the crystal axis system. A (113)-cut GaAs wafer allows for a steerable direction of the current flow along both $x = [1\bar{1}0]$ and $y = [33\bar{2}]$ direction. According to table 2.2 and with $\sigma^{(2)}_{xxy} = \sigma^{(2)}_{xyx}$ respectively $\sigma^{(2)}_{yxx} = -\sigma^{(2)}_{yyy}$, the THz steering mechanism occurs along the x and y-axis. First results are shown in figure 4.21, utilizing the delay-based measurement scheme. In (113)-cut GaAs, the linear pump polarization also induces significant current flows along the direction perpendicular to the main detection direction. These currents are also sensitive to the change of the polarization. Due to the non-perfect suppression of orthogonal field components by the THz polarizer, parts of

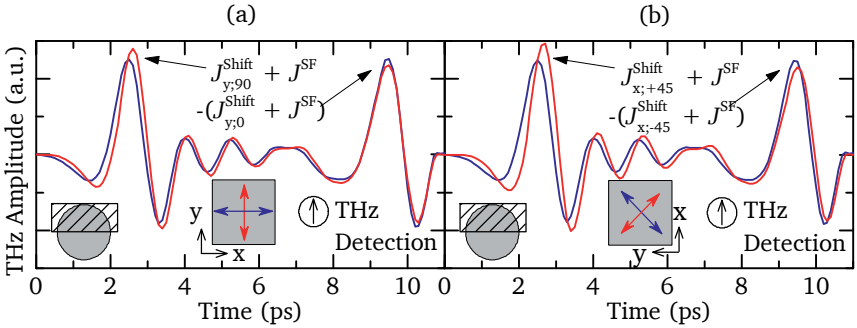

Figure 4.21 Steering effect along the x and y-direction of (113)-GaAs.

the related THz fields contribute to the measurement traces shown here. This explains the less symmetric behavior of the measurements as compared to the results obtained with (110)-cut GaAs (refer figure 4.7). Nevertheless, the steering effect along both directions is clearly visible, calling for future investigations.

Finally, an alternative detection method is proposed to investigate the spatial profile of the emitted THz radiation. In analogy to the spatially resolved detection scheme as presented in chapter 3, the radiation pattern of the optically induced currents can be analyzed by a relative movement of the source and the detection system. However, this is difficult using an electro-optic detection scheme based on OPMs due to the sensitive alignment properties of the mirrors. Without the use of focusing elements, the THz field strength is too weak to be adequately detected by the electro-optic effect. As an alternative, time-integrating detection systems such as Golay-cells, radiometers or pyroelectric detectors may be employed.

5 Conclusion

In the preceding chapters about THz frequency combs and the coherent control of steerable THz emitters individual summaries and outlooks have been stated with regard to the corresponding findings and further studies of interest. Here some general remarks about the work presented in this thesis are given.

THz technology offers an enormous potential to gain insights into fundamental physical effects as well as for the realization of applications in various fields of highest importance for modern society. Here, next to communication technology, also the market for imaging and sensing technologies, vital e.g. for medical diagnosis, quality control or security applications, showed a tremendous growth in the last years. THz sources and detectors greatly evolved over the last decade, offering various well-designed solutions for specific problems. From a technical point of view, the THz gap is about to be closed.

This thesis aims to contribute to this development. Regarding the viewpoint of NMIs like the Physikalisch-Technische Bundesanstalt, the chapter on THz frequency combs demonstrated how to adopt well-established metrological techniques and utilize them at the frontiers of today's physics. The transfer of the precision and accuracy of atomic clocks to higher frequencies utilizing optical frequency combs constitutes a very recent breakthrough of metrology. However, soon the concept of THz frequency combs followed and, as demonstrated here and by other groups, could be utilized for highest measurement accuracy in the THz frequency range. Moreover, a full characterization of the emission properties of THz sources was shown to be possible utilizing the demonstrated techniques. Still, in a metrological sense, the THz gap is not yet closed. A lot of work needs to be done: On the one hand this concerns a detailed analysis of the measurement parameter allowing to establish a detailed uncertainty budged. On the other hand, NMIs all over the world are called to compare their results to ensure for highest reliability and repeatability of the individual measurement techniques.

Concerning the topic of THz sources, an important demand given by THz applications operating in the field of, e.g., imaging, communication technology or sensing has been approached. It has been shown that the

concept of coherent control of steerable THz emitters allows for a reliable and fast modification of the THz emission direction. In contrast to mechanical or diffractive approaches, a predominantly frequency-independent and precisely adjustable THz emitter is given. Hence, a promising THz source has been introduced, ready to be adopted for technological needs. Yet there are additional parameters which are worth to be investigated. For instance also a well-controlled modification of the radiation frequency is desirable. Such a demand could also be approached on the basis of coherently controlled currents [189]. But also for cw-THz radiation comparable steering mechanisms are needed. Here, additional effort and research is necessary.

Thus also for future research the THz frequency range provides a rich and promising field of modern physics, allowing for plenty of interesting, astonishing an usefull findings.

A Electro-Optic Detection Crystals

According to equations (2.43) and (2.48), the signal strength obtained from the balanced detection scheme (refer figure 2.9) depends on the crystal material and geometry. Table A.1 summarizes the relevant quantities for the materials used or tested throughout this work. In (a), the corresponding values for the electro-optic coefficient r_{41} at a wavelength of about 800 nm are given. Additionally, the frequencies f_{res} of the lowest optical phonon resonances at 300 K are shown. In (b), the spectral amplitude of the THz beating signal (beat between the free-space signal with a frequency of $f_{\mathrm{THz}} = 100$ GHz and the optical frequency comb, refer equation (2.37)) are listed, obtained using different materials for the mixing process. These values compare the detection sensitivity of specific EO-detection crystals available for the work presented in the theses. The comparison does not intend to result in a general treatment of the EO-detection process as given in literature, refer subsection 2.3.2.

(a)

Material	r_{41} (pm/V)	f_{res} (THz)
ZnTe	3.9	5.4
GaP	1.0	10.96
GaSe	14.4	7.1
GaAs	1.1	8.02

(b)

Thickness (mm)	ZnTe (μV)	GaP (μV)	GaSe (μV)	GaAs (μV)
0.04	20			
0.08	30			
0.10	55			
0.20	100	–		
0.50	500	300		50
1.00	–		50	
2.00	45			
3.00	1100			

Table A.1 (a) Electro-optic coefficient r_{41} and the lowest optical phonon resonance at 300 K. The values have been taken from [60] and [190] and references therein. (b) Amplitude of the THz beating signal obtained with the 100 GHz source utilizing different detection crystals.

For all measurements, the detection signal was recorded using the balanced detection setup and the NI-5122 ADC at a sample rate of 100 megasamples/second over a measurement interval of 0.3 s. A noise amplitude of about 15 μV was obtained. For several crystals, no beating signal was found (indicated by the dashes) or the resulting signal strength was considerably less than expected. This is attributed to the individual quality and aging processes of the specific crystals that have been available. Moreover, since the crystals have been obtained from different manufacturers, a detailed comparison is difficult.

B Photoconductive Antenna Geometries

For the detection of a cw free-space electromagnetic signal, PCAs may be employed according to the description given in subsection 2.3.2. Following equation (2.36), the radiation induces a current flow of carriers excited by an optical pump pulse. The corresponding detection signal of the PCA yields spectral components attributed to the THz beating signal at a frequency of $f_{\mathrm{b,THz}}$ according to expression (2.37). The strength of this signal component depends on the current density between the contact electrodes of the PCA induced by the optical excitation. Hence, the geometric structure as well as the excitation density influence the measurement signal. To evaluate which structure and excitation condition yield the best results, different geometries have been tested. As signal source, a frequency multiplier operating at 100 GHz was used. The following treatment describes the measurement results obtained with the specific PCAs available for the work presented in the thesis. A general study and improvement of the PCA performance is not intended. Detailed investigations regarding a thorough comparison of different PCA structures are found in literature, e.g. [191–194].

The obtained spectral amplitude of the beating signal using dipole-shaped PCAs (refer figure 3.3) is shown in figure B.1. Different bow-tie geometries are compared, both fabricated on chip S31 (substrate P892-5). Either excitation gaps with a size of 20×20 $\mu\mathrm{m}^2$, subframe (a), or 6×6 $\mu\mathrm{m}^2$, subframe (b), were available on the chip. As can be seen, the larger excitation gap yields better results. However, due to the fragile construction of the PCA, this antenna was damaged during the experiments. Since also with the small gap sufficient signal-to-noise ratios were obtained, no additional antennas were fabricated. Thus for the measurements shown in chapter 3, the antenna with smaller excitation gap was employed.

The measured signal strength depends on the focal length of the excitation lens, hereby a 10 mm lens provides a slightly better signal as compared to a 15 mm lens. Smaller focus length could not be employed due to the experimental geometry. An even larger improvement of the signal am-

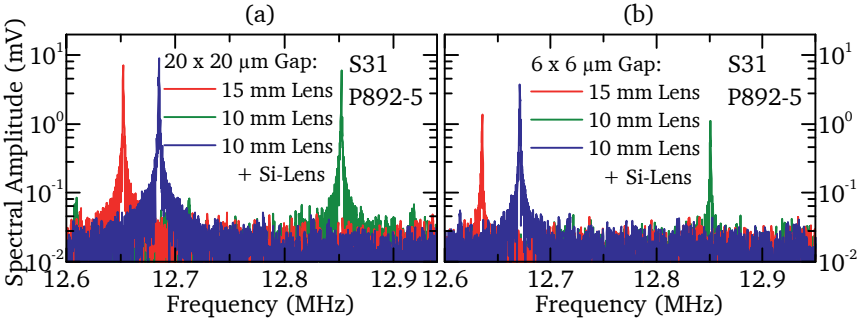

Figure B.1 Beating signal at a frequency of $f_{b,THz}$ using bow-tie-shaped antennas with a (a) 20 × 20 µm² or (b) 6 × 6 µm² excitation gap. A 100 GHz source is used as free-space signal. For the lens focusing the laser, two different focal lengths are compared. The maximum signal is obtained with a hemispherical lens with 0.5 cm diameter attached to the backside of the GaAs. Both antennas are part of chip S31, fabricated on the substrate P892-5.

plitude results when a hemisperical lens made of silicon is attached to the backside of the PCA. The lens mainly reduces the index-of-refraction mismatch between the GaAs sample and air, which reduces reflection of the electromagnetic radiation incident on the detector. Due to the large wavelength of the 100 GHz radiation as compared to the geometry of the lens and the excitation gap, no significant focusing effects occur. Next to the antennas fabricated on chip S31, a second chip with bow-tie-shaped PCAs has been used, internally labeled S30 (substrate P774-5). The geometric structure as well as the detection sensitivity of the chip is comparable to S31. This chip is employed for the measurement of the reference signal in section 3.3.

Additional to the bow-tie-shaped structures, dipole-formed antennas have been fabricated. Again using an LT-grown GaAs substrate (P1057), different antenna geometries are compared. Figure B.2 shows the measured beating signals utilizing a frequency multiplier operating at 34 GHz. The focus length of the excitation lens was 25 mm. The four subframes show the measurement results using different antenna geometries as described in the figure caption. The dipole antennas show a significantly reduced detection sensitivity as compared to the bow-tie-structure. This is attributed to the properties of the substrate and the changed experimental geometries necessary to incorporate the chip into the setup. Unfavorable electrical contacts and a reduced focal length of the excitation lens result in a reduced signal-to-noise ratio. Hence, the PCA-based experimental results shown throughout this work are obtained using the bow-tie structure.

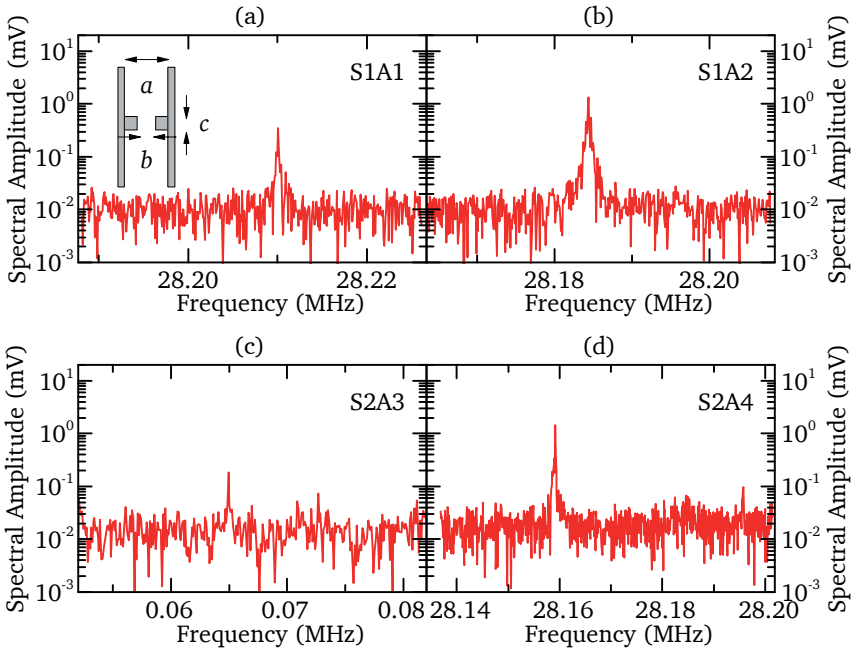

Figure B.2 Beating signal at a frequency of $f_{b,THz}$ using dipole-shaped antennas (see inset in subframe (a)) and an excitation lens with 25 mm focal length. The dipole parameters are (a) $a = 50\ \mu m$, $b = 12\ \mu m$, $c = 40\ \mu m$; (b) $a = 500\ \mu m$, $b = 25\ \mu m$, $c = 40\ \mu m$; (c) $a = 50\ \mu m$, $b = 25\ \mu m$, $c = 80\ \mu m$; (d) $a = 500\ \mu m$, $b = 50\ \mu m$, $c = 80\ \mu m$.

Bibliography

[1] A. Redo-Sanchez and X.-C. Zhang, "Terahertz Science and Technology Trends," *IEEE Journal of Selected Topics in Quantum Electronics*, vol. 14, no. 2, pp. 260–269, 2008.

[2] B. Ferguson and X.-C. Zhang, "Materials for terahertz science and technology.," *Nature materials*, vol. 1, no. 1, pp. 26–33, 2002.

[3] M. Tonouchi, "Cutting-edge terahertz technology," *Nature Photonics*, vol. 1, no. 2, pp. 97–105, 2007.

[4] P. H. Siegel, "Terahertz technology," *IEEE Transactions on Microwave Theory and Techniques*, vol. 50, no. 3, pp. 910–928, 2002.

[5] D. M. Mittleman, *Sensing with THz radiation*. Heidelberg: Springer, 2003.

[6] P. U. Jepsen, D. G. Cooke, and M. Koch, "Terahertz spectroscopy and imaging - Modern techniques and applications," *Laser & Photonics Reviews*, vol. 5, no. 1, pp. 124–166, 2011.

[7] J. El Haddad, B. Bousquet, L. Canioni, and P. Mounaix, "Review in terahertz spectral analysis," *Trends in Analytical Chemistry*, vol. 44, pp. 98–105, 2013.

[8] H. Eisele, A. Rydberg, and G. I. Haddad, "Recent advances in the performance of InP Gunn devices and GaAs TUNNETT diodes for the 100-300-GHz frequency range and above," *IEEE Transactions on Microwave Theory and Techniques*, vol. 48, no. 4, pp. 626–631, 2000.

[9] N. Kumar, U. Singh, T. P. Singh, and A. K. Sinha, "A Review on the Applications of High Power, High Frequency Microwave Source: Gyrotron," *Journal of Fusion Energy*, vol. 30, no. 4, pp. 257–276, 2011.

[10] G. R. Neil, "Accelerator Sources for THz Science: A Review," *Journal of Infrared, Millimeter, and Terahertz Waves*, 2013.

[11] G. Dodel, "On the history of far-infrared (FIR) gas lasers: Thirty-five years of research and application," *Infrared Physics & Technology*, vol. 40, no. 3, pp. 127–139, 1999.

[12] W. J. Witteman, *The CO2 Laser*. Berlin: Springer, 1987.

[13] D. Deacon, L. Elias, J. Madey, G. Ramian, H. Schwettman, and T. Smith, "First Operation of a Free-Electron Laser," *Physical Review Letters*, vol. 38, no. 16, pp. 892–894, 1977.

[14] C. W. Roberson and P. Sprangle, "A review of free-electron lasers," *Physics of Fluids B: Plasma Physics*, vol. 1, no. 1, p. 3, 1989.

[15] S. Barbieri, J. Alton, H. E. Beere, J. Fowler, E. H. Linfield, and D. A. Ritchie, "2.9 THz quantum cascade lasers operating up to 70 K in continuous wave," *Applied Physics Letters*, vol. 85, no. 10, p. 1674, 2004.

[16] B. S. Williams, "Terahertz quantum-cascade lasers," *Nature Photonics*, vol. 1, no. 9, pp. 517–525, 2007.

[17] G. P. Gallerano and S. Biedron, "Overview of Terahertz Radiation Sources," in *Proceedings of the 2004 FEL Conference* (R. Bakker, L. Giannessi, M. Marsi, and R. Walker, eds.), pp. 216–221, Comitato Conferenze Elettra, 2004.

[18] D. Grischkowsky, S. Keiding, M. Van Exter, and C. Fattinger, "Far-infrared time-domain spectroscopy with terahertz beams of dielectrics and semiconductors," *Journal of the Optical Society of America B*, vol. 7, no. 10, p. 2006, 1990.

[19] A. Nahata, A. S. Weling, and T. F. Heinz, "A wideband coherent terahertz spectroscopy system using optical rectification and electro-optic sampling," *Applied Physics Letters*, vol. 69, no. 16, p. 2321, 1996.

[20] J. Federici and L. Moeller, "Review of terahertz and subterahertz wireless communications," *Journal of Applied Physics*, vol. 107, no. 11, p. 111101, 2010.

[21] H.-J. Song and T. Nagatsuma, "Present and Future of Terahertz Communications," *IEEE Transactions on Terahertz Science and Technology*, vol. 1, no. 1, pp. 256–263, 2011.

[22] T. Kleine-Ostmann and T. Nagatsuma, "A Review on Terahertz Communications Research," *Journal of Infrared, Millimeter, and Terahertz Waves*, vol. 32, no. 2, pp. 143–171, 2011.

[23] J.-W. Shi, C.-B. Huang, and C.-L. Pan, "Millimeter-wave photonic wireless links for very high data rate communication," *NPG Asia Materials*, vol. 3, no. 4, pp. 41–48, 2011.

[24] C. Jastrow, S. Priebe, B. Spitschan, J. Hartmann, M. Jacob, T. Kürner, T. Schrader, and T. Kleine-Ostmann, "Wireless digital data transmission at 300 GHz," *Electronics Letters*, vol. 46, no. 9, p. 661, 2010.

[25] A. Hirata, H. Takahashi, N. Kukutsu, Y. Kado, H. Ikegawa, H. Nishikawa, T. Nakayama, and T. Inada, "Transmission trial of television broadcast materials using 120-GHz-band wireless link," *NTT Technical Review*, vol. 7, no. 3, 2009.

[26] E. Seok, D. Shim, C. Mao, R. Han, S. Sankaran, C. Cao, W. Knap, and K. K. O, "Progress and Challenges Towards Terahertz CMOS Integrated Circuits," *IEEE Journal of Solid-State Circuits*, vol. 45, no. 8, pp. 1554–1564, 2010.

[27] T. W. Crowe, W. L. Bishop, D. W. Porterfield, J. L. Hesler, and R. M. Weikle, "Opening the terahertz window with integrated diode circuits," *IEEE Journal of Solid-State Circuits*, vol. 40, no. 10, pp. 2104–2110, 2005.

[28] H.-W. Hübers, "Terahertz technology: Towards THz integrated photonics," *Nature Photonics*, vol. 4, no. 8, pp. 503–504, 2010.

[29] C. M. Armstrong, "Opportunities and challenges of working in the THz region of the electromagnetic spectrum: A critical analysis of applications and sources," in *2010 Abstracts IEEE International Conference on Plasma Science*, pp. 1–1, IEEE, 2010.

[30] N. Horiuchi, "Terahertz technology: Endless applications," *Nature Photonics*, vol. 4, no. 3, pp. 140–140, 2010.

[31] A. J. L. Adam, "Review of Near-Field Terahertz Measurement Methods and Their Applications," *Journal of Infrared, Millimeter, and Terahertz Waves*, vol. 32, no. 8-9, pp. 976–1019, 2011.

[32] G. P. Gallerano, "THz radiation and its applications: A review of events and a glance to the future," in *2013 6th UK, Europe, China Millimeter Waves and THz Technology Workshop (UCMMT)*, pp. 1–1, IEEE, 2013.

[33] A. Redo-Sanchez, N. Laman, B. Schulkin, and T. Tongue, "Review of Terahertz Technology Readiness Assessment and Applications," *Journal of Infrared, Millimeter, and Terahertz Waves*, vol. 34, no. 9, pp. 500–518, 2013.

[34] T. Kleine-Ostmann, T. Schrader, M. Bieler, U. Siegner, C. Monte, B. Gutschwager, J. Hollandt, A. Steiger, L. Werner, R. Müller, G. Ulm, I. Pupeza, and M. Koch, "THz Metrology," *Frequenz*, vol. 62, no. 5-6, pp. 137–148, 2008.

[35] M. Naftaly, R. A. Dudley, J. R. Fletcher, F. Bernard, C. Thomson, and Z. Tian, "Frequency calibration of terahertz time-domain spectrometers," *Journal of the Optical Society of America B*, vol. 26, no. 7, p. 1357, 2009.

[36] M. Naftaly, "Metrology Issues and Solutions in THz Time-Domain Spectroscopy: Noise, Errors, Calibration," *IEEE Sensors Journal*, vol. 13, no. 1, pp. 8–17, 2013.

[37] Y. Deng, Q. Sun, and J. Yu, "On-line calibration for linear time-base error correction of terahertz spectrometers with echo pulses," *Metrologia*, vol. 51, no. 1, pp. 18–24, 2014.

[38] M. Naftaly and R. Dudley, "Linearity calibration of amplitude and power measurements in terahertz systems and detectors," *Optics Letters*, vol. 34, no. 5, p. 674, 2009.

[39] J. H. Lehman, B. Lee, and E. N. Grossman, "Far infrared thermal detectors for laser radiometry using a carbon nanotube array.," *Applied Optics*, vol. 50, no. 21, pp. 4099–104, 2011.

[40] J. H. Lehman, M. Dowell, N. B. Popovic, K. Betz, and E. Grossman, "Laser power-meter comparison at far-infrared wavelengths and terahertz frequencies," *Metrologia*, vol. 49, no. 4, pp. 583–587, 2012.

[41] A. Steiger, B. Gutschwager, M. Kehrt, C. Monte, R. Müller, and J. Hollandt, "Optical methods for power measurement of terahertz radiation," *Optics Express*, vol. 18, no. 21, p. 21804, 2010.

[42] A. Steiger, M. Kehrt, C. Monte, and R. Müller, "Traceable terahertz power measurement from 1 THz to 5 THz," *Optics Express*, vol. 21, no. 12, pp. 14466–14473, 2013.

[43] Y. Deng, Q. Sun, J. Yu, Y. Lin, and J. Wang, "Broadband high-absorbance coating for terahertz radiometry.," *Optics Express*, vol. 21, no. 5, pp. 5737–42, 2013.

[44] M. Bieler, M. Spitzer, G. Hein, U. Siegner, and E. O. Göbel, "Ultrafast optics establishes metrological standards in high-frequency electronics," *Applied Physics A: Materials Science & Processing*, vol. 78, no. 4, pp. 429–433, 2004.

[45] M. Bieler, M. Spitzer, G. Hein, U. Siegner, F. Schnieder, T. Tischler, and W. Heinrich, "Broadband characterization of a microwave probe for picosecond electrical pulse measurements," *Measurement Science and Technology*, vol. 15, no. 9, pp. 1694–1701, 2004.

[46] T. S. Clement, P. D. Hale, S. Member, D. F. Williams, C. M. Wang, A. Dienstfrey, and D. A. Keenan, "Calibration of sampling oscilloscopes with high-speed photodiodes," *IEEE Transactions on Microwave Theory and Techniques*, vol. 54, no. 8, pp. 3173–3181, 2006.

[47] P. D. Hale, A. Dienstfrey, J. Wang, D. F. Williams, A. Lewandowski, D. A. Keenan, and T. S. Clement, "Traceable Waveform Calibration With a Covariance-Based Uncertainty Analysis," *IEEE Transactions on Instrumentation and Measurement*, vol. 58, no. 10, pp. 3554–3568, 2009.

[48] S. Priebe, C. Jastrow, M. Jacob, T. Kleine-Ostmann, T. Schrader, and T. Kürner, "Channel and Propagation Measurements at 300 GHz," *IEEE Transactions on Antennas and Propagation*, vol. 59, no. 5, pp. 1688–1698, 2011.

[49] J. A. DeSalvo, A. Hati, C. Nelson, and D. A. Howe, "Phase-Noise Measurement System for the Terahertz-Band," *IEEE Transactions on Terahertz Science and Technology*, vol. 2, no. 6, pp. 638–641, 2012.

[50] C. Dietlein, Z. Popovic, and E. N. Grossman, "Aqueous blackbody calibration source for millimeter-wave/terahertz metrology," *Applied Optics*, vol. 47, no. 30, p. 5604, 2008.

[51] R. Müller, A. Hoehl, A. Serdyukov, G. Ulm, J. Feikes, M. Ries, and G. Wüstefeld, "The Metrology Light Source of PTB - a Source for THz Radiation," *Journal of Infrared, Millimeter, and Terahertz Waves*, vol. 32, no. 6, pp. 742–753, 2011.

[52] J. F. Molloy, M. Naftaly, and R. A. Dudley, "Characterization of Terahertz Beam Profile and Propagation," *IEEE Journal of Selected Topics in Quantum Electronics*, vol. 19, no. 1, pp. 8401508–8401508, 2013.

[53] T. Yasui, Y. Kabetani, E. Saneyoshi, S. Yokoyama, and T. Araki, "Terahertz frequency comb by multifrequency-heterodyning photoconductive detection for high-accuracy, high-resolution terahertz spectroscopy," *Applied Physics Letters*, vol. 88, no. 24, p. 241104, 2006.

[54] S. Yokoyama, R. Nakamura, M. Nose, T. Araki, and T. Yasui, "Terahertz spectrum analyzer based on a terahertz frequency comb," *Optics Express*, vol. 16, no. 17, p. 13052, 2008.

[55] D.-S. Yee, Y. Jang, Y. Kim, and D.-C. Seo, "Terahertz spectrum analyzer based on frequency and power measurement.," *Optics Letters*, vol. 35, no. 15, pp. 2532–4, 2010.

[56] Y.-D. Hsieh, Y. Iyonaga, Y. Sakaguchi, S. Yokoyama, H. Inaba, K. Minoshima, F. Hindle, Y. Takahashi, M. Yoshimura, Y. Mori, T. Araki, and T. Yasui, "Terahertz Comb Spectroscopy Traceable to Microwave Frequency Standard," *IEEE Transactions on Terahertz Science and Technology*, vol. 3, no. 3, pp. 322–330, 2013.

[57] A. Steiger and Y. Deng, "Private communications: Project towards a comparison of PTB's and NIM's THz detectors," 2013.

[58] T. Yasui, R. Nakamura, K. Kawamoto, A. Ihara, Y. Fujimoto, S. Yokoyama, K. Minoshima, T. Nagatsuma, and T. Araki, "Real-time monitoring of continuous-wave terahertz radiation using a fiber-based, terahertz-comb-referenced spectrum analyzer.," *Optics Express*, vol. 17, no. 19, pp. 17034–43, 2009.

[59] C. Jansen, S. Wietzke, O. Peters, M. Scheller, N. Vieweg, M. Salhi, N. Krumbholz, C. Jördens, T. Hochrein, and M. Koch, "Terahertz imaging: applications and perspectives," *Applied Optics*, vol. 49, no. 19, pp. E48–57, 2010.

[60] A. Yariv, *Optical Electronics in Modern Communications*. New York: Oxford University Press, 5th ed., 1997.

[61] R. W. Boyd, *Nonlinear Optics*. San Diego: Academic Press, 2nd ed., 2003.

[62] H. Haug and S. W. Koch, *Quantum Theory of the Optical and Electronic Properties of Semiconductors*. Singapore: World Scientific Publishing, 4th ed., 2004.

[63] T. Meier, P. Thomas, and S. W. Koch, *Coherent Semiconductor Optics*. Berlin: Springer, 2007.

[64] M. Wegener, *Extreme Nonlinear Optics*. Berlin: Springer, 2005.

[65] C. Cohen-Tannoudji, B. Diu, and F. Laloe, *Quantum Mechanics*. New York: John Wiley & Sons, 1977.

[66] M. Bass, P. Franken, J. Ward, and G. Weinreich, "Optical Rectification," *Physical Review Letters*, vol. 9, no. 11, pp. 446–448, 1962.

[67] P. Franken, A. Hill, C. Peters, and G. Weinreich, "Generation of Optical Harmonics," *Physical Review Letters*, vol. 7, no. 4, pp. 118–119, 1961.

[68] M. Bass, P. Franken, A. Hill, C. Peters, and G. Weinreich, "Optical Mixing," *Physical Review Letters*, vol. 8, no. 1, pp. 18–18, 1962.

[69] J. Armstrong, N. Bloembergen, J. Ducuing, and P. Pershan, "Interactions between Light Waves in a Nonlinear Dielectric," *Physical Review*, vol. 127, no. 6, pp. 1918–1939, 1962.

[70] D. E. Aspnes, "Energy-band theory of the second-order nonlinear optical susceptibility of crystals of zinc-blende symmetry," *Physical Review B*, vol. 6, no. 12, 1972.

[71] J. E. Sipe and E. Ghahramani, "Nonlinear optical response of semiconductors in the independent-particle approximation," *Physical Review B*, vol. 48, no. 16, 1993.

[72] E. Ghahramani and J. E. Sipe, "Full band structure calculation of the linear electro-optic susceptibility," *Applied Physics Letters*, vol. 64, no. 18, p. 2421, 1994.

[73] J. L. P. Hughes and J. E. Sipe, "Calculation of second-order optical response in semiconductors.," *Physical Review B*, vol. 53, no. 16, pp. 10751–10763, 1996.

[74] C. Aversa and J. E. Sipe, "Nonlinear optical susceptibilities of semiconductors: Results with a length-gauge analysis," *Physical Review B*, vol. 52, no. 20, 1995.

[75] J. E. Sipe and A. Shkrebtii, "Second-order optical response in semiconductors," *Physical Review B*, vol. 61, no. 8, pp. 5337–5352, 2000.

[76] A. E. Siegman, *Lasers*. Sausalito: University Science Books, 1986.

[77] O. Svelto, *Principles of Lasers*. New York: Springer, 5th ed., 2010.

[78] A. Schawlow and C. Townes, "Infrared and Optical Masers," *Physical Review*, vol. 112, no. 6, pp. 1940–1949, 1958.

[79] T. H. Maiman, "Stimulated Optical Radiation in Ruby," *Nature*, vol. 187, no. 4736, pp. 493–494, 1960.

[80] W. Lamb, "Theory of an Optical Maser," *Physical Review*, vol. 134, no. 6A, pp. A1429–A1450, 1964.

[81] L. E. Hargrove, R. L. Fork, and M. A. Pollack, "Locking of He[Single Bond]Ne Laser Modes induced by Synchronous intracavity modulation," *Applied Physics Letters*, vol. 5, no. 1, p. 4, 1964.

[82] P. F. Moulton, "Spectroscopic and laser characteristics of Ti:Al_2O_3," *Journal of the Optical Society of America B*, vol. 3, no. 1, p. 125, 1986.

[83] D. E. Spence, J. M. Evans, W. E. Sleat, and W. Sibbett, "Regeneratively initiated self-mode-locked Ti:sapphire laser.," *Optics Letters*, vol. 16, no. 22, pp. 1762–4, 1991.

[84] T. Brabec, C. Spielmann, P. F. Curley, and F. Krausz, "Kerr lens mode locking," *Optics Letters*, vol. 17, no. 18, pp. 1292–4, 1992.

[85] D. H. Sutter, G. Steinmeyer, L. Gallmann, N. Matuschek, F. Morier-Genoud, U. Keller, V. Scheuer, G. Angelow, and T. Tschudi, "Semiconductor saturable-absorber mirror assisted Kerr-lens mode-locked Ti:sapphire laser producing pulses in the two-cycle regime," *Optics Letters*, vol. 24, no. 9, p. 631, 1999.

[86] U. Morgner, F. X. Kärtner, S. H. Cho, Y. Chen, H. A. Haus, J. G. Fujimoto, E. P. Ippen, V. Scheuer, G. Angelow, and T. Tschudi, "Sub-two-cycle pulses from a Kerr-lens mode-locked Ti:sapphire laser," *Optics Letters*, vol. 24, no. 6, p. 411, 1999.

[87] R. Ell, U. Morgner, F. X. Kärtner, J. G. Fujimoto, E. P. Ippen, V. Scheuer, G. Angelow, T. Tschudi, M. J. Lederer, A. Boiko, and B. Luther-Davies, "Generation of 5-fs pulses and octave-spanning spectra directly from a Ti:sapphire laser," *Optics Letters*, vol. 26, no. 6, p. 373, 2001.

[88] J. Reichert, R. Holzwarth, T. Udem, and T. W. Hänsch, "Measuring the frequency of light with mode-locked lasers," *Optics Communications*, vol. 172, pp. 59–68, 1999.

[89] T. Udem, R. Holzwarth, and T. W. Hänsch, "Optical frequency metrology.," *Nature*, vol. 416, no. 6877, pp. 233–237, 2002.

[90] S. T. Cundiff and J. Ye, "Colloquium: Femtosecond optical frequency combs," *Reviews of Modern Physics*, vol. 75, no. 1, pp. 325–342, 2003.

[91] S. A. Diddams, "The evolving optical frequency comb," *Journal of the Optical Society of America B*, vol. 27, no. 11, 2010.

[92] T. Udem, *Die Messung der Frequenz von Licht mit modengekoppelten Lasern*, vol. 293. Garching: Max-Planck-Institut für Quantenoptik, 2004.

[93] R. Paschotta, H. R. Telle, and U. Keller, "Noise of Solid-State Lasers," in *Solid-State Lasers and Applications* (A. Sennaroglu, ed.), Optical Science and Engineering, ch. 12, pp. 473–510, Boca Raton: CRC Press, 2006.

[94] C. Caves, "Quantum limits on noise in linear amplifiers," *Physical Review D*, vol. 26, no. 8, pp. 1817–1839, 1982.

[95] D. Linde, "Characterization of the noise in continuously operating mode-locked lasers," *Applied Physics B*, vol. 39, no. 4, pp. 201–217, 1986.

[96] H. A. Haus and A. Mecozzi, "Noise of mode-locked lasers," *IEEE Journal of Quantum Electronics*, vol. 29, no. 3, pp. 983–996, 1993.

[97] R. Paschotta, "Noise of mode-locked lasers (Part I): numerical model," *Applied Physics B*, vol. 79, no. 2, pp. 153–162, 2004.

[98] R. Paschotta, "Noise of mode-locked lasers (Part II): timing jitter and other fluctuations," *Applied Physics B*, vol. 79, no. 2, pp. 163–173, 2004.

[99] C. R. Menyuk, J. K. Wahlstrand, J. Willits, R. P. Smith, T. R. Schibli, and S. T. Cundiff, "Pulse dynamics in mode-locked lasers: relaxation oscillations and frequency pulling.," *Optics Express*, vol. 15, no. 11, pp. 6677–89, 2007.

[100] F. X. Kärtner, *Few-cycle-pulse generation and its applications*. Berlin: Springer, 2004.

[101] J. K. Wahlstrand, J. T. Willits, C. R. Menyuk, and S. T. Cundiff, "The quantum-limited comb lineshape of a mode-locked laser: fundamental limits on frequency uncertainty.," *Optics Express*, vol. 16, no. 23, pp. 18624–30, 2008.

[102] M. J. Ablowitz, B. Ilan, and S. T. Cundiff, "Noise-induced linewidth in frequency combs.," *Optics Letters*, vol. 31, no. 12, pp. 1875–7, 2006.

[103] E. N. Ivanov, S. A. Diddams, and L. Hollberg, "Analysis of noise mechanisms limiting the frequency stability of microwave signals generated with a femtosecond laser," *IEEE Journal of Selected Topics in Quantum Electronics*, vol. 9, no. 4, pp. 1059–1065, 2003.

[104] D. R. Walker, D. W. Crust, W. E. Sleat, and W. Sibbett, "Reduction of phase noise in passively mode-locked lasers," *IEEE Journal of Quantum Electronics*, vol. 28, no. 1, pp. 289–296, 1992.

[105] D. E. Spence, J. M. Dudley, K. Lamb, W. E. Sleat, and W. Sibbett, "Nearly quantum-limited timing jitter in a self-mode-locked Ti:sapphire laser.," *Optics Letters*, vol. 19, no. 7, pp. 481–3, 1994.

[106] H. Dember, "Über eine photoelektromotorische Kraft in Kupferoxydul-Kristallen," *Physikalische Zeitschrift*, vol. 32, pp. 554–556, 1931.

[107] H. Dember, "Über eine Kristallphotozelle," *Physikalische Zeitschrift*, vol. 32, p. 856, 1931.

[108] H. Dember, "Über die Vorwärtsbewegung von Elektronen durch Licht.," *Physikalische Zeitschrift*, vol. 33, pp. 207–208, 1932.

[109] E. Yablonovitch, B. J. Skromme, R. Bhat, J. P. Harbison, and T. J. Gmitter, "Band bending, Fermi level pinning, and surface fixed charge on chemically prepared GaAs surfaces," *Applied Physics Letters*, vol. 54, no. 6, p. 555, 1989.

[110] X.-C. Zhang, B. B. Hu, J. T. Darrow, and D. H. Auston, "Generation of femtosecond electromagnetic pulses from semiconductor surfaces," *Applied Physics Letters*, vol. 56, no. 11, p. 1011, 1990.

[111] X.-C. Zhang and D. H. Auston, "Optoelectronic measurement of semiconductor surfaces and interfaces with femtosecond optics," *Journal of Applied Physics*, vol. 71, no. 1, p. 326, 1992.

[112] T. Dekorsy, T. Pfeifer, W. Kütt, and H. Kurz, "Subpicosecond carrier transport in GaAs surface-space-charge fields.," *Physical Review B*, vol. 47, no. 7, pp. 3842–3849, 1993.

[113] T. Held, T. Kuhn, and G. Mahler, "Influence of internal electric fields and surface charges on the transport of an optically generated electron-hole plasma," *Physical Review B*, vol. 44, no. 23, pp. 12873–12879, 1991.

[114] A. Kuznetsov and C. Stanton, "Ultrafast optical generation of carriers in a dc electric field: Transient localization and photocurrent," *Physical Review B*, vol. 48, no. 15, pp. 10828–10845, 1993.

[115] V. L. Malevich, "Monte Carlo simulation of THz-pulse generation from semiconductor surface," *Semiconductor Science and Technology*, vol. 17, no. 6, pp. 551–556, 2002.

[116] M. B. Johnston, D. Whittaker, A. Corchia, A. Davies, and E. H. Linfield, "Simulation of terahertz generation at semiconductor surfaces," *Physical Review B*, vol. 65, no. 16, p. 165301, 2002.

[117] S. M. Sze, *Physics of Semiconductor Devices*. John Wiley & Sons, 2nd ed., 1982.

[118] J. N. Heyman, N. Coates, A. Reinhardt, and G. Strasser, "Diffusion and drift in terahertz emission at GaAs surfaces," *Applied Physics Letters*, vol. 83, no. 26, p. 5476, 2003.

[119] M. Nakajima, Y. Oda, and T. Suemoto, "Competing terahertz radiation mechanisms in semi-insulating InP at high-density excitation," *Applied Physics Letters*, vol. 85, no. 14, p. 2694, 2004.

[120] X.-C. Zhang, J. T. Darrow, B. B. Hu, D. H. Auston, M. T. Schmidt, P. Tham, and E. S. Yang, "Optically induced electromagnetic radiation from semiconductor surfaces," *Applied Physics Letters*, vol. 56, no. 22, p. 2228, 1990.

[121] X.-C. Zhang and D. H. Auston, "Generation of steerable submillimeter waves from semiconductor surfaces by spatial light modulators," *Applied Physics Letters*, vol. 59, no. 7, p. 768, 1991.

[122] K. Liu, J. Xu, T. Yuan, and X.-C. Zhang, "Terahertz radiation from InAs induced by carrier diffusion and drift," *Physical Review B*, vol. 73, no. 15, pp. 1–6, 2006.

[123] A. Kuznetsov and C. Stanton, "Coherent phonon oscillations in GaAs," *Physical Review B*, vol. 51, no. 12, pp. 7555–7565, 1995.

[124] T. Dekorsy, H. Auer, H. J. Bakker, H. G. Roskos, and H. Kurz, "THz electromagnetic emission by coherent infrared-active phonons.," *Physical Review B*, vol. 53, no. 7, pp. 4005–4014, 1996.

[125] R. Kersting, K. Unterrainer, G. Strasser, H. Kauffmann, and E. Gornik, "Few-Cycle THz Emission from Cold Plasma Oscillations," *Physical Review Letters*, vol. 79, no. 16, pp. 3038–3041, 1997.

[126] R. Kersting, J. Heyman, G. Strasser, and K. Unterrainer, "Coherent plasmons in n-doped GaAs," *Physical Review B*, vol. 58, no. 8, pp. 4553–4559, 1998.

[127] A. Reklaitis, "Terahertz emission from InAs induced by photo-Dember effect: Hydrodynamic analysis and Monte Carlo simulations," *Journal of Applied Physics*, vol. 108, no. 5, p. 053102, 2010.

[128] D. Côté, N. Laman, and H. M. van Driel, "Rectification and shift currents in GaAs," *Applied Physics Letters*, vol. 80, no. 6, p. 905, 2002.

[129] F. Nastos and J. E. Sipe, "Optical rectification and shift currents in GaAs and GaP response: Below and above the band gap," *Physical Review B*, vol. 74, no. 3, p. 035201, 2006.

[130] M. Bieler, K. Pierz, and U. Siegner, "Simultaneous generation of shift and injection currents in (110)-grown GaAs/AlGaAs quantum wells," *Journal of Applied Physics*, vol. 100, no. 8, p. 083710, 2006.

[131] Z. Popovic and E. N. Grossman, "THz Metrology and Instrumentation," *IEEE Transactions on Terahertz Science and Technology*, vol. 1, no. 1, pp. 133–144, 2011.

[132] G. Mourou, "Picosecond microwave pulse generation," *Applied Physics Letters*, vol. 38, no. 6, p. 470, 1981.

[133] G. Mourou, "Picosecond microwave pulses generated with a subpicosecond laser-driven semiconductor switch," *Applied Physics Letters*, vol. 39, no. 4, p. 295, 1981.

[134] D. H. Auston, K. P. Cheung, and P. R. Smith, "Picosecond photoconducting Hertzian dipoles," *Applied Physics Letters*, vol. 45, no. 3, p. 284, 1984.

[135] P. R. Smith, D. H. Auston, and M. C. Nuss, "Subpicosecond photoconducting dipole antennas," *IEEE Journal of Quantum Electronics*, vol. 24, no. 2, pp. 255–260, 1988.

[136] G. Klatt, R. Gebs, C. Janke, T. Dekorsy, and A. Bartels, "Rapid-scanning terahertz precision spectrometer with more than 6 THz spectral coverage.," *Optics Express*, vol. 17, no. 25, pp. 22847–54, 2009.

[137] S. Kono, M. Tani, P. Gu, and K. Sakai, "Detection of up to 20 THz with a low-temperature-grown GaAs photoconductive antenna gated with 15 fs light pulses," *Applied Physics Letters*, vol. 77, no. 25, p. 4104, 2000.

[138] S. Kono, M. Tani, and K. Sakai, "Ultrabroadband photoconductive detection: Comparison with free-space electro-optic sampling," *Applied Physics Letters*, vol. 79, no. 7, p. 898, 2001.

[139] A. Hussain and S. R. Andrews, "Dynamic range of ultrabroadband terahertz detection using GaAs photoconductors," *Applied Physics Letters*, vol. 88, no. 14, p. 143514, 2006.

[140] S. Gupta, J. F. Whitaker, and G. A. Mourou, "Ultrafast carrier dynamics in III-V semiconductors grown by molecular-beam epitaxy at very low substrate temperatures," *IEEE Transactions on Quantum Electronics*, vol. 28, no. 10, 1992.

[141] J. T. Darrow, B. B. Hu, X.-C. Zhang, and D. H. Auston, "Subpicosecond electromagnetic pulses from large-aperture photoconducting antennas," *Optics Letters*, vol. 15, no. 6, p. 323, 1990.

[142] F. G. Sun, G. A. Wagoner, and X.-C. Zhang, "Measurement of free-space terahertz pulses via long-lifetime photoconductors," *Applied Physics Letters*, vol. 67, no. 12, p. 1656, 1995.

[143] M. Tani, S. Matsuura, K. Sakai, and S. Nakashima, "Emission characteristics of photoconductive antennas based on low-temperature-grown GaAs and semi-insulating GaAs.," *Applied Optics*, vol. 36, no. 30, pp. 7853–9, 1997.

[144] A. Haché, J. E. Sipe, and H. M. van Driel, "Quantum interference control of electrical currents in GaAs," *IEEE Journal of Quantum Electronics*, vol. 34, no. 7, pp. 1144–1154, 1998.

[145] M. Tani, K. Sakai, and H. Mimura, "Ultrafast photoconductive detectors based on semi-insulating GaAs and InP," *Japanese Journal of Applied Physics*, vol. 36, p. 1175, 1997.

[146] P. U. Jepsen, R. H. Jacobsen, and S. R. Keiding, "Generation and detection of terahertz pulses from biased semiconductor antennas," *Journal of the Optical Society of America B*, vol. 13, no. 11, p. 2424, 1996.

[147] J. A. Valdmanis, G. Mourou, and C. W. Gabel, "Picosecond electro-optic sampling system," *Applied Physics Letters*, vol. 41, no. 3, p. 211, 1982.

[148] J. A. Valdmanis and G. Mourou, "Subpicosecond electrooptic sampling: Principles and applications," *IEEE Journal of Quantum Electronics*, vol. 22, no. 1, pp. 69–78, 1986.

[149] Q. Wu and X.-C. Zhang, "Free-space electro-optic sampling of terahertz beams," *Applied Physics Letters*, vol. 67, no. 24, p. 3523, 1995.

[150] Q. Wu, M. Litz, and X.-C. Zhang, "Broadband detection capability of ZnTe electro-optic field detectors," *Applied Physics Letters*, vol. 68, no. 21, p. 2924, 1996.

[151] Q. Wu and X.-C. Zhang, "7 terahertz broadband GaP electro-optic sensor," *Applied Physics Letters*, vol. 70, no. 14, p. 1784, 1997.

[152] A. Leitenstorfer, S. Hunsche, J. Shah, M. C. Nuss, and W. H. Knox, "Detectors and sources for ultrabroadband electro-optic sampling: Experiment and theory," *Applied Physics Letters*, vol. 74, no. 11, p. 1516, 1999.

[153] G. Gallot and D. Grischkowsky, "Electro-optic detection of terahertz radiation," *Journal of the Optical Society of America B*, vol. 16, no. 8, p. 1204, 1999.

[154] G. Gallot, J. Zhang, R. W. McGowan, T.-I. Jeon, and D. Grischkowsky, "Measurements of the THz absorption and dispersion of ZnTe and their relevance to the electro-optic detection of THz radiation," *Applied Physics Letters*, vol. 74, no. 23, p. 3450, 1999.

[155] D. Côté, J. E. Sipe, and H. M. v. Driel, "Simple method for calculating the propagation of terahertz radiation in experimental geometries," *Journal of the Optical Society of America B*, vol. 20, no. 6, pp. 1374–1385, 2003.

[156] P. C. M. Planken, H.-K. Nienhuys, H. J. Bakker, and T. Wenckebach, "Measurement and calculation of the orientation dependence of terahertz pulse detection in ZnTe," *Journal of the Optical Society of America B*, vol. 18, no. 3, p. 313, 2001.

[157] N. C. J. van der Valk, T. Wenckebach, and P. C. M. Planken, "Full mathematical description of electro-optic detection in optically isotropic crystals," *Journal of the Optical Society of America B*, vol. 21, no. 3, pp. 622–631, 2004.

[158] R. C. Jones, "A new calculus for the treatment of optical systems," *Journal of the Optical Society of America*, vol. 31, p. 488, 1941.

[159] A. Bauch and H. R. Telle, "Frequency standards and frequency measurement," *Reports on Progress in Physics*, vol. 65, no. 5, pp. 789–843, 2002.

[160] R. Wynands and S. Weyers, "Atomic fountain clocks," *Metrologia*, vol. 42, no. 3, pp. S64–S79, 2005.

[161] S. Weyers, V. Gerginov, N. Nemitz, R. Li, and K. Gibble, "Distributed cavity phase frequency shifts of the caesium fountain PTB-CSF2," *Metrologia*, vol. 49, no. 1, pp. 82–87, 2012.

[162] F. Riehle, "Optical Atomic Clocks Could Redefine Unit of Time," *Physics*, vol. 5, p. 126, 2012.

[163] A. A. Madej, P. Dubé, Z. Zhou, J. E. Bernard, and M. Gertsvolf, "Sr 445-THz Single-Ion Reference at the 10^(-17) Level via Control and Cancellation of Systematic Uncertainties and Its Measurement against the SI Second," *Physical Review Letters*, vol. 109, no. 20, p. 203002, 2012.

[164] N. Hinkley, J. A. Sherman, N. B. Phillips, M. Schioppo, N. D. Lemke, K. Beloy, M. Pizzocaro, C. W. Oates, and A. D. Ludlow, "An Atomic Clock with 10-18 Instability," *Science*, 2013.

[165] H. R. Telle, B. Lipphardt, and J. Stenger, "Kerr-lens, mode-locked lasers as transfer oscillators for optical frequency measurements," *Applied Physics B: Lasers and Optics*, vol. 74, no. 1, pp. 1–6, 2002.

[166] R. Holzwarth, T. Udem, T. W. Hänsch, J. Knight, W. J. Wadsworth, and P. S. J. Russell, "Optical frequency synthesizer for precision spectroscopy," *Physical Review Letters*, vol. 85, no. 11, pp. 2264–7, 2000.

[167] H. Ito, S. Nagano, M. Kumagai, M. Kajita, and Y. Hando, "Terahertz Frequency Counter with a Fractional Frequency Uncertainty at the 10^(-17) Level," *Applied Physics Express*, vol. 6, no. 10, p. 102202, 2013.

[168] P. Gaal, M. B. Raschke, K. Reimann, and M. Woerner, "Measuring optical frequencies in the 0-40 THz range with non-synchronized electro-optic sampling," *Nature Photonics*, vol. 1, no. 10, pp. 577–580, 2007.

[169] B. Lipphardt, G. Grosche, U. Sterr, C. Tamm, S. Weyers, and H. Schnatz, "The Stability of an Optical Clock Laser Transferred to the Interrogation Oscillator for a Cs Fountain," *IEEE Transactions on Instrumentation and Measurement*, vol. 58, no. 4, pp. 1258–1262, 2009.

[170] D. W. Allan and D. D. Davis, "Accuracy of international time and frequency comparisons via global positioning system satellites in common-view," *IEEE Transactions on Instrumentation and Measurement*, vol. 34, no. 2, pp. 118–125, 1985.

[171] C.-L. Cheng, F.-R. Chang, and K.-Y. Tu, "Highly accurate real-time GPS carrier phase-disciplined oscillator," *IEEE Transactions on Instrumentation and Measurement*, vol. 54, no. 2, pp. 819–824, 2005.

[172] D. Gabor, "Theory of Communication Part 1. The Analysis of Information," *Journal of the Institution of Electrical Engineers-Part III: Radio and Communication Engineering*, vol. 93, no. 26, pp. 429–441, 1946.

[173] B. Boashash, "Estimating and interpreting the instantaneous frequency of a signal. I. Fundamentals," *Proceedings of the IEEE*, vol. 80, no. 4, pp. 520–538, 1992.

[174] J. Ville, "Theory and applications of the notion of complex signal," *Cables et Transmissions*, vol. 2A(1), pp. 61–74, 1958.

[175] B. Boashash, "Estimating and interpreting the instantaneous frequency of a signal. II. Algorithms and applications," *Proceedings of the IEEE*, vol. 80, no. 4, pp. 540–568, 1992.

[176] L. S. Rothman, I. E. Gordon, A. Barbe, D. C. Benner, P. F. Bernath, M. Birk, V. Boudon, L. R. Brown, A. Campargue, J.-P. Champion, K. Chance, L. H. Coudert, V. Dana, V. M. Devi, S. Fally, J.-M. Flaud, R. R. Gamache, A. Goldman, D. Jacquemart, I. Kleiner, N. Lacome, W. J. Lafferty, J.-Y. Mandin, S. Massie, S. N. Mikhailenko, C. E. Miller, N. Moazzen-Ahmadi, O. V. Naumenko, A. V. Nikitin, J. Orphal, V. I. Perevalov, A. Perrin, A. Predoi-Cross, C. Rinsland, M. Rotger, M. Šimečková, M. a. H. Smith, K. Sung, S. a. Tashkun, J. Tennyson, R. a. Toth, A. C. Vandaele, and J. Vander Auwera, "The HITRAN 2008 molecular spectroscopic database," *Journal of Quantitative Spectroscopy and Radiative Transfer*, vol. 110, no. 9-10, pp. 533–572, 2009.

[177] B. B. Hu, J. T. Darrow, X.-C. Zhang, D. H. Auston, and P. R. Smith, "Optically steerable photoconducting antennas," *Applied Physics Letters*, vol. 56, no. 10, p. 886, 1990.

[178] T. D. Drysdale, E. D. Walsby, and D. R. S. Cumming, "Measured and simulated performance of a ceramic micromechanical beam steering device at 94 GHz.," *Applied Optics*, vol. 47, no. 13, pp. 2382–5, 2008.

[179] K. Maki and C. Otani, "Terahertz beam steering and frequency tuning by using the spatial dispersion of ultrafast laser pulses," *Optics Express*, vol. 16, no. 14, pp. 10158–69, 2008.

[180] J. Bromage, S. Radic, G. P. Agrawal, P. M. Fauchet, and R. Sobolewski, "Spatiotemporal shaping of half-cycle terahertz pulses by diffraction through conductive apertures of finite thickness," *Journal of the Optical Society of America B*, vol. 15, no. 4, p. 1399, 1998.

[181] R. Inoue, K. Takayama, and M. Tonouchi, "Angular dependence of terahertz emission from semiconductor surfaces photoexcited by femtosecond optical pulses," *Journal of the Optical Society of America B*, vol. 26, no. 9, p. A14, 2009.

[182] G. Klatt, F. Hilser, W. Qiao, M. Beck, R. Gebs, A. Bartels, K. Huska, U. Lemmer, G. Bastian, M. B. Johnston, M. Fischer, J. Faist, and T. Dekorsy, "Terahertz emission from lateral photo-Dember currents.," *Optics Express*, vol. 18, no. 5, pp. 4939–47, 2010.

[183] S. Busch, B. Scherger, M. Scheller, and M. Koch, "Optically controlled terahertz beam steering and imaging," *Optics Letters*, vol. 37, no. 8, pp. 1391–3, 2012.

[184] Y. Monnai, K. Altmann, C. Jansen, H. Hillmer, M. Koch, and H. Shinoda, "Terahertz beam steering and variable focusing using programmable diffraction gratings," *Optics Express*, vol. 21, no. 2, p. 2347, 2013.

[185] R. K. Wangsness, *Electromagnetic Fields*. Hoboken: John Wiley & Sons, 1986.

[186] Y.-S. Jin, G.-J. Kim, and S.-G. Jeon, "Terahertz dielectric properties of polymers," *Journal of the Korean Physical Society*, vol. 49, no. 2, pp. 513–517, 2006.

[187] J. Jackson, *Classical Electrodynamics (3rd Edition)*. New York: John Wiley & Sons, 1998.

[188] J. Goodman, *Introduction to Fourier Optics (3rd Edition)*. Englewood: Roberts and Company Publishers, 2005.

[189] A. M. Racu, S. Priyadarshi, M. Leidinger, U. Siegner, and M. Bieler, "Coherent control of ultrafast shift currents in GaAs with chirped optical pulses.," *Optics Letters*, vol. 34, no. 18, pp. 2784–6, 2009.

[190] I. Wilke and S. Sengupta, "Nonlinear Optical Techniques for Terahertz Pulse Generation and Detection - Optical Rectification and Electrooptic Sampling," in *Terahertz Spectroscopy: Principles and Applications* (S. L. Dexheimer, ed.), pp. 41–72, CRC Press, 2007.

[191] R. Yano, H. Gotoh, Y. Hirayama, S. Miyashita, Y. Kadoya, and T. Hattori, "Terahertz wave detection performance of photoconductive antennas: Role of antenna structure and gate pulse intensity," *Journal of Applied Physics*, vol. 97, no. 10, p. 103103, 2005.

[192] R. Mendis, C. Sydlo, J. Sigmund, M. Feiginov, P. Meissner, and H. L. Hartnagel, "Spectral Characterization of Broadband THz Antennas by Photoconductive Mixing: Toward Optimal Antenna Design," *Antennas and Wireless Propagation Letters*, vol. 4, no. 1, pp. 85–88, 2005.

[193] I. S. Gregory, C. Baker, W. R. Tribe, I. V. Bradley, M. J. Evans, E. H. Linfield, A. G. Davies, and M. Missous, "Optimization of photomixers and antennas for continuous-wave terahertz emission," *IEEE Journal of Quantum Electronics*, vol. 41, no. 5, pp. 717–728, 2005.

[194] F. J. González and G. D. Boreman, "Comparison of dipole, bowtie, spiral and log-periodic IR antennas," *Infrared Physics & Technology*, vol. 46, no. 5, pp. 418–428, 2005.

Acknowledgements

Für die Unterstützung bei der Erstellung meiner Dissertation möchte ich mich bei allen Menschen bedanken, die mich während dieser Zeit begleitet haben.

Besonders und an erster Stelle möchte ich Dr. Mark Bieler (PTB Braunschweig) danken, in dessen Arbeitsgruppe diese Arbeit entstanden ist und der als mein wissenschaftlicher Betreuer in den letzten viereinhalb Jahren jederzeit für Fragen, Anregungen und ausführlichen Diskussionen zur Verfügung stand. Er hat mit Begeisterung und vielen Ideen wesentlich zum Gelingen dieser Arbeit beigetragen.

Mein weiterer Dank gilt Herrn Prof. Dr. Andreas Hangleiter (TU Braunschweig) für die Übernahme dieser Promotion. Als Erstgutachter hat er mich aktiv mit seinen Anregungen unterstützt.

Genauso möchte ich PD Dr. Uwe Siegner (PTB Braunschweig) für seine Tätigkeit als Zweitgutachter danken, zudem bedanke ich mich für die stetige und interessierte Begleitung meiner Arbeit.

Darüber hinaus gilt mein ausdrücklicher Dank meinen Kollegen an der PTB. Hier sind zum einen Sibylle, Niklas und Patryk zu nennen, die meinen Bezug zur Welt aufrecht erhalten haben. Zum anderen möchte ich Ana Maria, Shekhar und Christian für die vielen Diskussionen und den fachlichen Austausch in Labor und Büro danken. Darüber hinaus bin ich allen weiteren Mitgliedern des Fachbereichs für die gute Stimmung und das produktive Arbeitsklima dankbar.

Zu guter Letzt möchte ich meiner Familie und meinen Freunden für die uneingeschränkte Unterstützung über die letzten Jahre und für die unerschütterliche Zuversicht bezüglich des Gelingens dieser Arbeit danken.